Since 1955

Strojniški vestnik
Journal of Mechanical Engineering

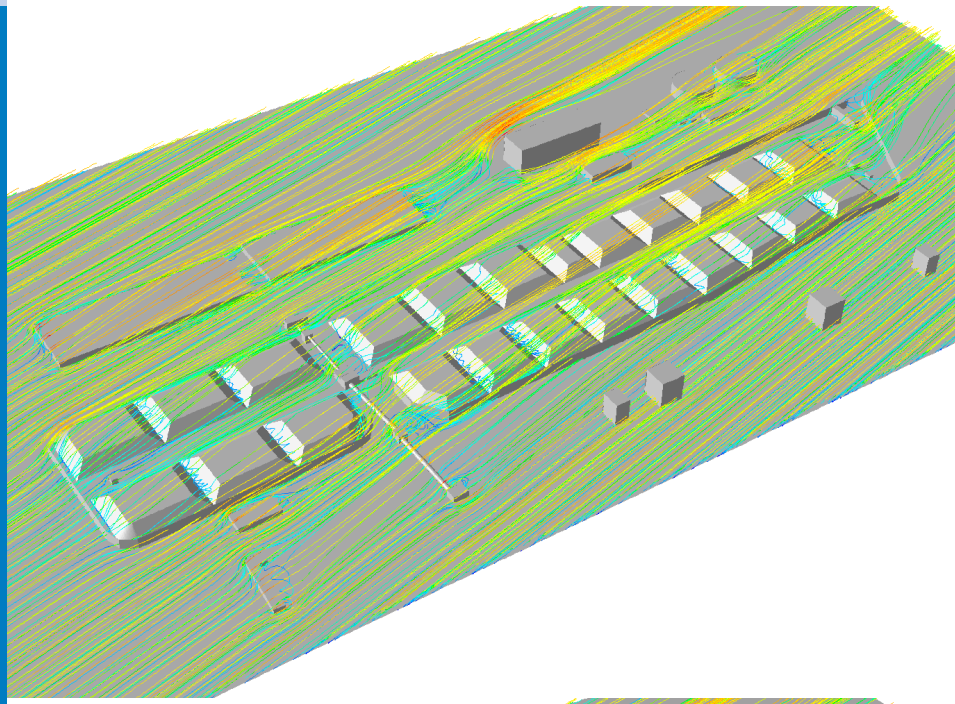

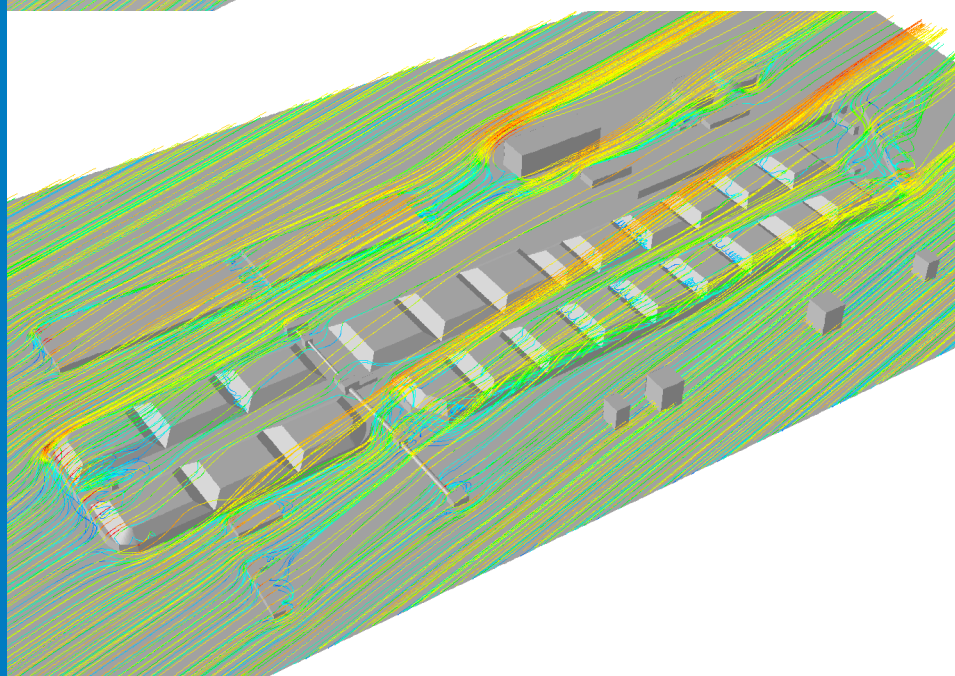

no. 11
year 2015
volume 61

Strojniški vestnik – Journal of Mechanical Engineering (SV-JME)

Aim and Scope
The international journal publishes original and (mini)review articles covering the concepts of materials science, mechanics, kinematics, thermodynamics, energy and environment, mechatronics and robotics, fluid mechanics, tribology, cybernetics, industrial engineering and structural analysis.
The journal follows new trends and progress proven practice in the mechanical engineering and also in the closely related sciences as are electrical, civil and process engineering, medicine, microbiology, ecology, agriculture, transport systems, aviation, and others, thus creating a unique forum for interdisciplinary or multidisciplinary dialogue.
The international conferences selected papers are welcome for publishing as a special issue of SV-JME with invited co-editor(s).

Editorial Office
University of Ljubljana, Faculty of Mechanical Engineering
SV-JME, Aškerčeva 6, SI-1000 Ljubljana, Slovenia
Phone: 386 (0)1 4771 137
Fax: 386 (0)1 2518 567
info@sv-jme.eu, http://www.sv-jme.eu

Print: Grafex, d.o.o., printed in 380 copies

Founders and Publishers
University of Ljubljana, Faculty of Mechanical Engineering, Slovenia
University of Maribor, Faculty of Mechanical Engineering, Slovenia
Association of Mechanical Engineers of Slovenia
Chamber of Commerce and Industry of Slovenia, Metal Processing Industry Association

President of Publishing Council
Branko Širok
University of Ljubljana, Faculty of Mechanical Engineering, Slovenia

Vice-President of Publishing Council
Jože Balič
University of Maribor, Faculty of Mechanical Engineering, Slovenia

Cover:
Wind conditions over the coal and iron ore stockpile in the Port of Koper were analysed by using CFD simulations. Wind exposure was determined for different wind directions and intensities with the aim of estimating potentials for occurrence of wind-induced dust lifting. Several wind reduction measures were simulated. The cover image shows near-ground pathlines for eastern wind for two wind-breaker fence types: solid fence (bottom) and porous fence (top).

Courtesy: LVTS, Faculty of Mechanical Engineering, University of Ljubljana.

ISSN 0039-2480

General information
Strojniški vestnik – Journal of Mechanical Engineering is published in 11 issues per year (July and August is a double issue).

Institutional prices include print & online access: institutional subscription price and foreign subscription €100,00 (the price of a single issue is €10,00); general public subscription and student subscription €50,00 (the price of a single issue is €5,00). Prices are exclusive of tax. Delivery is included in the price. The recipient is responsible for paying any import duties or taxes. Legal title passes to the customer on dispatch by our distributor.

Single issues from current and recent volumes are available at the current single-issue price. To order the journal, please complete the form on our website. For submissions, subscriptions and all other information please visit: *http://en.sv-jme.eu/.*

You can advertise on the inner and outer side of the back cover of the journal. The authors of the published papers are invited to send photos or pictures with short explanation for cover content.

We would like to thank the reviewers who have taken part in the peer-review process.

The journal is subsidized by Slovenian Research Agency.

Strojniški vestnik - Journal of Mechanical Engineering is available on http://www.sv-jme.eu, where you access also to papers' supplements, such as simulations, etc.

Contents

Strojniški vestnik - Journal of Mechanical Engineering
volume 61, (2015), number 11
Ljubljana, November 2015
ISSN 0039-2480

Published monthly

Papers

Strojniški vestnik - Journal of Mechanical Engineering 61(2015)11, 621-631

DOI:10.5545/sv-jme.2015.2824 Original Scientific Paper
Received for review: 2015-07-02
Received revised form: 2015-10-07
Accepted for publication: 2015-10-08

Numerical Modeling of Dust Lifting from a Complex-Geometry Industrial Stockpile

Lovrenc Novak[1] – Benjamin Bizjan[1,2,*] – Jure Pražnikar[3] – Boris Horvat[2,3] – Alen Orbanić[2,3] – Brane Širok[1]

[1] University of Ljubljana, Faculty of Mechanical Engineering, Slovenia
[2] Abelium Research and Development, Slovenia
[3] University of Primorska, Institute Andrej Marušič, Slovenia

This paper investigates the dust lifting phenomenon at the coal and iron ore stockpile at the Port of Koper, Slovenia. Dust lifting presents a serious environment and health hazard, thus the main objective of our study was to propose efficient measures for wind erosion reduction. A numerical model of the stockpile was created using the computational fluid dynamics (CFD) software. Wind velocity fields above the piles were calculated for the current stockpile layout and for several modified cases with rearranged piles and added porous barriers. Results from numerical modelling were used in the USEPA model to determine dust emission factors. Comparison of selected cases shows a positive, although limited effect of porous fences and barriers on reduction of local velocities and consequently, dust erosion rate. On the other hand, pile rearrangement has little effect and may not be practical for implementation. Realistic stockpile geometry with adjacent structures has shown to cause wind velocity distributions, which are not consistent with the most studied cases of regular pile shapes and layouts. The angle of incoming wind is a key factor influencing effectiveness of both solid and porous windbarriers. The proposed placement of porous barriers between the piles has shown to be effective in reducing wind exposure and dust emission. To maintain the dust emissions at an acceptably low level, other measures such as spraying with water and crust-forming liquids may still be necessary at higher wind velocities.
Keywords: computational fluid dynamics, fugitive emissions, dust lifting, open storage pile, emission factor, wind velocity

Highlights
- *Wind-driven dust lifting from port stockpile was studied.*
- *Wind speed across piles was calculated numerically using CFD software.*
- *Solid fences provide a very limited wind protection.*
- *Porous fences significantly reduce total emission rate.*
- *Properly placed transverse barriers reduce wind velocity and emissions.*

0 INTRODUCTION

Wind-driven erosion of fine particles from granular materials stored in open stockpiles, also known as dust lifting, is one of the main environmental and safety issues of modern-day seaport operations. Most problematic in this respect are loose dry materials such as coal and iron ore due to the high fugitive emission potential during handling and storage. Large open stockpiles, such as those typically encountered in cargo ports, are especially problematic due to their exposure to wind. Different wind erosion mechanisms can be identified depending on the ratio of wind induced aerodynamic forces (lift and drag) and gravity force, such as creep, saltation and suspension **[1]**. The wind-induced fugitive dust emissions result in material loss from the stockpile and at the same time increase particulate matter concentrations, with significant health hazards when particles are transported to urban areas. Particulate matter emissions have become a global health issue as negative effects are observed at all levels of exposure **[2]**, therefore particulate emissions must be reduced as much as possible.

Over the last decade, computational fluid dynamics (CFD) with experimental validation has been used extensively for analysis of flow structures over different stockpile configurations. Badr and Harion **[3]** and **[4]** used 3D numerical simulations and validated them for wind tunnel measurements. Toraño et al. **[5]** found that the semicircular pile shape lowered dust emissions and study made by Turpin and Harion **[6]** showed that the flat-topped pile configuration is the most favorable shape to lower dust emissions. In very complex sites such as ports and power plants, where "24/7" activity is present, it is not possible to perform on-site experimental studies due to instrumentation and logistical limitations. In such cases, CFD simulations alone can be used as an alternative tool for engineers to improve the understanding of flow processes at fine spatial resolution and to evaluate emissions at particular industrial sites **[7]**.

To accurately evaluate occurrence of wind-induced erosion in ports and other industrial sites, stockpiles should not be considered as individual elements. An aggregate storage yard is composed of many stockpiles in addition to obstacles such as

*Corr. Author's Address: University of Ljubljana, Faculty of Mechanical Engineering, Aškerčeva 6, 1000 Ljubljana, Slovenia, benjamin.bizjan@fs.uni-lj.si

buildings and cranes, which can affect local wind distribution [8]. Stockpile arrangement at storage yards was found to significantly affect the dust lifting. The simulation performed by Diego et al. [9] showed that the front pile creates a "shadow" of wind over the back pile, thus emission of adjacent piles are not equal. Another step forward was made by Cong et al. [10] who studied 16 stockpiles arranged in 4 rows and 4 columns. Their analysis showed that total dust emission is increased when the distance to the adjacent piles is raised and *vice versa*. Therefore, in order to evaluate emissions from a particular stockpile, adjacent piles should also be considered. Calculations by Furieri et al. [11] showed that not only piles, but areas surrounding the piles could contribute significantly to the total emission of dust particles. Furthermore, the simulations made by Turpin and Harion [8] revealed a significant effect of adjacent buildings. In their simulation, three very long stockpiles were included in the calculation domain. While this may be a common situation in a power plant storage yard, the situation is very different at port terminals where coal is transported from different destinations and is then delivered to various customers. Coal at terminals cannot be "mixed up" to form a large single coal pile, therefore it is common that coal is warehoused in a large number of piles. The size, location and arrangement of piles is set up in a way to allow fast and efficient coal handling for the port authorities, suppliers and customers. Additionally, rearrangement or resizing of stockpiles to reduce fugitive emissions is often restricted by crane capabilities and placement of adjacent buildings, meaning that large-scale modifications may not be practical and economically justified. Taking all these issues in consideration, modeling of an actual configuration presents a challenge and an opportunity to improve the understanding of fugitive emissions.

In this study, we have used measured wind speeds and directions to simulate realistic scenarios in the cargo port. The height, size, arrangement and shape of piles were set to represent the most commonly used distribution of coal at the fully occupied port terminal. Moreover, surrounding buildings, solid fence and cranes were also included to achieve a more realistic model. Simulations of air flow in the model were performed by employing state-of-the-art CFD simulations. Additionally, simulated data were used to estimate emission rates by using the United States Environmental Protection Agency (EPA) emission formulation.

1 METHODS

1.1 Location and meteorological conditions

The Port of Koper is located in northern Adriatic Sea (Fig. 1a) and it covers about 5 km^2. It is a multi-purpose port and the basic activities in the Port of Koper are handling and warehousing of various cargos conducted at three terminals. At one particular terminal, named the European energy terminal (EET), port handles and stores coal and iron ore. The present facility has current holding capacity of 8 million tones. This terminal presents open storage area of 108,500 m^2 and is one of the largest bulk cargo terminals in southern Europe.

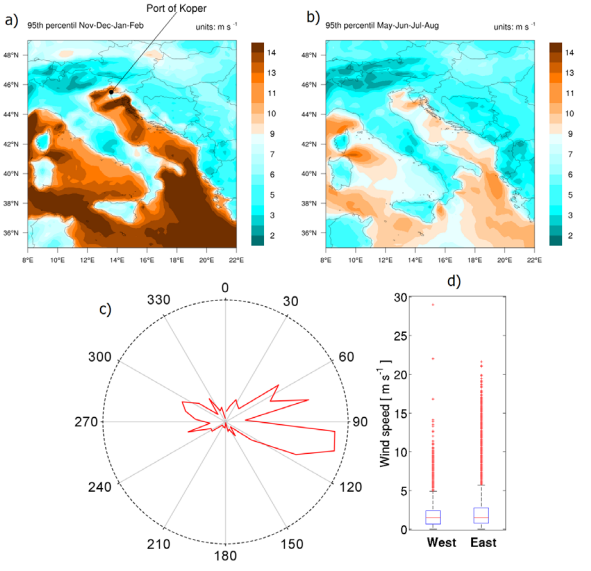

Fig. 1. *Regional location and wind conditions at the Port of Koper; 90th percentile of wind speed (ECMWF) above land and sea surface for: a) cold and b) warm period; c) wind rose and d) box plot of measured wind speed for west and east direction*

One of the most important factors that influence fugitive emissions is wind speed. Due to the lower sea roughness, wind speed above sea surface is higher than wind speed over land (Fig. 1a). The regional wind speed data was obtained from the European centre for medium-range weather forecasts (ECMWF). Following that, stockpiles located near seashore are usually exposed to higher winds, which lead to higher fugitive dust emissions. Statistical analysis of local wind speed recorded data (at 50 m above terrain) for the period between august 2012 and august 2013 at the Port of Koper are shown in Fig. 1b. The box plot (Fig. 1d) shows that gusts above 10 m/s are more frequent from east direction.

Nevertheless, maximum gust of 29 m/s was recorded from west direction. Furthermore, analysis of maximum wind speeds reveals that the highest speeds were observed from 75° and 250° direction. In summary, it is evident that winds from east and occasionally west reach very high speeds and are capable of causing significant dust emissions from the EET stockpile.

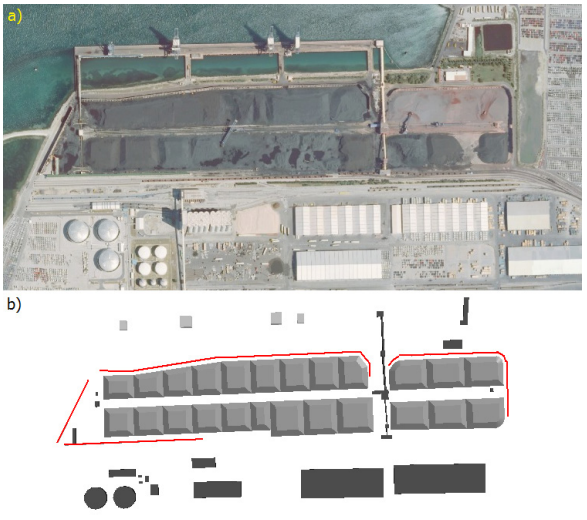

Fig. 2. *a) Satellite image of the coal and iron ore stockpile with surroundings; b) top view of the geometrical model*

1.2 Numerical Method and Model

Before performing the actual simulations of airflow over the coal and iron ore stockpile, a geometrical model of the site and boundary conditions had to be defined. The geometric 3D model was built on the basis of a satellite image (Fig. 2a) available from Geopedia [12]. It presents an area of 1380 m length in east-west direction and 730 m length in north-south direction (Fig. 2b). Vertically, the model was limited to the height of 200 m above terrain or sea. Minimum extent of the storage site surroundings, included in the model was determined on the basis of guidelines from relevant literature [13]. All significant wind directions and influences of surrounding structures were also taken in consideration and the model was further extended in some directions (i.e. south). Heights of included buildings and structures are presented in Table 1. Port authorities provided all necessary information about stockpiles, adjacent buildings and cranes. Buildings that have no influence on conditions at the stockpile at major wind directions were not included in the model. Basic distribution of piles in the model was made on the basis of the satellite picture and information provided by port authorities. The height of all piles was 10 m and base dimension was between 65 m and 80 m.

Table 1. *Buildings and structures in the 3D model*

		Dimensions (X×Y×Z) [m]
North side objects	Crane 1	25×15×25
	Crane 2	25×25×30
	Crane 3	25×25×30
	Crane 4	20×15×20
	Building 1	16.6×62.1×5.5
	Building 2	42.9×20.7×6
South side objects	Building 1	53×22×10
	Building 2	105×35×32
	Building 3	182.5×65.4×7
	Building 4	205×65.5×7
Stockpiles		65 to 75×65 to 80×10
Reservoir, diameter = 50 m, height = 15 m North-south coal conveyor, height = 7 m to 10 m		

Discretization of the geometric model into finite volumes (grid generation) was done with the Ansys ICEM CFD 14.5 software. Grid density was chosen on a basis of grid independence study, which was performed on the single pile case (see section 2.4). At the same time, available computer resources also had to be considered. The final hybrid grid consisted of 14.5 million hexahedral, tetrahedral and prismatic elements. Prismatic elements were used on walls to enable better resolution of the boundary layer. Near wall grid density was designed for the use of wall functions, which provide sufficient accuracy for flows around buildings.

Ansys Fluent 14.5 software was used for the CFD calculations. A Reynolds averaged Navier-Stokes (RANS) method, which is an industry-standard approach for simulation of atmospheric flows around buildings, was employed. Turbulence was modeled by the k–ε model [14], which is a proven and robust model, often employed in similar problems. Constants of the model were adjusted to the recommended values for simulation of atmospheric flows according to [15]. Standard wall functions with Fluent's default rough wall formulation [16] were employed. Since Fluent Release 14.0, the default rough wall formulation shifts wall location according to the local roughness height. This eliminates the well known problems associated with mesh resolution at walls with large roughness heights [17], caused by the requirement to keep the first node at the wall outside the specified roughness height.

Air was used as a working fluid assuming incompressibility (i.e. constant density). Steady state conditions were simulated. Second order discretization

schemes were used for all equations. Calculation reached convergence when the maximum scaled residuals for continuity and momentum equations dropped below 5×10^{-4} and for turbulence equations at least below 10^{-3}.

1.3 Boundary Conditions

The model boundary conditions were set to represent the actual conditions at the site. The inlet and outlet boundary surfaces were set in pairs depending on the simulated wind direction. For example, in case of the north-eastern wind directions the inlets were defined on the northern and eastern model boundaries while the outlets were set on the southern and western boundaries. Inlets were defined as velocity (U) inlets with velocity and turbulence quantities (k, ε) as functions of the vertical coordinate. Standard logarithmic profiles for atmospheric boundary layers were used ([15] and [18]). For illustration, turbulence intensity values, calculated from the inlet profiles as $Tu = \sqrt{(2k/3)}U$, reach 33.5 %, 17.2 % and 12.2 % at 1 m, 10 m and 50 m height, respectively. Terrain roughness length of 0.1 m was assumed for the profiles, meaning that the average roughness elements are 1 m high. Outlet boundaries were set as pressure outlets with average relative pressure of 0 Pa.

Walls of buildings and other structures, including the fence, were defined as hydraulically smooth walls with zero slip. Walls representing piles and terrain inside the stockpile fence were set as rough walls with equivalent sand grain roughness of 0.045 m. Terrain outside the fence (both land and sea) was treated as rough wall with equivalent sand grain roughness of 1 m, which takes into account the presence of different objects such as cars, trucks, trains, piers, sea waves etc.). Wall at the top of the model was set as a wall with zero shear stress.

Porous walls were used to represent certain structures, for example cranes located north of the stockpile that were simplified to a cuboid shape. Porous walls were also used to simulate perforated walls and barriers that were included in some of the calculated cases. The porous jump boundary condition type, which can be seen as a model for a thin membrane that has known velocity (pressure-drop) characteristics, was employed for all cases of porous walls. Only inertial resistance (quadratic function of velocity) was prescribed. For cranes and for porous fences the pressure drop at the wall equaled 0.2 times and 4 times the dynamic head of free flow, respectively.

1.4 Computed Cases

The prevalent wind directions and intensities were determined on the basis of continuous wind measurements at the site. The measured values provided the complete wind velocity vector at the height of 50 m. Only horizontal velocity component was taken into account since the vertical velocity was significantly smaller. For simulations, cases were defined at precise directions: 75° and 250° and two wind velocity magnitudes were considered for the simulations: 18 m/s and 22 m/s.

Taking into account the logarithmic velocity profile, speeds at 50 m height, 18 m/s and 22 m/s, correspond to 14.85 m/s and 18.15 m/s at the height of 10 m, respectively. Wind speed values at the height of 10 m were later used to calculate normalized wind speed and emission factors according to EPA methodology.

In addition to the simulation of base condition representing currently existing structures and fully occupied storage area, additional cases were computed. All the modifications to the base conditions were done with the aim of reducing exposure of piles to high wind velocities. The cases were designated with letters: (A) basic – current condition; (B) existing fence changed into a porous fence; (D) basic condition with piles on the south-west extended closer to the fence; (H) insertion of porous barriers between piles with heights of 11 meters.

Before performing simulations for different cases with the realistic site model, a model with a single pile was prepared to test grid independence and to determine the influence of incoming wind magnitude on normalized velocity distributions. The single pile model covered the same area and height as the realistic site model, but had all the structures and buildings removed. It included only a single pile in the middle of flat terrain. The pile was shaped as a cone with flat top, where bottom radius was 25 m, height was 10 m and side slope was 37°.

2 RESULTS AND DISCUSSION

Fugitive emissions are directly related to the wind speed and predicting wind flow conditions at stockpile surfaces plays an important role for assessment of the erosion potential. CFD results will be therefore presented in form of figures which show a top view of the different degrees of wind exposure over the piles. The piles were divided into subareas of constant u_s/u_r, where u_s is wind speed measured 25 cm from the pile surface and u_r is wind speed reference measured at the

height of 10 m above terrain. Furthermore, the emission factors were calculated according to the EPA method [19] where threshold velocity for coal u_t^* = 1 m/s [20] was used. EPA defines emission factors as statistical averages of the rate at which a pollutant is released to the atmosphere as a result of some activity, divided by the level of that activity. Formulae for their calculation are mostly based on regression analysis of relevant measured data. The emission factor for wind-generated particulate emissions from granular materials subject to disturbance is expressed in units of grams per year as follows:

$$k\sum_{i=1}^{N} P_i S_i. \quad (1)$$

In Eq. (1), k is a particle size multiplier, N the number of disturbances per year, P_i the erosion potential corresponding to the observed fastest mile of wind for the i^{th} period between disturbances and S_i the pile surface area. Particle size multiplier (k) was set to 0.5, which corresponds to emissions of PM_{10} particles [19].

The erosion potential function for a dry, exposed pile surface is defined by Eq. (2):

$$P = 58(u^* - u_t^*)^2 + 25(u^* - u_t^*), \quad (2)$$

where u_t^* is threshold velocity and u^* is given by Eq. (3).

$$u^* = 0.1u_{10}^+(u_s / u_r), \quad (3)$$

where u_{10}^+ is the fastest mile of wind at 10 m height. When friction velocity u^* is greater than the threshold friction velocity u_t^*, the erosion potential is positive. Because of the non-linear form of the erosion potential function, each erosion event must be treated separately. Sub-areas of constant u^* or u_s/u_r intervals were therefore considered as separate sources and it was assumed that there was only one disturbance per year.

The EPA method by itself is only used to quantify sources of particulate emissions and does not model subsequent transport and dispersion of airborne particles. Its prediction of yearly particulate emissions due to wind erosion was considered sufficient for the purpose of this study. In case spatial distribution of particle concentration would be required, then an additional dispersion model would need to be included in the simulations [21].

2.1 Single Pile Case

Grid refinement on the single pile case included three grids of variable element size near the pile (4 m, 2 m and 1 m maximum edge length). While finer grids showed slightly more detail in the velocity distributions, they did not show any major changes in their patterns. It was decided that the maximum edge length of 2 m at the pile surface, 4 m on terrain away from the pile and 7 m on distant surfaces provided sufficient resolution for final calculations. The same grid density was applied also for the realistic stockpile model, but with additional refinements near structures (i.e. 1 m max. element edge on the fence).

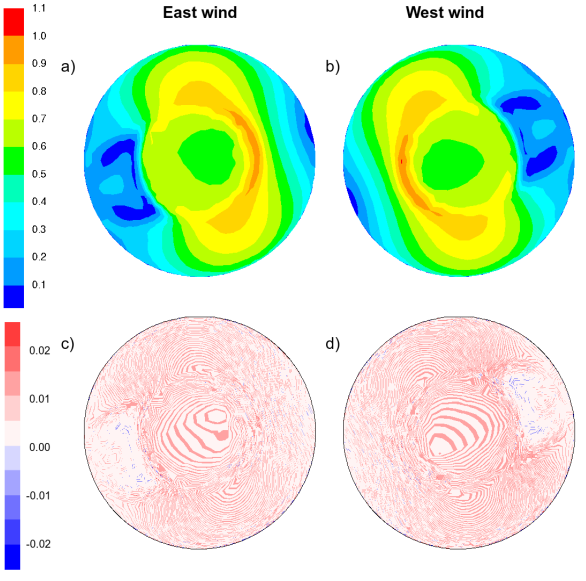

Fig. 3. *a) and b) Top view of us/ur contours at 25 cm from the flat-topped pile surface for wind magnitude 18 m/s; c) and d) top view of difference between us/ur contours at magnitudes of U = 22 m/s and U = 18 m/s*

Influence of the incoming wind magnitude on normalized velocity distribution was studied by performing calculations at two magnitudes, U=18 m/s and U = 22 m/s. Difference in results for the both magnitudes is shown by subtracting the normalized velocities u_s/u_r for the U = 18 m/s case from the U = 22 m/s case and presenting this difference in form of contour plot. Results shown in Fig. 3 show only minimal differences (up to ±0.02) for the both wind directions (75° and 250°) and therefore confirm independence of normalized velocity from the incoming wind magnitude and direction. These results are consistent with study of Badr and Harion [4] in which the normalized wind speed over a simple geometry was shown to be independent of the incoming wind velocity magnitude. However, the realistic configuration included multiple piles with adjacent structures, therefore the normalized wind speed distributions in the realistic model are expected

to show some dependence on the incoming wind conditions.

2.2 Case A – Current State

Fig. 4 presents current state conditions (case A) for two wind speeds for both west and east direction. It is evident that intermediate and high normalized velocities occur on top of the piles for the both wind directions. Generally, highest wind exposure is seen on pile edges. Wind exposure in case of west wind is higher than in case of the equally strong east wind, which indicates that existing wind protection is less effective in case of the west wind. In fact, the solid fence in the western part of the site is placed further away from the piles and at an angle, which provides favorable conditions for air currents to penetrate lower. The west wind also has fewer obstructions on its way over the central east-west oriented road, which is used by the coal stacking and reclaiming machinery. Therefore, higher wind exposure on the piles downwind from the central road can be seen for the case of west wind.

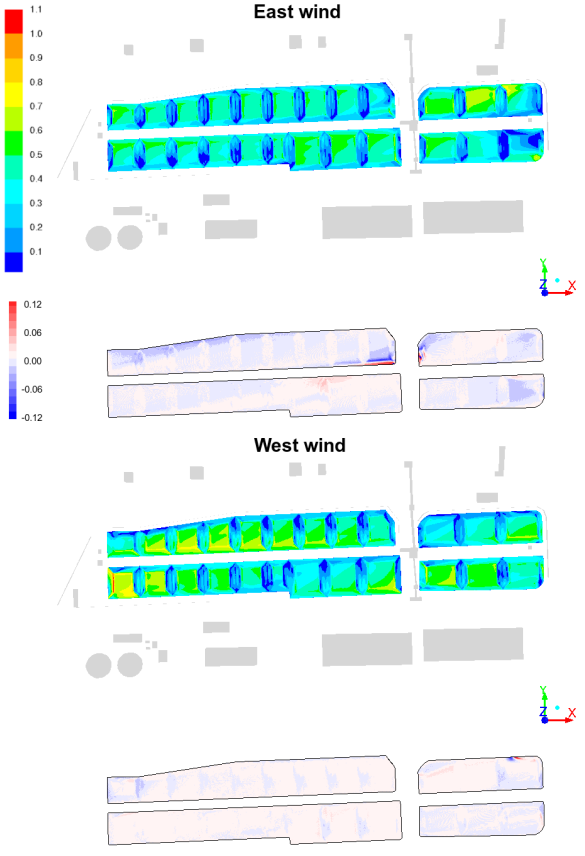

Fig. 4. *Case A for east and west wind; top view of us/ur contours in rainbow color map and difference between us/ur contours at magnitudes of U = 22 m/s and U = 18 m/s in red-blue color map*

Both wind directions were calculated at two incoming wind magnitudes, U = 18 m/s and U = 22 m/s. From Fig. 4 it can be seen that differences in results for the both magnitudes are very small for both wind directions. On average, a slight reduction in wind exposure is indicated for the higher wind magnitude, especially in case of east wind. Isolated spots with local differences of up to ±0.12 indicate shifts in flow structures (vortices), caused by the objects located upwind.

2.3 Case B – Porous Fence

Proper installation of porous fences and windbreak barriers can reduce dust emissions and protect coal stockpiles against high wind velocities [22]. The installation of porous fences that yields optimal protection is a challenging task and has been studied by several researchers. Reported wind tunnel investigations include measurements of surface pressure fluctuations on a prism behind a porous fence [23] and [24] or measurements of sand particle movement from a pile located behind a porous fence [25]. Field measurements on actual port stockpiles combined with CFD simulations are reported in [7] and [26], while a recent numerical study on a single pile is reported in [27]. These studies provide valuable knowledge for selecting optimal fence parameters such as location, height and porosity, but with regard to a single pile or to regular arrays of piles.

Replacement of the solid fence with a porous one was the first simulated measure for wind exposure reduction (Figs. 5 and 6). In case of solid barriers, the airflow is initially pushed over the barrier but then quickly lowers and continues without significant reduction in velocities. A vortex is formed leeward from the solid barrier, which can additionally deteriorate local conditions. On the other hand, porous barriers allow passing of fluid at a reduced velocity. This means that a region of reduced wind speed without any vortices is expected to form and stretch further downstream compared to the solid barrier case.

Fig. 5 shows streamlines for west wind at 18 m/s for solid fence (case A) and porous fence (case B). The eastern part of the stockpile is shown and wind blows towards the camera position. Streamlines originate from a surface of 2 m height, located just above the fence.

It is clearly seen that the existing solid fence causes many vortices that are pushed towards the stockpile edges, leaving the central part of piles

exposed. The porous fence on the other side eliminates any large-scale vortices and allows a uniform flow over the entire stockpile.

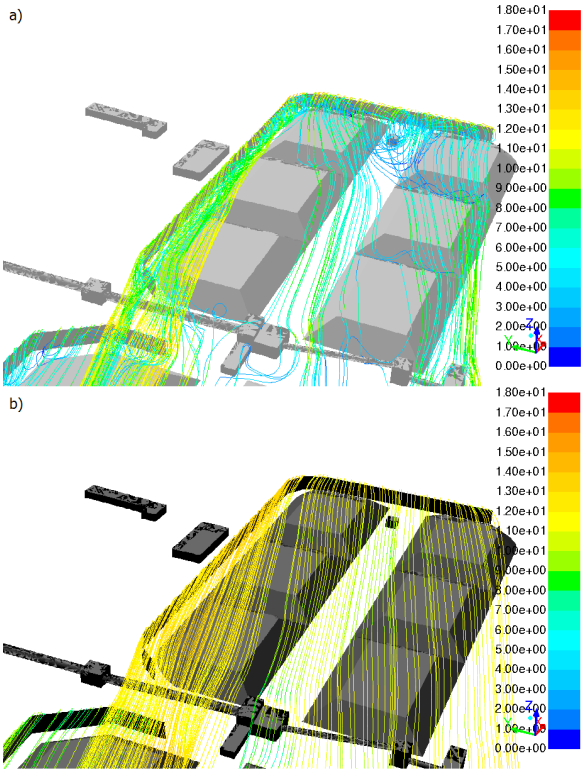

Fig. 5. *Streamlines for east wind at 18 m/s; a) solid-fence-case A; b) porous-fence-case B*

Fig. 6 shows normalized velocity distributions above piles for both east and west wind with the porous fence. Reduced wind exposure compared to the solid fence (Fig. 4) can be seen on some of the piles, while on the other piles, wind exposure seems to be unaffected or even increased. Reasons for limited porous fence effectiveness can be attributed to the large size of the terminal, which stretches in the direction of dominant winds, and to the sharp angle of incoming winds relative to the fence. Nevertheless, the largest wind speed reduction occurs at locations with the largest velocity magnitude while an increase mostly occurs at spots with relatively low wind velocities, meaning that velocity distribution becomes more uniform and has fewer extremes.

Since the wind erosion is only problematic at a relatively large wind velocity over piles, there is clearly an advantage of a porous fence (case B) in comparison with a solid fence (case A). This is confirmed by a reduction in total dust emissions which are lower in case B (consider the section 2.6 for details). Differences between the U = 18 m/s and the U = 22 m/s cases are low and on average show slightly smaller normalized velocities for the case of U = 22 m/s. This can be attributed to the non-linear resistance characteristic of the porous fence, which was set as a quadratic function of the upstream velocity.

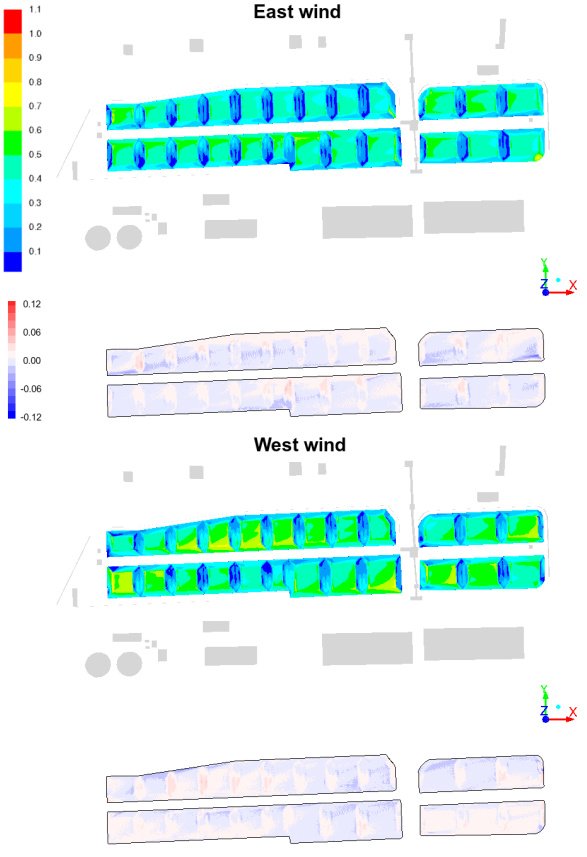

Fig. 6. *Case B for east and west wind; top view of us/ur contours in rainbow color map and difference between us/ur contours at magnitudes of U = 22 m/s and U = 18 m/s in red-blue color map*

2.4 Case D – Distribution of Stockpiles

Another possible measure for wind exposure reduction at the site would be to optimize distribution and size of piles. Numerous combinations of pile locations and sizes are possible in theory but in practice they are limited by the technical possibilities of the stacking and reclaiming machinery. Furthermore, technical and logistical requirements dictate filling and emptying of the stockpile and the length of individual piles. Therefore it is difficult to perform such optimization in reality, even if simulations indicated significant benefits.

Fig. 7 shows basic condition, very similar to case A, but with piles on the south-west extended closer to the fence. No significant differences in normalized

velocities can be seen relative to case A. However, differences between the U = 18 m/s and the U = 22 m/s cases are more evident in case D than case A. Especially in case of west wind, the effect of southern fence seems to not scale linearly with the incoming wind magnitude – lower normalized velocities are computed downwind from the fence at the higher incoming wind velocity magnitude.

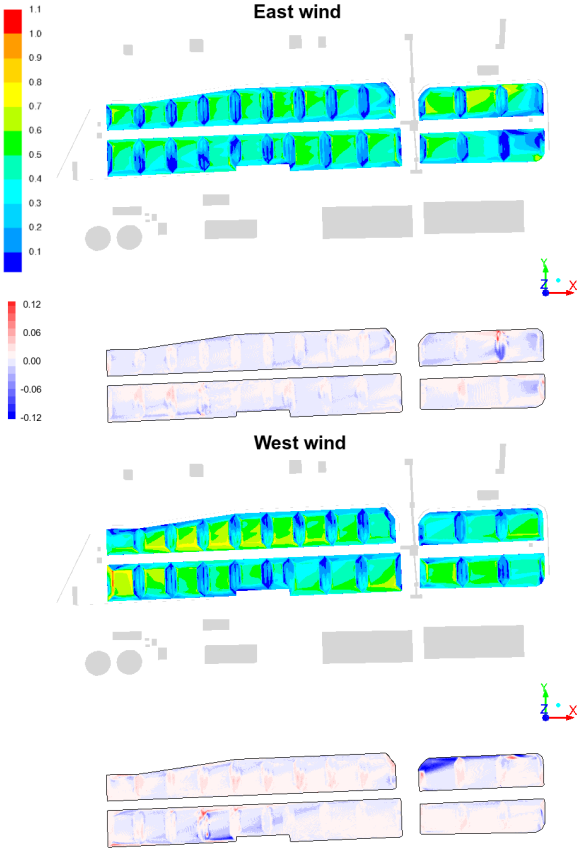

Fig. 7. *Case D for east and west wind; top view of us/ur contours in rainbow color map and difference between us/ur contours at magnitudes of U = 22 m/s and U = 18 m/s in red-blue color map*

2.5 Case H – Transverse Porous Barriers

As said, effectiveness of both solid and porous fences in reducing wind velocities above piles is greatly limited due the stretched shape and orientation of the cargo terminal and surrounding fences relative to the incoming wind direction. Major portions of the fence are hit by wind at sharp angles and the resulting area of reduced wind velocity downstream the fence is too short to reach piles further away. Therefore, a different approach for wind damping was proposed. Porous barriers between piles that were oriented transverse to the main winds were included into the numerical model (Fig. 8). Three porous barriers were placed at the south-western part of the stockpile to test the method mostly for west wind and another barrier was placed on the eastern edge of the south-western row of piles. All the barriers were 11 m high.

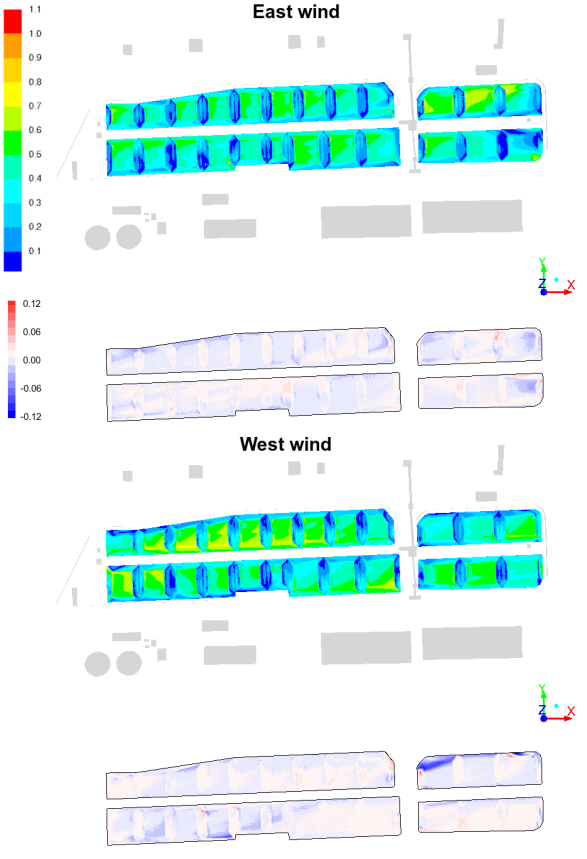

Fig. 8. *Case H for east and west wind; top view of us/ur contours in rainbow color map and difference between us/ur contours at magnitudes of U = 22 m/s and U = 18 m/s in red-blue color map*

Positive effects of the barriers are evident mostly in case of west wind. Wind exposure is significantly reduced for the first pile and partially also for the second pile downwind from the barrier. On average, differences between the U = 18 m/s and the U = 22 m/s cases show smaller normalized velocities in case of U = 22 m/s. As in the case of the porous fence (case B), this can be partly explained by the resistance characteristic of the barriers, which was set as a quadratic function of the upstream velocity.

2.6 Comparison of B-A and H-D Cases

Effects of modified/additional wind protection measures compared to the basic (current state) conditions are presented in Fig. 9. Case B (porous

fence) is compared to case A by calculating absolute difference between the normalized velocities at U = 18 m/s. In the same way, case H (four porous barriers) is compared to case D. Calculated differences are presented in form of contour plots, where color map is set to represent values between –0.2 and +0.2. Local differences can slightly exceed these values, but the color map was intentionally set to cap the extreme values in order to better present the bulk differences.

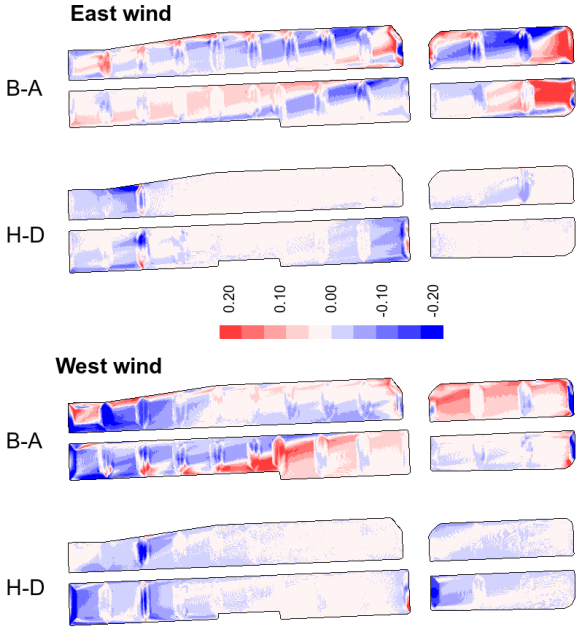

Fig. 9. *Top view of difference between us/ur contours for B-A, and H-D case (U = 18 m/s)*

Comparison of case B to case A shows that replacement of the existing solid fence by a porous fence would produce extensive regions of both reduced and increased wind exposure for the both wind directions. It is again evident that the large size of the dry bulk cargo terminal and its orientation relative to the direction of dominant winds present a challenging configuration for wind protection by porous fence that simply runs around the terminal perimeter. Judging from the normalized velocity differences, replacement of solid fence with a porous one seems to yield no overall benefits in wind protection, however, when taking into account emissions (see Fig. 10), benefits become evident. Results shown in Fig. 10 reveal that dust emission rates are lower for case B (porous fence); they are reduced by 50 % for both east and west wind. When comparing west and east wind emission rates it can be seen that the west wind emission rate is almost 10-times higher than the east wind emission rate (Fig. 10). The reason for much higher west wind emission rate is that fence in the western part of the site is less efficient in wind protection. Its location further away from the piles and its orientation relative to direction of incoming west wind provide conditions for air currents to penetrate lower and attain higher wind velocities above the piles.

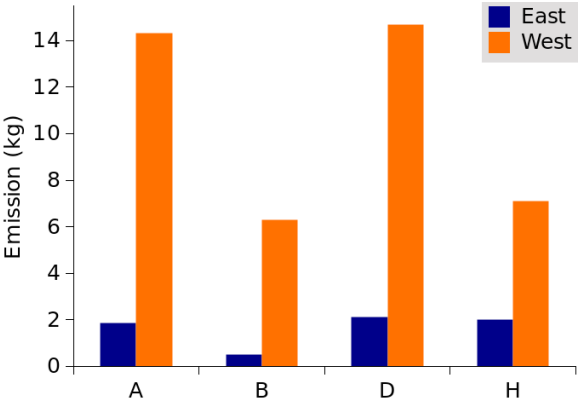

Fig. 10. *Total dust emissions under west and east wind flow for A, B, D and H case*

On the other hand, placement of porous barriers that are oriented transverse to the main wind directions (case H) clearly shows a highly positive effect. In this case, normalized velocities are significantly reduced for the first pile and partially also for the second pile downwind from the barrier. In case of west wind positive effects of barriers can be seen also on other piles in the wider stockpile area. Lower emission rates in case H are observed only for west wind while east wind emission rate is unchanged (Fig. 10). The reason for unchanged emission rate in case of east wind is that emissions in this case mostly occur on the eastern piles, so barriers placed further downwind are not effective in reducing critical wind velocities. In fact, most barriers in the model were intentionally placed at the south-western part of the stockpile to test their effectiveness mostly for west wind. In this respect, much lower emission reduction in case of east wind is not surprising. Further emission reductions for both wind directions could most probably be achieved by performing optimization of barrier locations, size and porosity parameters.

3 CONCLUSIONS

Simulations of wind conditions at the coal and iron ore stockpile at the Port of Koper were performed by employing CFD tools to assess the problem of dusting. Experimental validation by wind tunnel measurements or field experiments was not performed due to limited

time and resources available, but should preferably be executed in the future. Wind exposure of piles was analyzed for different wind conditions and by application of various physical measures for reduction of wind velocity. Results of simulations show that the existing solid fence provides a very limited protection from high winds due to the size and stretched shape of the stockpile area and its orientation relative to the main wind directions. Modifications to the fence by replacing it with porous structures were simulated and showed that their efficiency is limited for the same reasons as in the case of solid fence, although the total emission rate could be significantly reduced.

An efficient measure for reduction of wind velocity over the piles was found to be placement of porous barriers between the piles, oriented transverse to the main wind directions. However, such barriers on the real stockpile could impose significant limitations for the material stacking and reclaiming machinery. Watering and spraying with crust-forming liquids still remain a necessary step for prevention of wind erosion and fugitive emissions. Nevertheless, maps of local wind velocities that were created by the simulations enable identification of critical spots for occurrence of dusting and in this way help in optimization of spraying and reduction of associated costs.

The study showed that wind reduction by physical measures such as barriers is a very challenging task when dealing with large stockpiles and strong winds. Numerous dust emission research was done for single piles or regular arrays of piles, however, realistic sites are often hardly compared to such cases. Presence of adjacent fences, buildings, structures and irregular pile layouts have shown to have an important influence on wind conditions and should therefore always be taken into account when doing wind exposure analysis for real sites.

4 ACKNOWLEDGEMENTS

We would like to thank the port authorities for providing data for this research. This research was supported in part by European Union (European development fund, Interreg SLO-ITA, 2007-2013, project SAFEPORT - The port and industrial and environmental risk management) and in part by Slovenian Research Agency under research grants L7-5554 and P1-0294.

5 REFERENCES

[1] Bagnold, R.A. (1941). *The Physics of Blown Sand and Desert Dunes*. Methuen and Co., London.

[2] World health organization (2009). *Global Health Risk: Mortality and Burden of Diseases Attributable to Selected Major Risks*. p. 23-53.

[3] Badr, T., Harion, J.L. (2005). Numerical modelling of flow over stockpiles: Implications on dust emissions. *Atmospheric Environment,* vol. 39, no. 30, p. 5576-5584, **DOI:10.1016/j.atmosenv.2005.05.053**.

[4] Badr, T., Harion, J.L. (2007). Effect of aggregate storage piles configuration on dust emissions. *Atmospheric Environment*, vol. 41, no. 2, p. 360-368, **DOI:10.1016/j.atmosenv.2006.07.038**.

[5] Toraño, J.A., Rodriguez, R., Diego, I., Rivas, J.M., Pelegry, A. (2007). Influence of pile shape on wind erosion CFD emission simulation. *Applied Mathematical Modelling*, vol. 31, no. 11, p. 2487-2502, **DOI:10.1016/j.apm.2006.10.012**.

[6] Turpin, C., Harion, J.L. (2009). Numerical modeling of flow structures over various flat-topped stockpiles height: Implications on dust emissions. *Atmospheric Environment*, vol. 43, no. 35, p. 5579-5587, **DOI:10.1016/j.atmosenv.2009.07.047**.

[7] Cong, X.C., Cao, S.Q., Chen, Z.L., Peng, S.T., Yang, S.L. (2011). Impact of the installation scenario of porous fences on wind-blown particle emission in open coal yards. *Atmospheric Environment*, vol. 45, no. 30, p. 5247-5253, **DOI:10.1016/j.atmosenv.2011.07.005**.

[8] Turpin, C., Harion, J.L. (2010). Numerical modelling of flow structures over an industrial site: effect of the surrounding buildings on dust emissions. *Global NEST Journal*, vol. 12, no. 1, p. 40-45.

[9] Diego, I., Pelegry, A., Torno, S., Toraño, J., Menendez, M. (2009). Simultaneous CFD evaluation of wind flow and dust emission in open storage piles. *Applied Mathematical Modelling*, vol. 33, no. 7, p. 3197-3207, **DOI:10.1016/j.apm.2008.10.037**.

[10] Cong, X.C., Yang, S.L., Cao, S.Q., Chen, Z.L., Dai, M.X., Peng, S.T. (2012). Effect of aggregate stockpile configuration and layout on dust emissions in an open yard. *Applied Mathematical Modelling*, vol. 36, no. 11, p. 5482-5491, **DOI:10.1016/j.apm.2012.01.014**.

[11] Furieri, B., Santos, J.M., Russeil, S., Harion, J.-L. (2014). Aeolian erosion of storage piles yards: contribution of the surrounding areas. *Environmental Fluid Mechanics*, vol. 14, no. 1, p. 51-67, **DOI:10.1007/s10652-013-9293-4**.

[12] Geopedia, from *http://www.geopedia.si/#T105_F1173:6064_x402189.531_y47286.32_s17_b2*, accessed on 2013-09-30.

[13] Tominaga, Y., Mochida, A., Yoshie, R., Kataoka, H., Nozu, T., Yoshikawa, M., Shirasawa, T. (2008). AIJ guidelines for practical applications of CFD to pedestrian wind environment around buildings. *Journal of Wind Engineering & Industrial Aerodynamics*, vol. 96, no. 10-11, p. 1749-1761, **DOI:10.1016/j.jweia.2008.02.058**.

[14] Launder, B.E., Spalding, D.B. (1974). The numerical computation of turbulent flows. *Computer Methods in Applied Mechanics and Engineering*, vol. 3, no. 2, p. 269-289, **DOI:10.1016/0045-7825(74)90029-2**.

[15] Mandas, N., Cambuli, F., Crasto, G., Cau, G. (2004). Numerical simulation of the Atmospheric Boundary Layer (ABL) over

complex terrains. *Proceedings of European Wind Energy Conference*, London.

[16] ANSYS Inc. (2012). *ANSYS Fluent, Release 14.5*, User's Guide.

[17] Blocken, B., Stathopoulos, T., Carmeliet, J. (2007). CFD simulation of the atmospheric boundary layer: wall function problems. *Atmospheric Environment*, vol. 41, no. 2, p. 238-252, **DOI:10.1016/j.atmosenv.2006.08.019**.

[18] Richards, P.J., Hoxey, R.P. (1993). Appropriate boundary conditions for computational wind engineering models using the k-ε turbulence model. *Journal of Wind Engineering & Industrial Aerodynamics*, vol. 46-47, p. 145-153, **DOI:10.1016/0167-6105(93)90124-7**.

[19] EPA (2006). *Update of Fugitive Dust Emissions Factors In AP-42 Section 13.2.5 – Wind Erosion*. Midwest Research Institute, Kansas City.

[20] Topić N., Žitnik M. (2012). Fugitive Dust Emissions from a Coal-, Iron Ore- and Hydrated Alumina Stockpile. Khare, M. (ed.). *Air Pollution - Monitoring, Modelling and Health*. P. Intech, p. 197-222, **DOI:10.5772/33741**.

[21] Hriberšek M., Samec N., Ravnik J., Zadravec, M. (2011). Numerical Simulations of Wind Induced Particle Contamination in Gypsum Landfill Surroundings. *Environmental Modeling & Assessment*, vol. 16, no. 5, p. 479-489, **DOI:10.1007/s10666-011-9255-5**.

[22] Borges, A., Viegas, D. (1988). Shelter effects on a row of coal piles to prevent wind erosion. *Journal of Wind Engineering & Industrial Aerodynamics*, vol. 29, no. 1-3, p. 145-154, **DOI:10.1016/0167-6105(88)90153-5**.

[23] Lee, S.J., Park, C.W. (1998). Surface-pressure variations on a triangular prism by porous fences in a simulated atmospheric boundary layer. *Journal of Wind Engineering & Industrial Aerodynamics*, vol. 73, no. 1, p. 45-58, **DOI:10.1016/S0167-6105(97)00276-6**.

[24] Lee, S.J., Park, C.W. (1999). Surface pressure characteristics on a triangular prism located behind a porous fence. *Journal of Wind Engineering & Industrial Aerodynamics*, vol. 80, no. 1-2, p. 69-83, **DOI:10.1016/S0167-6105(98)00195-0**.

[25] Lee, S.J, Park, K.C., Park, C.W. (2002). Wind tunnel observations about the shelter effect of porous fences on the sand particle movements. *Atmospheric Environment*, vol. 36, no. 9, p. 1453-1463, **DOI:10.1016/S1352-2310(01)00578-7**.

[26] Cong, X.C, Du, H.B., Peng, S.T., Dai, M.X. (2013). Field measurements of shelter efficacy for installed wind fences in the open coal yard. *Journal of Wind Engineering and Industrial Aerodynamics*, vol. 117, p. 18-24, **DOI:10.1016/j.jweia.2013.04.004**.

[27] Song, C.F, Peng, L., Cao, J.J., Mu, L., Bai, H.L., Liu, X.F. (2014). Numerical simulation of airflow structure and dust emissions behind porous fences used to shelter open storage piles. *Aerosol and Air Quality Research*, vol. 14, no. 6, p. 1584-1592, **DOI:10.4209/aaqr.2013.11.0331**.

Strojniški vestnik - Journal of Mechanical Engineering 61(2015)11, 632-640
DOI:10.5545/sv-jme.2015.2778
Original Scientific Paper
Received for review: 2015-06-18
Received revised form: 2015-08-13
Accepted for publication: 2015-09-02

The Effects of a Pneumatic-Driven Variable Valve Timing Mechanism on the Performance of an Otto Engine

Fatih Uysal* – Selami Sagiroglu
Karabuk University, Faculty of Engineering, Turkey

In this study, the classic cam mechanism of a single cylinder, four-stroke, 6 hp spark-ignited engine was replaced by an electro-pneumatic rocker mechanism, which is designed and manufactured to open the intake valve at low (3.7 mm), normal (5.7 mm) and high (7.7 mm) lifts between engine speeds of 1600 rpm to 2200 rpm. An air compressor was used to feed 6 bar air pressure in order to have the plungers drive the cams in an orderly manner. A control panel was used to control plungers in order to modulate the valve lifts gradually. The volumetric efficiency, torque, power and specific fuel consumption with this operation were measured at full load and compared to the values with a classic cam mechanism. The results of the study showed that decreasing the valve lift at low engine speeds and increasing the lift at high speeds improve the engine performance. Moreover, it was concluded that the idle speed can be lowered by decreasing the valve lift at low engine speeds.

Keywords: variable valve timing (VVT), valve timing and lift electronic control system (VTEC), Otto engine, engine performance, spark ignition, electro-pneumatic rocker mechanism

Highlights

- *The effects of a pneumatic-driven valve mechanism on the performance a designed and manufactured engine is investigated.*
- *The existing rocker system was bypassed, and exhaust and intake rockers were remanufactured in accordance with the reference engine. Idle rockers were manufactured for both sides of the intake rocker. Two pneumatic-driven plungers were designed and manufactured, which lock and unlock the idle rockers to the intake rocker according to their order.*
- *The obtained values indicate that, depending on the engine speed, valve lifting at different heights has a positive impact on the performance of the engine.*
- *The reduction of valve lift makes the start-up of the engine easier and ensures that the engine can be started with less electricity.*

0 INTRODUCTION

Factors such as fuel economy, time economy, social concerns about environmental pollution and a production philosophy formed according to customer satisfaction, and the tightening of emission standard values by governments have forced designers to correct exhaust emissions accordingly and improve cam mechanisms. Particularly in the United States and Europe, the tightening of emission standard values and aggressive competitive conditions have forced automobile companies and universities to conduct research and development activities on cam mechanisms. Studies concentrate on the opening/closing times of intake and exhaust valves, as any failure in joining the fuel atoms with oxygen atoms in combustion chambers deteriorates the quality of combustion and, consequently, causes the emission of carcinogenic materials from the exhaust, which are hazardous to human health; these include nitrogen oxides (NOx), carbon monoxide (CO), unburnt hydrocarbons (HC), etc.

In internal combustion engines, volumetric efficiency is the most important parameter affecting combustion performance. The other parameters are engine torque, power output, fuel economy, and exhaust emission. At all engine speeds, increasing the amount of charge taken into the cylinders, which means an improved volumetric efficiency by variable valve timing, will also affect other parameters positively.

Volumetric efficiency is affected by several factors: atmospheric conditions outside the engine, and thermodynamic conditions inside the engine, such as cylindrical volume, flow area of fuel-air mixture, engine speed, open-close timing of intake and exhaust valves and valve lifting (opening) level, pressure changes inside the cylinder, and others.

The intake of fresh charge into the cylinder and the expelling of burnt mixture in spark-ignited (SI) engines are performed by opening and closing of valves which are opened by a crankshaft driven camshaft. The timing of the opening and closing of valves is a function of the shape of the camshaft and position of the crankshaft. In classic cam mechanisms, the intake valve opens 12 deg before it reaches top dead centre (TDC) and closes 56 deg after bottom dead centre (BDC). This provides additional time for taking more air-fuel mixture inside the cylinder **[1]**. This application can cause ideal results for an engine

*Corr. Author's Address: Karabuk University, Faculty of Engineering, Department of Mechanical Engineering, Karabuk, Turkey, fatihuysal@karabuk.edu.tr

which works at fixed speed. Depending on the needs of car drivers, it can be used at low speeds in urban areas at first start-up and high speed in rural areas or places which requires high performance. It must be taken into consideration that classical valve timing is optimized for a certain speed and engine load, but in studies over or under this speed, volumetric efficiency decreases. Changing the opening and closing advances of the intake and exhaust valves affects the efficiency of the engine, depending on its working rotation and load status. Increasing the advance of intake valves increases the volumetric efficiency at medium and low engine speeds. In addition, volumetric efficiency decreases with decreased intake valve opening advance and decreased exhaust valve closing delay [2].

Recently, the need for fuel economy and further reductions of hazardous exhaust emissions has forced engine designers to alter classic valve mechanisms and seek alternative ones. As a result of research activities, several camshaft and valve mechanisms have been developed. The fundamental principle in these mechanisms is the same and widely used on vehicles today. Electromagnetic, electromechanical, electrohydraulic, electro-pneumatic valve mechanisms suffer from some problems; research in this area is ongoing [3].

At low engine speeds, intake and exhaust camshafts are taken to advance together; at high engine speeds the intake camshaft or both camshafts are delayed; thus, volumetric efficiency is improved [4]. In a variable valve timing system used by Ferrari, there are separate camshafts for both intake and exhaust valves. A helical gear is opened on the camshaft with intake valves and the shaft is moved at axial direction according to engine rotation; thus opening advances and closing delays of intake cams are thus altered [5]. The movement of the crankshaft is transmitted to the camshaft through a sprocket or timing belt pulley. Gradual alteration of the calibration of the tensioning system of the sprocket can change the advance of the camshaft. The advance alteration systems performed this way can also increase the efficiency of the engine [6]. According to the data received from the engine control unit, the solenoid valve directs engine hydraulic to a hydraulic cylinder; therefore, it can ensure that the cylinder moves the pallet and the camshaft can perform thus relative action independent of regular rotation movement, and the opening and closing advances of the valves are changed [7].

The opening amounts of the intake and exhaust valves also affect engine efficiency, depending on the engine speed and engine load status. Camshaft profiles are used in order to change the opening levels of valves. Mechanical, electrical, hydraulic, pneumatic, and other energy sources are used to engage and disengage different cam profiles. Usually, next to a central cam profile, there are other cam profiles that engage and disengage with the help of a feeder needle. The Honda variable valve timing and lift electronic control system (VTEC) is the first system in the world that can simultaneously switch the timing and lift of the intake and exhaust valves. This system has made improvements in the maximum output at high rpm and also improved the low rpm range, with regards to idling stability and starting capability [8]. The customization of valve lifts and open/close advances according to engine speeds increase engine efficiency [9]. With a two-graded Variable Valve Actuation system, which is lower than the regular profile of camshaft, a 6.9 % decrease in fuel consumption can be achieved in dynamometer tests [10]. In such systems, which perform gradual variable valve timing and valve lift alteration, engine efficiency is optimum at several engine speeds instead of a single speed. Although it seems like a disadvantage, the low number of parts and low level of friction forces make these systems more utilizable.

Different systems of camshaft and its shape are being developed in order to open valves at different intake advances and close at closing advances. When the position of hall-effected sensors is changed to alter the advance of the valves in an electromagnetic valve mechanism fed by 42 V voltage, volumetric efficiency decreased and the air-fuel ratio deteriorated due to the bouncing of the intake valve disk, and the opening and closing delays at especially high engine speeds [3]. Appropriate systems have been developed for internal combustion engines, consisting of a planetary gear set, a worm mechanism, and a control motor that can continuously control the valve timing and lift [11]. As this type of system is being developed, its relation with existing systems also has to be examined. With a VVT strategy, a 5 % to 6 % improvement was observed in specific fuel consumption and a 47 % decrease was achieved in pumping losses compared to the classic cam mechanism; in addition, a decrease was observed in NOX values without any decrease in combustion quality with EGR (exhaust gas recirculation) [12].

As a result, it is difficult to obtain the necessary change in the closing of intake valve; late closing is more appropriate in cases where the change in timing is minor [13]. Difficulties in variable valve timing, the fact that the resulting increase in efficiency is higher than the energy needed to drive the developed system,

the low number of parts used, the long service life of the system, its failure-proof quality, and other factors have cause several methods to be researched for system development, although very few of them have become commercialized. For this reason, researches on the system is ongoing.

The purpose of this study is to investigate the design, manufacturing and effects of a pneumatic-driven valve mechanism on performance, which is similar to the VTEC model that drives the low and high cam noses with an unchanged profile at low and high rotations in addition to the classic cam nose on the same camshaft.

The design is based on the average speed of an engine with a classic cam mechanism in order to the optimize volumetric efficiency and air-fuel ratio. Pumping losses increase at low engine speeds, and the desired amount of charge cannot be taken into the cylinders at high rotation levels, due to the fixed cam mechanism, which results in a decreasing torque curve. In order to prevent such problems and achieve a horizontal torque curve, valves should open less at low engine speeds and more at high speeds. That is why variable valve timing is required.

1 MATERIAL AND METHOD

During the experiments two LONCIN brand, G200F(D) model four-stroke, single-cylinder, electronic ignition, 6 HP, gasoline engines and a KEMSAN brand 10 kW dynamometer were used. In Table 1, the technical specifications of the reference and testing machines are given.

Table 1. *Technical features of testing engine*

Brand	LONCIN BRAND 4 stroke, gasoline
Model	G200F(D)
Number of cylinders	1
Piston stroke	54 mm
Cylinder diameter	68 mm
displacement	196 cm^3
Ignition	Electronic ignition
Classical cam intake valve lift	5.7 mm
Intake valve low lift	3.7 mm
Intake valve high lift	7.7 mm

The first engine is the "reference engine" (classic cam mechanism engine), and the second engine is "test engine" (variable valve mechanism engine). Some modifications were made in the test engine:

1. In the reference engine, the crank and camshaft gears were directly connected to each other, whereas in the test engine the camshaft and crankshaft are connected with a timing belt (Fig. 1). Theintake and exhaust cams on the camshaft were remanufactured. In addition, 2 mm low and 2 mm high cams were added next to the regular intake cam.

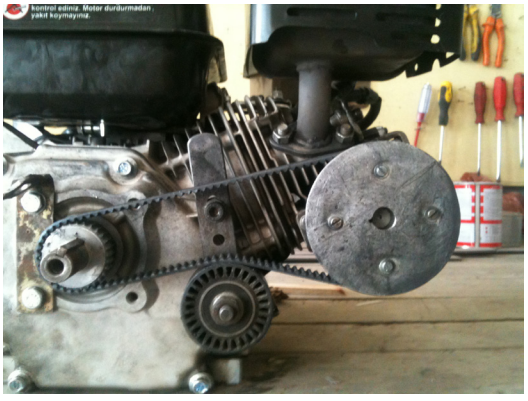

Fig. 1. *Test engine*

2. The existing rocker system was bypassed, and exhaust (A) and intake rockers (B) were remanufactured in accordance with the reference engine. Idle rockers (C) were manufactured at both sides of the intake rocker. Two pneumatic driven plungers (D) were designed and manufactured, which lock and unlock the idle rockers to the intake rocker according to their order (Fig. 2).

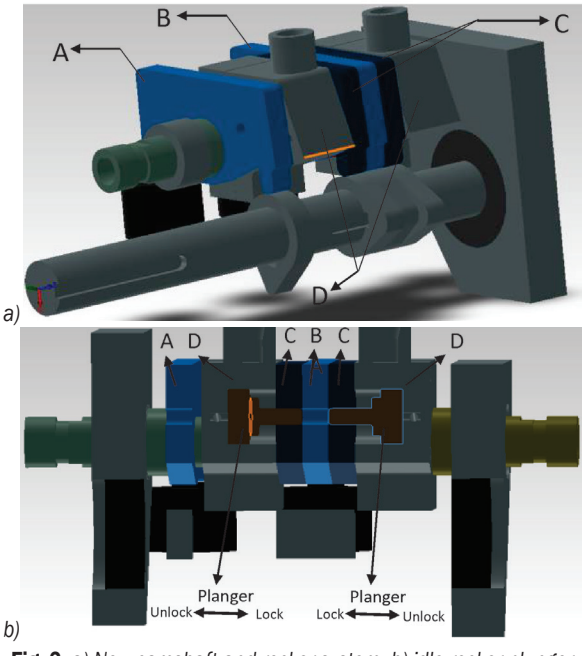

Fig. 2. *a) New camshaft and rocker system; b) idle rocker plunger cross-sections*

3. A quick coupler (E) was mounted at the end of rocker rod to feed air for pneumatic driven plunger system. Due to this coupler rocker, a carburettor was taken 30 mm away from the intake manifold using an intermediate connecting part (F) (Fig. 3).

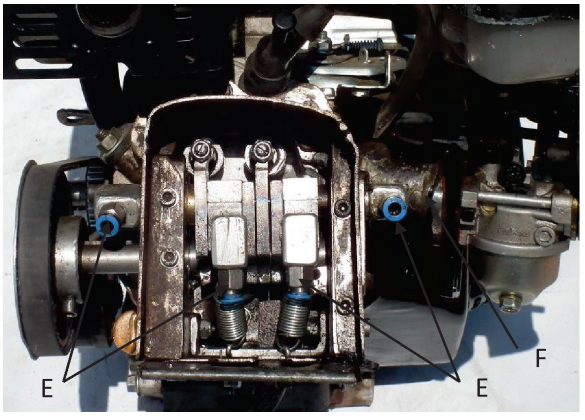

Fig. 3. *The connecting part between intake manifold and the carburettor*

4. A control panel was manufactured so that the plungers could step in and out at desired engine speeds. The air required by the system was provided by an external compressor and electricity was used from the mains (220 V_{AC}) (Figs. 4 and 5).

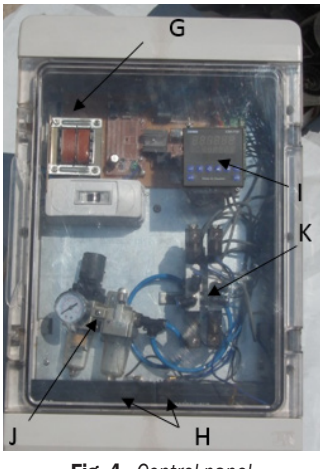

Fig. 4. *Control panel*

A 220 V_{AC} to 12 V_{DC} supply unit (G), two 12 V_{DC}, 7 Ah batteries (H), a double-contact tachometer (I), a conditioner (J), and a 5/3 electro pneumatic valve (K) were used so that this panel does not cause delay during operation (Fig. 4). The SET value on the tachometer can be adjusted to define at which engine speeds the system will engage and disengage the low and high cams. The data-reading speed of the tachometer can also be adjusted to prevent the evaluation of instant changes in engine speed in order to provide unnecessary fluctuation of engagement and disengagement. The electricity needed to operate the panel was supplied by two batteries in addition to the engine, since the supply voltages of circuit elements are different (12 or 24 V_{DC}).

Fig. 5. *Tachometer on control panel*

The testing mechanism is shown in Fig. 6.

1. Dynamometer
2. Coupler
3. Test engine
4. Conditioner
5. Air tank
6. Compressor
7. 5/3 electro pneumatic valve
8. Plunger (single impact spring return)
9. Tachometer (double-contact, normally open, normally closed)
10. 2 batteries (12 Vdc, 7 Ah)
11. Proximity switch

For the measurements, the engine was brought to operating temperature, the throttle was blocked fully open, and the engine was loaded with a dynamometer. The engine was tested by increasing the engine speed from 2000 rpm to 4000 rpm at 6 steps with 400 rpm increments.

1.1 Method

In order to adjust the valve lift in the test engine, the set values of the tachometer on the control panel were adjusted. For the normal cam, the SET1 ON value was set to 2300 rpm, the SET1 OFF value was set to 2200 rpm; for the high cam, the SET2 ON value was set to 3300 rpm, and the SET2 OFF value was set to 3200 rpm. Thus, it was ensured that during the acceleration, low, normal and high cams operated at 0 rpm to 2300 rpm, 2300 rpm to 3300 rpm and 3300 rpm to 5500 rpm ranges, respectively. When the engine is

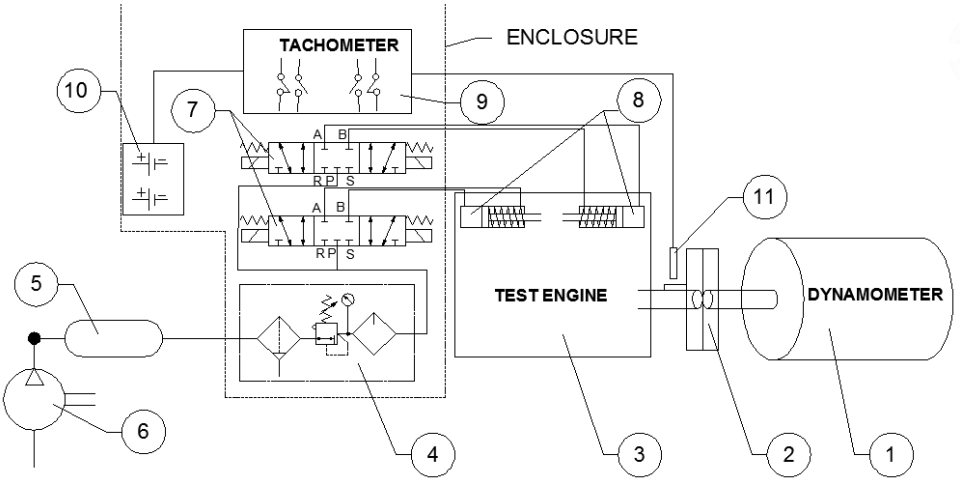

Fig. 6. *Experimental setup*

decelerating, low, normal and high cams operate at below 2200 rpm, 2200 rpm to 3200 rpm and 3200 rpm to 5500 rpm ranges, respectively. Different limits between acceleration and deceleration courses did not affect the test results as they did not correspond to the measurement speeds. The purpose of adjusting different on/off values is to prevent damage caused on the variable timing valve control system by frequent engagement and disengagement due to minor engine rotation changes and to ensure that the system has a longer life.

Before the tests were started, the engine was operated at idle for 15 minutes so that the operation temperature could be reached. Then the throttle was brought to the fully open position, the engine was loaded with a dynamometer, and measurements were taken.

Tests were conducted at 1600 rpm to 4000 rpm interval with 400 rpm speed increments. Intake valve lift data was taken at all speeds; 2000 rpm, 2800 rpm and 4000 rpm engine speeds were chosen for low cam, classical cam and high cam, respectively, in order to compare engine performance as they were very stable operating speeds for those cam types.

1.1.1 Effective Moment and Power of the Engine

When the engine is operated at the abovementioned speeds, the force value was read from the dynamometer indicator. The force value for each speed (kgf: kilogram-force) was multiplied with the dynamometer moment arm length (0.25 m) and the effective moment at that speed was found **[14]** and **[15]**.

$$M_e = F \times l \times 9.81. \tag{1}$$

The effective power of the engine is calculated by using Eq. (2) **[14]** and **[15]**:

$$N_e = \frac{M_e \times n}{9549.3}. \tag{2}$$

1.1.2 Measuring Fuel Consumption and Calculation of Specific Fuel Consumption

Super gasoline was used as test fuel. Under testing conditions, a chronometer was used to measure the time depletion time of 15 ml fuel in the fuel measurement tube under test conditions, and fuel consumption was calculated.

The specific fuel consumption is calculated using Eq. (3) **[14]** and **[15]**.

$$b_e = \frac{B_y}{N_e} \times 1000. \tag{3}$$

1.1.3 Air Consumption and Volumetric Efficiency

For air consumption, an air orifice diameter suitable for the engine was calculated first and the orifice shown in Fig. 7 was used.

In the test orifice diameter (d) was applied as 18 mm and pressure (h) was taken from the manometer as "mm H_2O column". Real air consumption was calculated as **[14]**.

$$Q_{real} = 0.1123 \times d^2 \times \sqrt{h}. \tag{4}$$

The density of dry air at sea level under standard atmospheric pressure and 15° C was taken as 1.225 kg/m³.

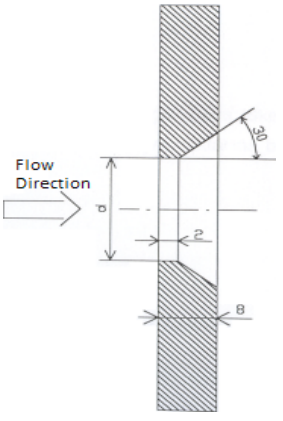

Fig. 7. *Airflow orifice*

Volumetric efficiency is calculated as a percentage by dividing the real air consumption (Q_{real}) for every speed with the amount of air ($Q_{theoretical}$) that the engine theoretically has to consume at that speed **[15]**.

$$\eta_v = \frac{Q_{real}}{Q_{theoretical}}. \quad (5)$$

Here, theoretical air consumption is calculated according to displaced cylinder volume (V_h) **[15]** with Eq. (6):

$$Q_{theoretical} = V_h \times \frac{n}{2}. \quad (6)$$

1.1.4 Excess Air Coefficient (λ)

Stoichiometric (or chemically correct or theoretical) proportions of fuel and air can be defined as the existence of just enough oxygen for conversion of all the fuel into completely oxidized products ($\lambda = 1$) **[15]**.

An MRU DELTA 1600L exhaust gas analysis device was used to measure exhaust emissions and the ambient temperature. The device calibrates itself in 15 minutes at start up. The exhaust-measuring probe of the engine analyser is installed into the exhaust pipe of the engine. After the engine was brought to normal working conditions, excess air coefficient, exhaust emissions and ambient temperature values were measured at the given engine speeds.

2 EVALUATION OF TEST RESULTS

Tests were conducted at 1600 rpm to 4000 rpm range with 400 rpm increments. Intake valve lift data was taken at all speeds and 2000 rpm, 2800 rpm and 4000 rpm engine speeds were chosen as reference speeds for low cam, classic cam and high cam, respectively, in order to compare engine performance, as they were very stable operation speeds for those cam types.

2.1 Volumetric Efficiency

It can be seen from Fig. 8 that at 2000 rpm the highest volumetric efficiency was measured at the low cam situation of the test engine with 60.86 %; at the same speed, the volumetric efficiency of the reference engine was measured as 44.51 %, meaning a 16.35 % increase in volumetric efficiency of the test engine. At 2800 rpm, the highest volumetric efficiency was measured at the classic cam situation of test engine with 52.20 %; at the same speed, the volumetric efficiency of the reference engine was measured as 50.05 %, which means a 2.15 % increase in the volumetric efficiency of the test engine. At 4000 rpm, the highest volumetric efficiency was measured at the high cam situation of test engine with 38.55 %; at the same speed, the volumetric efficiency of the reference engine was measured as 35.19 %, meaning a 3.36 % increase in the volumetric efficiency of the test engine.

The reason the test engine gives the highest volumetric efficiency in the low cam situation at 2000 rpm is that, depending on the decrease of the valve lift, pumping losses decrease, the flow speed of the fuel-air mixture passing through the valve opening increases, as a result of which turbulence inside the cylinder increases and the fuel-air mixture becomes more homogeneous.

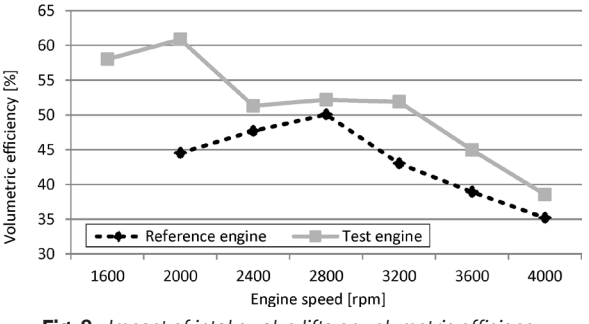

Fig. 8. *Impact of intake valve lifts on volumetric efficiency according to the engine speed*

The reason the test engine gives almost the same volumetric efficiency in a classic cam situation at 2800 rpm is that they have identical cams. As the classic cam of the test engine is remanufactured, a 2.15 % increase was witnessed in efficiency due to differences attributable to manufacturing and

installation. The reason that the test engine generates higher volumetric efficiency at high cam situation at 4000 rpm is that, although the open period of the valve at high speed decreased, the valve lift increased, which reduced the flow speed of the fuel-air mixture into the cylinder and increased the vacuum by the downward movement of the piston. Therefore, the volumetric efficiency increases.

2.2 Excess Air Coefficient (λ)

When the excess air coefficient graph is examined (Fig. 9), it shows that at 2000 rpm engine speed, when test engine is at low cam status, λ was measured as 1.048, whereas the λ of the reference engine in the same speed was measured as 1.111. The test engine remained in the lean mixture side with a 4.8 % deviation and stayed the closest to the ideal value. At a 2800 rpm engine speed, when the test engine is at classic cam status, λ was measured as 0.978, whereas the λ of the reference engine in the same speed was measured as 0.995. The test engine remained in the rich mixture side with a 2.2 % deviation, and the reference engine remained in the rich mixture side with a 0.5 % deviation. At a 4000 rpm engine speed, when λ of test engine was measured as 0.842 at high cam status, the λ of the reference engine in the same speed was measured as 1.072, and the test engine remained in the lean mixture side with a 15.8 % deviation.

The excess air coefficient (λ) approached the ideal value at low cam but moved away from it at high cam to the rich mixture side.

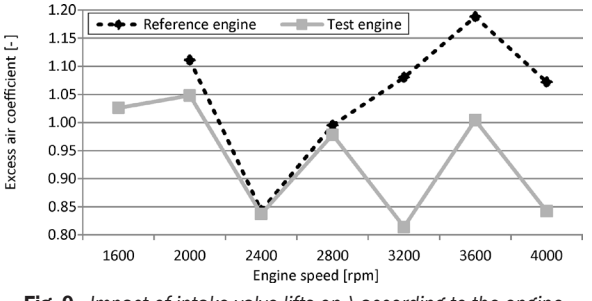

Fig. 9. *Impact of intake valve lifts on λ according to the engine speed*

This was partly the result of the carburettor design, which was made for the classic cam system and its detachment from intake manifold with a connecting piece. This system is more suitable for fuel injection systems.

2.3 Moment

The moment of the test engine (Fig. 10) at 2000 rpm speed at low cam status was measured as 10.3 Nm, whereas the moment of the reference engine at the same speed was measured as 9.31 Nm, meaning a 10.63 % increase in the moment of the test engine compared to the reference engine. The moment of the test engine at 2800 rpm speed at classic cam status was measured as 12.75 Nm, whereas the moment of the reference engine at the same speed was measured as 12.51 Nm, meaning a 1.92 % increase in the moment of the test engine compared to the reference engine. The moment of the test engine at 4000 rpm speed at high cam status was measured as 11.53 Nm, whereas the moment of the reference engine at the same speed was measured as 8.83 Nm, meaning a 30.58 % increase in the moment of the test engine compared to the reference engine.

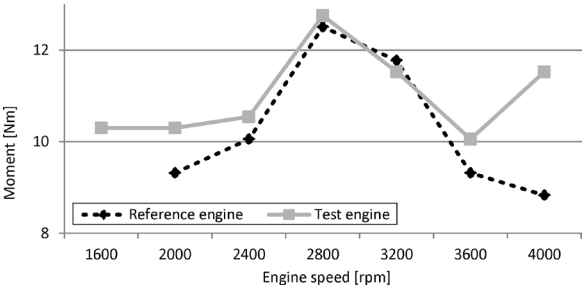

Fig. 10. *The impact of the different intake valve lifts on the engine moment according to the engine speed*

At 2000 rpm, the reason for the moment increase in test engine at low cam status is that the fuel-air mixture taken inside the cylinder increased depending on the increase in volumetric efficiency, and that λ took an almost ideal value (1.048). At 2800 rpm, the reason for which the test engine gave almost the same moment in classic cam status is that the cams are almost identical. As the classic cam of the test engine was remanufactured, due to differences caused by manufacturing and installation, a 1.92 % increase was observed in efficiency. The reason for the moment increase at high cam situation at 4000 rpm speed is the increase in volumetric efficiency and that λ remained in the side of the rich mixture.

2.4 Engine Power

When Fig. 11 is examined, at 2000 rpm engine, and the test engine at low cam status, the power of the engine was measured as 2.16 kW; meaning a 10.77 % increase in test engine compared to the reference

engine. At 2800 rpm, and the test engine at classic cam status, engine power was measured as 3.74 kW; compared to the 3.67 kW power of the reference engine at the same speed, meaning a 1.91 % increase in the power of the test engine. At 4000 rpm, and test engine at high cam status, the engine power was measured as 4.83 kW, whereas the power of reference engine at the same speed was measured as 3.70 kW, meaning a 30.54 % increase in the power of the test engine.

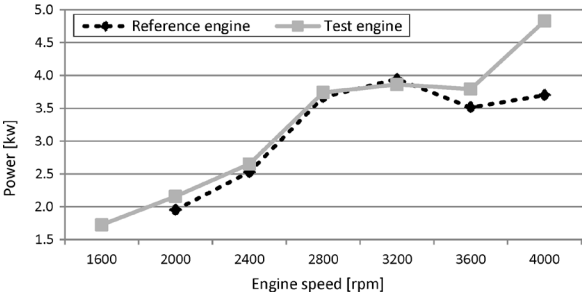

Fig. 11. *The impact of the different intake valve lifts on the engine power according to the engine speed*

As engine power is a function of its moment and speed, at high engine speeds work production per unit time increased and so the engine power was measured more with increased moment at these speeds.

2.5 Specific Fuel Consumption

The specific fuel consumption of the test engine (Fig. 12) at 2000 rpm at low cam status was measured as 427.85 g/kWh, whereas the specific fuel consumption of the reference engine was measured as 461.10 g/kWh, meaning a 7.2 % decrease in the fuel consumption of test engine compared to that of reference engine. At 2800 rpm, the specific fuel consumption of the test engine at classic cam status was measured as 388.794 g/kWh, whereas the specific fuel consumption of the reference engine was measured as 399.34 g/kWh, meaning a 2.64 % decrease in the fuel consumption of test engine compared to that of reference engine. At 4000 rpm, the specific fuel consumption of the test engine at high cam status was measured as 335.52 g/kWh, whereas the specific fuel consumption of the reference engine was measured as 425.87 g/kWh, meaning a 26.93 % decrease in the fuel consumption of the test engine compared to that of the reference engine.

The reason for the decrease in the specific fuel consumption of test engine at low cam status at 2000 rpm speed is the increase in volumetric efficiency, with the fuel-air mixture being more homogeneous and the resulting in increase of moment and power values.

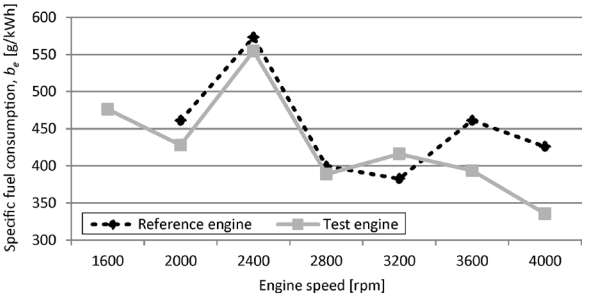

Fig. 12. *The impact of the different intake valve lifts on the specific fuel consumption according to the engine speed*

At 2800 rpm, the reason the test engine gave almost the same specific fuel consumption in the classic cam status is that the cams are almost identical. As the classic cam of the test engine was remanufactured, a 2.64 % decrease was observed in fuel consumption due to differences caused by manufacturing and installation. At 4000 rpm, the reason the test engine showed less specific fuel consumption at high cam status of the test engine is the increase in volumetric efficiency and λ remaining in the rich mixture side, as well as increased moment and power outputs.

3 CONCLUSION AND RECOMMENDATIONS

In these tests, the highest volumetric efficiency was found to be 60.86 % at low cam at 2000 rpm; the most ideal λ value was found to be 0.995 at classic cam at 2800 rpm; the highest increase in moment was found as 30.58 % at high cam at 4000 rpm; the highest decrease in specific fuel consumption was observed as 30.54 % at 4000 rpm. These obtained values indicate that, depending on the engine speed, valve lifting at different height has a positive impact on the performance of an engine.

During these tests, the idle speeds of the engines were also measured; when the idle of the classic cam engine decreased below 1200 rpm, the engine stopped; the test engine worked at 900 rpm idle speed at low cam.

The improvements in engine performance at low cam will contribute to fuel economy, particularly for vehicles used in urban transportation.

The reduction of valve lift makes the start-up of the engine easier and ensures that the engine can be started with less electricity. An automatic stop-start module that will be installed in cars will ensure savings from electric energy when the engine is

stopped and restarted at traffic lights. Thus, fuel economy can be achieved especially in roads with several and long traffic lights.

The fact that the engines used in the test had carburettors, and that the amount of fuel mixed with air depended on the structure of carburettor nozzle led to different λ values at different speeds. Repeating similar tests with injection and semi-injection engines will display different results.

4 REFERENCES

[1] Crouse, W.H., Anglin, D.L. (1994). *Automotive Engines*, 8th ed. Macmillan/Mc Graw Hill, New York.

[2] Aslan, R., Sürmen, A., Avcı, A. (1997). Theoretical and experimental investigation of volumetric effects on valve timing in a diesel engine. *5th Combustion Symposium*, Bursa, p. 220-230.

[3] Sagiroglu, S., Salman, M.S. (2007). Design and manufacturing of an electromagnetic valve train and the effects on exhaust emissions in a spark ignition engine. *Technology*, vol. 10, no. 2, p. 113-122.

[4] Leone, T. Christenson, E., Stein, R., (1996). Comparison of variable camshaft timing strategies at part load. *SAE Technical Paper*, no. 960584, p. 664-674, **DOI:10.4271/960584**.

[5] Titolo, A. (1991). The variable valve timing system-application on a V8 engine. *SAE Technical Paper*, no. 91009, p. 7-11, **DOI:10.4271/910009**.

[6] Li, L., Su, Y., Wang, Y., Tao, J., Xiao, M. (2001). Development of an electrical control VVT system for high speed SI engines. *Proceedings of the IEEE International Vehicle Electronics Conference*, Tottori, p. 115-119, **DOI:10.1109/IVEC.2001.961736**.

[7] Knecth, A., Stephan, W., Hannibal, W. (2002). VaneCAM - The third generation of camshaft adjustment system. *Motortechnische Zeitschrift Worldwide*, vol. 63, no. 4, p. 15-18.

[8] Hosaka, T., Hamazaki, M. (1991). Development of the variable valve timing and lift (VTEC) engine for the Honda NSX. *SAE Technical Paper*, no 910008, p. 1-6, **DOI:10.4271/910008**.

[9] Pierik, J.R., Burkhard, F.J. (2000). Design and development of a mechanical variable valve actuation system. *SAE Technical Paper*, no. 2000-01-1221, p. 1-8, **DOI:10.4271/2000-01-1221**.

[10] Sellnau, M., Kunz, T., Sinnamon, J., Burkhard, J. (2006). 2-Step variable valve actuation: System optimization and integration on an SI engine. *SAE Technical Paper*, no. 2006-01-0040, **DOI:10.4271/2006-01-0040**.

[11] Nagaya, K., Kobayashi, H., Koike, K. (2006). Valve timing and valve lift control mechanism for engines. *Mechatronics*, vol. 16, no. 2, p. 121-129, **DOI:10.1016/j.mechatronics.2005.09.007**.

[12] Fontana, G., Galloni, E. (2009). Variable valve timing for fuel economy improvement in a small spark-ignition engine. *Applied Energy*, vol. 86, no. 1, p. 96-105, **DOI:10.1016/j.apenergy.2008.04.009**.

[13] Stone, R., Kwan, E. (1989). Variable valve actuation mechanisms and the potential for their application. *SAE Technical Paper*, no. 890673, **DOI:10.4271/890673**.

[14] Martyr, A.J., Plint, M.A. (2007). *Engine testing*, 3rd ed. Elsevier, London, p. 144-146, p. 256-259, **DOI:10.1016/B978-075068439-2/50011-6**.

[15] Heywood, J.B. (2000). *Internal Combustion Engine Fundamentals*, International edition. Mc-Graw Hill, Singapore, p. 46-55, p. 69-71.

Strojniški vestnik - Journal of Mechanical Engineering 61(2015)11, 641-650

DOI:10.5545/sv-jme.2015.2493 Original Scientific Paper
Received for review: 2015-02-05
Received revised form: 2015-06-08
Accepted for publication: 2015-09-17

Numerical Modelling of Thermal Comfort Conditions in an Indoor Space with Solar Radiation Sources

Igor Bonefacic* – Igor Wolf – Bernard Frankovic
University of Rijeka, Faculty of Engineering, Croatia

In this paper, a three-dimensional case of heat transfer and air flow is presented for indoor space cooling with a wall-mounted A/C unit during the summer in Rijeka, Croatia. Numerical modelling is used to analyse the effect of different air flow angles of the A/C unit on the temperature and air velocity distribution under standard conditions with and without a direct solar radiation source. As parameters of thermal comfort conditions, the airflow velocities, indoor temperatures with its gradients, and the mean radiant temperature are analysed. Physical processes are modelled using the FLUENT computational fluid dynamics software. Calculations are carried out for an empty room without internal heat sources. When direct solar radiation through the window for an extreme case of summer solstice is included in the calculation, considerable deviations from thermal comfort conditions are observed, yielding the conclusion that solar radiation must be included in numerical simulations to properly predict heat balance and thermal comfort parameters in enclosed spaces.
Keywords: numerical modelling, thermal comfort, space cooling, air flow, solar radiation, mean radiant temperature

Highlights
- *Enclosed space during cooling season is modelled to determine temperature distribution and air flow field.*
- *Influence of the solar radiation on thermal comfort is examined using a solar ray-tracing algorithm.*
- *Mean radiant temperature is calculated.*
- *Local distortions from standard optimal comfort conditions are observed in cooling periods, taking into account solar radiation through the window.*

0 INTRODUCTION

The primary goal of the planning of the heating and cooling of an indoor working space is to find adequate microclimate conditions for occupants. This implies a thermodynamic balance between the human body and the environment. The balance and the perception of thermal comfort depend on several physical quantities that can be grouped as person-related (metabolic rate, clothing insulation) and environment-related (air temperature in the room, air humidity, local air velocity and the surface temperature of the surrounding walls, windows, and heating surfaces). These parameters must be appropriately combined in order to achieve a satisfactory thermal environment. Fanger et al. [1] presented a model that predicts the sensation of the draught as a function of air temperature, mean velocity, and turbulence intensity. Olesen and Parsons [2] presented the revision of EN ISO 7730 based on requirements for general thermal comfort (operative temperature and predicted mean vote) and local thermal discomfort (radiant temperature asymmetry, draught, vertical air temperature differences, and floor surface temperatures).

Designers of A/C system can choose between many different A/C unit types and setups. Alternative solutions also exist, such as those presented by Stritih and Butala [3] in which phase change materials are used for cooling and ventilation or Dovjak et al. [4] where low exergy H/C ceiling radiative panels and conventional systems with electric heaters and cooling split systems with indoor units are compared regarding individual thermal comfort conditions. Numerical simulations aid in selecting the most appropriate solution, giving the designer an opportunity to check in advance what level of thermal comfort can be expected to be produced in the given space. For those reasons, it is essential to develop optimally simple yet reliable numerical tools that can accurately simulate real spaces and the physical processes in them.

From a computational perspective, airflows in enclosed spaces are very complex. In the context of heating or cooling in warm climates, these flows are buoyant; in some cases, buoyancy drives the mean flow motion. In reality, most airflows are inherently three-dimensional and unsteady. Due to these characteristics, airflows in rooms present a great challenge to the available numerical models.

In recent years, extensive research efforts have been made in the development of general fluid flow and heat transfer software for solving the flow of air in enclosed spaces. Rutman et al. [5] and [6] and Wolf [7] give extensive insight into using numerical modelling tools for improving indoor environment quality, component optimisation, and complete system optimisation. Weather forecasting, including solar radiation, can be incorporated to decrease the energy demand of cooling systems using intelligent

*Corr. Author's Address: University of Rijeka, Faculty of Engineering, Vukovarska 58, 51000 Rijeka, Croatia, igorb@riteh.hr

control as in the paper by Dovrtel and Medved [8], in which a free-cooling system combined with heat storage is shown, and the method of incorporating weather forecasts into the control system is presented. With the constant progress of central processing units' (CPU) power, three-dimensional models of enclosed space with detailed geometry can now be modelled according to thermal comfort predictions with sufficient accuracy, as by Kuznik et al. [9] where CFD methods are used to investigate the velocity and temperature fields in a mechanically ventilated enclosure. Sevilgen and Kilic [10] performed a three-dimensional steady-state numerical analysis of the room heated by two-panel radiators and Aziz et al. [11] experimentally and numerically investigated performance of vortex, round, and square ceiling diffusers.

The objective of the study presented here is to determine the impact of the solar radiation source on the cooling performance of the wall-mounted A/C unit and thermal comfort conditions using the computational fluid dynamics (CFD) modelling method. The space under consideration is an office with one south-oriented external wall.

1 STUDY SETUP AND METHOD

A numerical model of the solar radiation through the window has been verified experimentally prior to analysing the effect of the radiation on the thermal comfort parameters in the space, by comparing the measured and calculated floor temperatures in the area exposed to direct solar radiation. The temperature measurements of the floor area have been carried out using the thermal imaging camera FLIR ThermaCAM S65. Results for indoor air flow velocity, temperature distribution, mean radiant temperature (MRT) and predicted mean vote (PMV) values are presented and compared for four different cases regarding air flow inlet angles from the A/C unit and solar radiation. The impact of the direct solar radiation through the window is verified with a thermal imaging camera.

1.1 Thermal Comfort Evaluation

Thermal comfort can be evaluated using different comfort indices, among which the predicted mean vote and predicted percentage dissatisfied (PMV/PPD) model and adaptive comfort approach (ATC) are well established and frequently used. For mechanically conditioned spaces, the PMV/PPD model should be used [12] and [13]. For offices and other spaces with sedentary workers, the requirement for mechanically air-conditioned buildings (based on the PMV/PPD model-category II) is an operative temperature range in winter 20 °C to 24 °C and 23 °C to 26 °C in summer. Thermal comfort also depends on the vertical temperature distribution in the room. The recommended vertical air temperature difference between 1.1 m and 0.1 m above the floor (at the head and at the ankle, respectively, of a person in the sitting position) or between 1.7 m and 0.1 m above the floor (at the head and at the ankle, respectively, of the person in an upright position) is less than 3 °C, ISO 7730:2005 [14]. According to [15], the most comfortable state is when the floor temperature is the same or slightly higher than the air temperature in the upper level. To avoid local discomfort, [13] and [14] recommend the air temperature difference between head and ankle to be less than 3 K. The state of thermal comfort cannot be determined simply by knowing the air temperature in the room.

A human body is constantly exchanging radiant heat with all the objects that surround it due to the temperature differences between them. The MRT of a space is the measure of the combined effects of the temperatures of the surfaces within that area of the human body. It is defined as the uniform temperature of an imaginary enclosure in which the radiant heat transfer from the human body is equal to the radiant heat transfer in the actual non-uniform enclosure [16]. The larger the surface area and the closer the person is to it, the more influence surface temperatures have on the individual. The mean radiant temperature, thus, changes with the position in the room and with it the corresponding air temperature, which provides thermal comfort.

Air-flow velocity is another important factor in determining thermal comfort because increased air velocity can cause discomfort due to increased convective heat transfer from the surface of a human body [14], limits local air flow velocity in offices and spaces where no major physical activities occur at 0.15 m/s during the winter (heating periods) and 0.25 m/s during the summer (cooling periods). The sense of draft is more pronounced with decreased physical activity. Furthermore, discomfort caused by draft increases with air temperature drops. Contrarily, if air velocity in an enclosed space is too low, it could cause a feeling of stuffiness and bad odour especially in winter (heating periods). It is, therefore, necessary to assure the optimal level of air circulation in the room.

The problem of indoor thermal comfort is sensitive to other physical parameters, in the cases of room environments with and without occupants. The existence of a thermal occupant was found to

produce thermal plume approximately 15% stronger in magnitude than that from an unoccupied room [17].

1.2 Study Setup

An empty office with the double glazed window facing south is modelled. Characteristic dimensions of the room and the window are given in Fig. 1. Four different cases regarding air flow inlet angles from the A/C unit and solar radiation on external surfaces and through the window are simulated and examined (Table 1). A few simplifications are made in the numerical model to decrease the number of control volumes needed to discretize the domain and, accordingly, accelerate the calculation. Internal obstacles such as office desks and cabinets are ignored. There are no additional heat sources in the room such as occupants, computers, monitors, etc.

Table 1. *Cases examined*

Case	Solar radiation	A/C air inlet angle
A	Not included	0°
B	Not included	45°
C	Included	0°
D	Included	45°

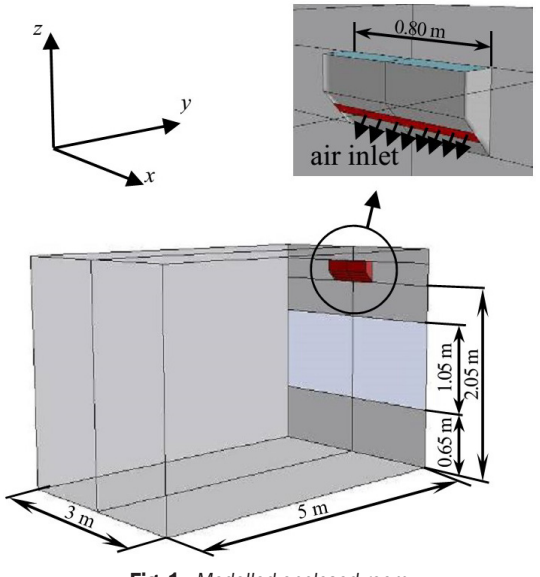

Fig. 1. *Modelled enclosed room*

Based on the known surrounding air temperature, convection boundary conditions are used to calculate heat transfer to the external surfaces. Where surfaces are exposed to the sun, radiation heat transfer is included. A numerical simulation is conducted for the most extreme case on the summer solstice at 13.00 in Rijeka, Croatia. Solar data for that day are given in [18]: direct solar radiation, 715 W/m² and diffuse solar radiation, 185 W/m². Assumed radiation properties of the wooden parquet and clear double-glazed window are used in the model and are given in Table 2.

Table 2. *Surface radiation properties*

		Window	Floor
Emissivity		0.9	0.9
Absorptivity	Visible	0.1	0.6
	IR	0.1	0.6
	Diffuse	0.1	0.6
Transmissivity	Visible	0.8	0
	IR	0.7	0
	Diffuse	0.7	0

The U-value of the wall and the U-value of the double-glazed window, are estimated as 0.4 W/(m²K) and 2.2 W/(m²K), respectively. The interior walls of the surrounding rooms are modelled with convection boundary conditions. It is assumed that the surrounding rooms (upstairs, downstairs and side rooms) have the same air temperature of 26 °C, corresponding to the indoor design temperature. The outdoor temperature is 32 °C, defined as the dry bulb temperature corresponding to 0.4 % of the annual cumulative frequency of occurrence and the mean coincident wet bulb temperature for Rijeka, Croatia. Constant air flow velocity was taken as the inlet boundary condition on the wall-mounted A/C unit with the following parameters: the inlet air velocity v_{in} = 2.0 m/s, the inlet air temperature T_{in} = 20 °C, and the air flow inlet angle φ = 0°/45°. In the PMV calculations, it is assumed that the metabolic rate is 1.2 met for sedentary activity (office), clothing insulation is 0.6 clo (trousers and shirt) with relative humidity assumed to be 50%.

1.3 Governing Equations

Transient solutions tend to be numerically more stable and often converge when solution controls are too restrictive to tend towards a steady-state solution. This is the case with high Rayleigh number flows in which the guidelines are to use time-dependent approach [19]. The problem of heat transfer and fluid flow in the space is solved using a mathematical model of the unsteady three-dimensional turbulent flow of incompressible fluid which is described with the general differential equation:

$$\frac{\partial}{\partial t}(\rho\varphi)+\frac{\partial}{\partial x_i}(\rho u_i\varphi)=\frac{\partial}{\partial x_i}\left(\Gamma\frac{\partial}{\partial x_i}\right)+S_\varphi, \qquad (1)$$

where variable j represents the velocity components u, v, w and the temperature T. In addition to the forced convection imposed by the wall-mounted A/C unit, the importance of buoyancy effects should be determined. The ratio of the Grashof and Reynolds numbers is:

$$Gr / Re^2 = \Delta\rho \cdot g \cdot H / \left(\rho \cdot v^2\right). \quad (2)$$

The ratio exceeds unity, showing that a strong buoyancy effect in the flow could be expected. Performances of different turbulence models in similar studies were examined in [20]. Turbulence was modelled using the realizable k–ε model, which consists of the transport equation for turbulent kinetic energy, and its dissipation rate and includes the generation of turbulent kinetic energy due to buoyancy effects. The values of model constants [21] are given in Table 3.

Table 3. *k–ε model constants*

Model constants	Value
C_2	1.9
$C_{1\varepsilon}$	1.0
$C_{3\varepsilon}$	1.2
σ_k	0.85
σ_ε	0.85

The system of transport equations was solved using the FLUENT CFD software, based on the finite volume method [22]. Heat transfer from the surroundings to the outer surface of the walls and window, due to convection and radiation, is defined as [21]:

$$q = \alpha_{ext} \cdot (T_o - T_{ext}) + \varepsilon_{ext} \cdot \sigma \cdot \left[T_\infty{}^4 - T_{ext}{}^4\right], \quad (3)$$

the second term in Eq. (3) represents the radiation term and is accounts for surfaces exposed to sun radiation. The radiation temperature T_∞ is determined so that radiative heat flux on the external surface is 375 W/m², taking into account the angle of the sun of 68°. Heat flux through the walls and window is calculated from [21]:

$$q = \frac{\lambda}{\Delta x} \cdot \left(T_{ext} - T_{int}\right), \quad (4)$$

where Δx is the thickness of the wall/window with constant thermal conductivity λ. The external heat transfer coefficients α_{ext}, in Eq. (3) for the wall and the window is calculated as 0.6 W/(m²K) and 6.5 W/(m²K), respectively.

The radiation energy source that results from incident solar radiation passing through the window is predicted with the solar ray tracing algorithm [21]. It uses the sun's position vector and two irradiation parameters, direct and diffuse solar irradiation, to set solar intensity. The resulting heat flux is coupled to the FLUENT calculation via the source term in the energy equation. The solar ray tracing algorithm also accounts for internal scattered and diffusive loading. The reflected component of direct solar irradiation is applied to all internal surfaces of the enclosed space.

1.4 Mean Radiant Temperature Calculation

The MRT calculation consists of the determination of view factors F_p, in every point of the room where MRT is to be calculated. It is based on the geometric position of the irradiated surface (human body) surrounded by surfaces with different temperatures, [16]. MRT should be calculated in relation to the human body surface area and orientation, but such a calculation is highly complicated. For simplicity, it is reduced to the point in space that is located in the human centre of gravity. The view factor for a very small surface area on the wall A_i, from an arbitrary point in space (x, y, z) can be calculated as:

$$F_{p-1} = \frac{A_i'}{4\pi}, \quad (5)$$

where A_i' is the projection of the surface area A_i to the sphere of radius $r = 1$ (Fig. 2).

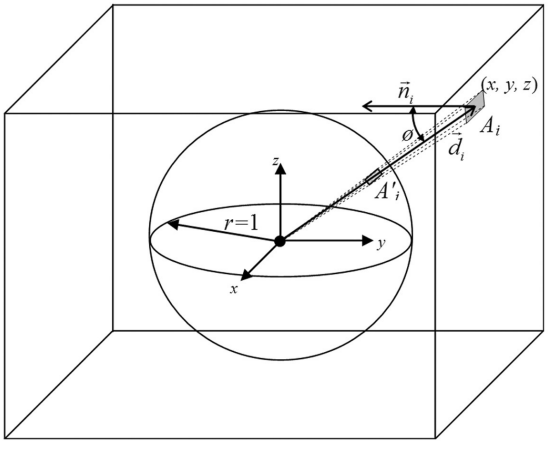

Fig. 2. *View factors calculation*

The projection area is then calculated as:

$$A_i' = \frac{A_i \cos\phi}{x^2 + y^2 + z^2} = A_i \cdot \frac{t}{\left(x^2 + y^2 + z^2\right)^{3/2}}, \quad (6)$$

where t is the distance from the originating point to the wall. When wall surfaces have a high emittance

(ε), they can be assumed to be black, and thus the following equation for MRT can be used [23]:

$$T_r^4 = T_1^4 \cdot F_{p-1} + T_2^4 \cdot F_{p-2} + \ldots + T_N^4 \cdot F_{p-N}. \quad (7)$$

To be valid, the wall surface area A_i should be adequately small. Using CFD software, such as FLUENT, allows for very small surface areas to be defined on walls so that this condition for view factor calculation is fulfilled. The user-defined function (UDF) was created and incorporated in FLUENT solver to calculate MRT in post-processing based on previously calculated wall surface temperatures. Different face mesh sizes were examined to determine the optimal value of surface area A_i regarding calculation time and discretization error. Four different mesh sizes with surface areas of 50 cm × 50 cm, 25 cm × 25 cm, 10 cm × 10 cm, and 5 cm × 5 cm were considered. Based on the results on calculated mean radiant temperatures for enclosed room with dimensions 5 m × 3 m × 2.5 m and arbitrary wall temperatures (Fig. 3), where maximum percentage error is about 0.7 % between cases 3 and 4, the optimal value for A_i is taken to be 10 cm × 10 cm as in Case 3.

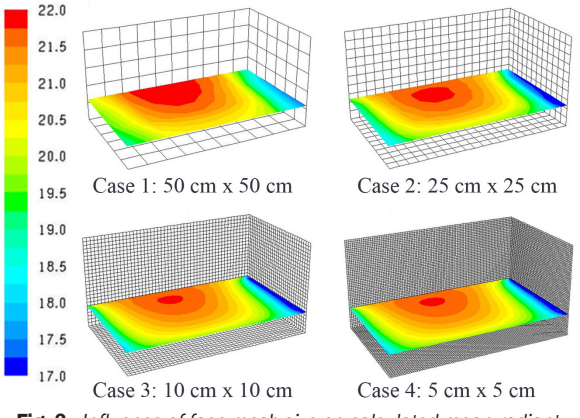

Fig. 3. *Influence of face mesh size on calculated mean radiant temperatures*

1.5 Model Verification

Verification of the solar ray tracing algorithm was conducted prior to analysing the effect of the solar radiation source on the thermal comfort conditions in the room. The temperature measurements of the floor area exposed to direct solar radiation through the window are done using the FLIR ThermaCAM S65 thermal imaging camera. Due to weather conditions, it was not possible to collect data exactly on the summer solstice, instead measurements were carried out on a clear sunny day on the 9th of July at 13.00 which is close to the most extreme case examined in the paper. To avoid reflections from the floor, a piece of cardboard was used to cover the entire window a moment before acquiring the thermogram. The modest resolution of the thermal imaging camera (320 pixels × 240 pixels) limited the target area to a square of approximately 1 m × 1 m. The acquired temperature field is compared with the temperature field of the same area calculated with CFD software. The photograph and thermogram of the target area are given in Fig. 4, and the calculated temperature field of the same area is given in Fig. 5. The measured and the calculated data show similar temperature fields as can be seen in Figs. 4 and 5.

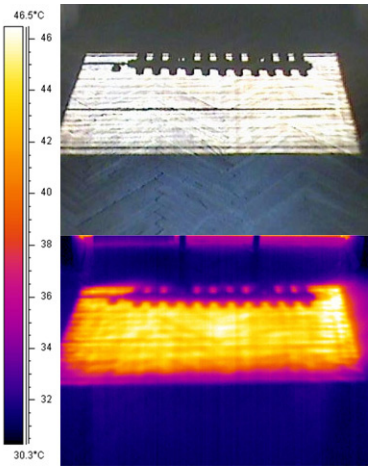

Fig. 4. *Photography and thermogram of the floor area exposed to the sun*

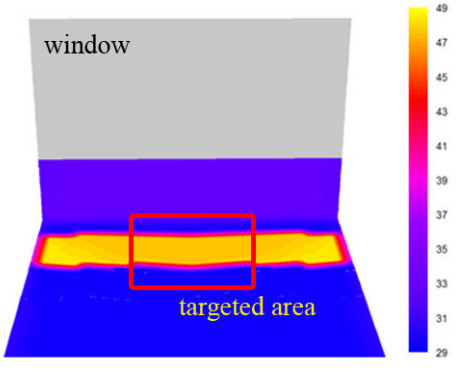

Fig. 5. *Calculated temperature field on the floor*

The average measured temperature of an area directly exposed to the sun is about 2.5 °C lower than calculated. The difference could be explained by the presumed values of absorptivity, emissivity and transmissivity of the floor and the clear double-glazed window.

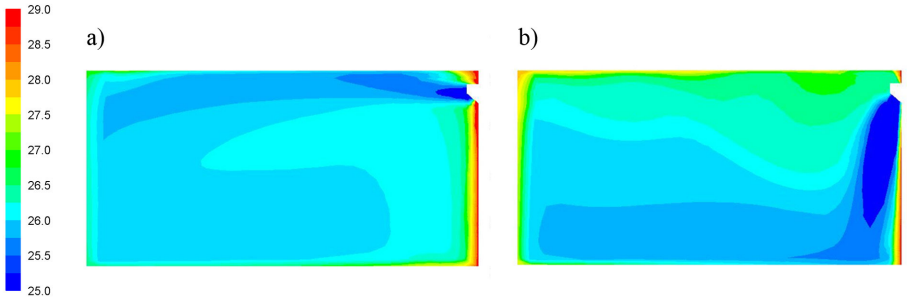

Fig. 6. *Temperature field at room cross section (x=1.5 m) for a) case A and b) case B*

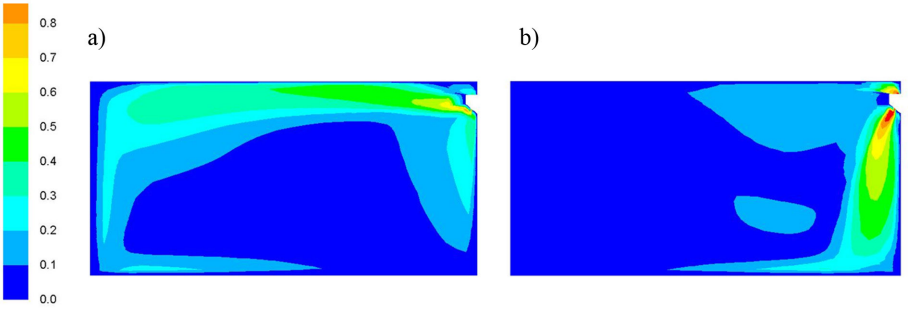

Fig. 7. *Air flow velocity field at room cross section (x=1.5 m) for a) case A and b) case B*

2 RESULTS AND DISCUSSION

2.1 Solar Radiation Source Not Included

The room is cooled by the cold air with an air inlet angle set to 0° from horizontal (Case A) and 45° from horizontal (Case B). In both cases, direct solar radiation through the window is not included in the calculation. By observing only the indoor air temperatures (Fig. 6) and air flow velocities (Fig. 7), both cases lead to satisfactory thermal comfort conditions regardless of the air flow inlet angle. When comparing the vertical temperature distribution in the middle of the room (Fig. 8), Case A leads to a more comfortable state where the temperature difference between $z = 1.1$ m and $z = 0.1$ m (at the head and at the ankle of a person in the sitting position) or between $z = 1.7$ m and $z = 0.1$ m (at the head and at the ankle of a person in an upright position) is negligible. In Case B, the air temperature is about 1°C lower at the floor level than at the head level, which is not recommended. It is a consequence of the cold air flowing downward from A/C unit resulting with the air stratification.

Fig. 9 shows the MRT profile at $z = 0.6$ m, corresponding to the chest level of a human in a sitting position. It can be seen that it does not change significantly with the air flow inlet angle, because

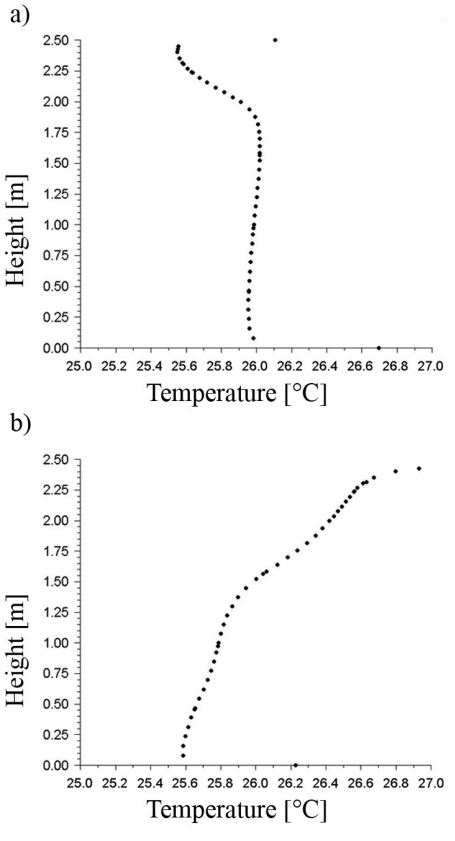

Fig. 8. *Vertical temperature distribution for a) case A and b) case B*

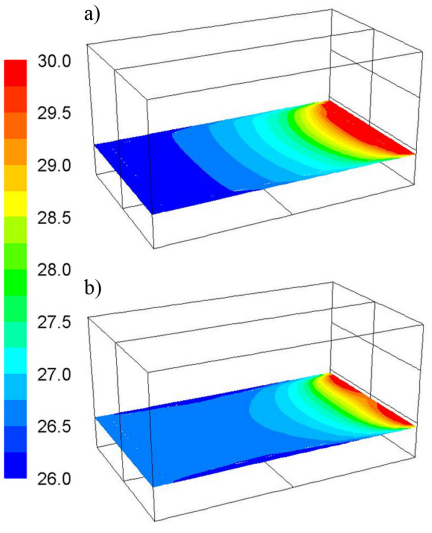

Fig. 9. *MRT at z = 0.6 m (sitting position) for a) case A and b) Case B*

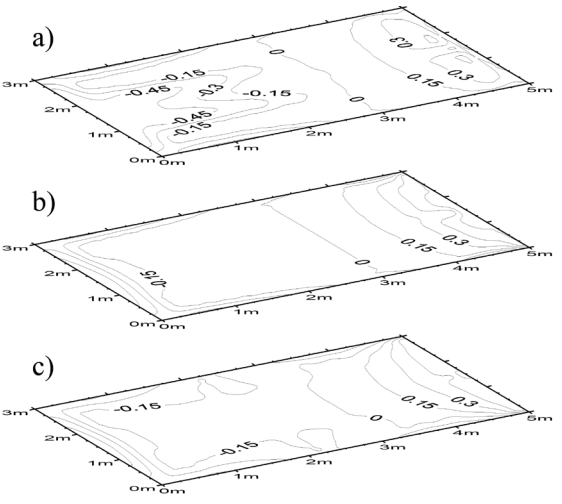

Fig. 10. *PMV values at three different levels for Case A; a) z = 1.7 m, b) z = 1.1 m, and c) z = 0.6 m*

in this case, it has only a small influence on the wall temperature. As Case A leads to more comfortable thermal conditions, PMV values are calculated for it. PMV values are displayed at three different heights, z = 0.6 m, z = 1.1 m and z = 1.7 m, corresponding to the chest level and the head level of a human in the sitting position, and at head level in the standing position, respectively (Fig. 10). It can be seen that PMV values are within the recommended values for Category II of indoor environments as defined by [12] at all levels (-0.5 < PMV < +0.5).

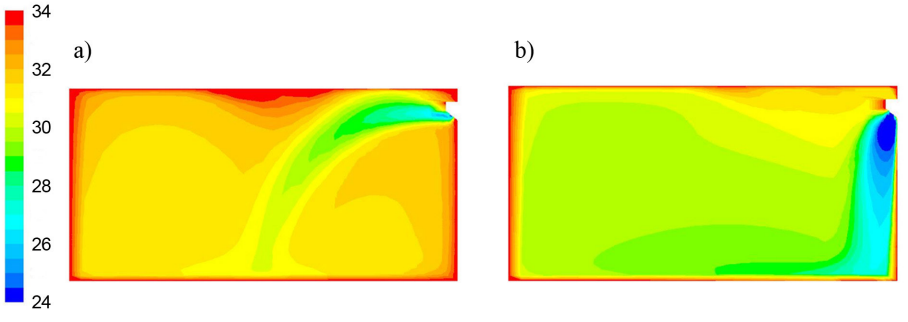

Fig. 11. *Temperature field at the room cross-section (x=1.5 m) for a) Case C and b) Case D*

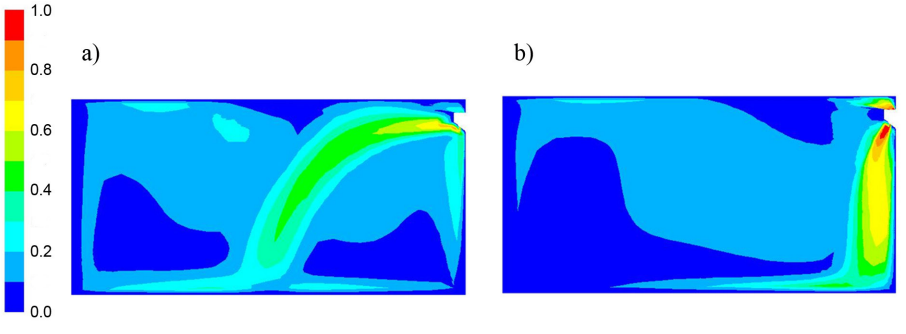

Fig. 12. *Air flow velocity field at the room cross-section (x = 1.5 m) for a) Case C and b) Case D*

2.2 Solar Radiation Source Included

The room is cooled the same way as in Section 2.1 but with direct solar radiation through the window included in the calculation (Case C and Case D). The solar altitude is set to 68°, matching an angle at summer solstice at noon on a latitude of approximately 45° North (Rijeka, Croatia), which represents the worst case scenario. As the sun's rays enter the room, they hit the floor at approximately 0.5 m from the window where the region of increased temperature is created. This region significantly affects the room temperature and flow field. As can be seen from Fig. 11, the cooling capacity of the same presented A/C unit is no longer sufficient to achieve thermal comfort conditions in the room, as the mean room temperature is about 4 °C higher when solar radiation is included in the calculation. Furthermore, the larger temperature difference between the surrounding air in the room and cold air from the A/C unit results in a different air flow field. In Case C (Fig. 12), it can be seen that, as opposed to cases without solar radiation (Fig. 7), the stream of cold air from the A/C unit drops much sooner due to a smaller buoyancy force, i.e. larger air temperature difference.

The mean radiant temperature profile, as seen in Fig. 13, is greatly affected by the high-temperature region on the floor (Fig. 14). MRT is also affected by the air flow inlet angle, as can be seen in Case D in which cold air from the A/C unit flows right over the heated region and, as a result, lowers its temperature by about 6 °C. In Case C, such an effect is not present because cold air from the A/C unit passes much higher over the heated region on the floor.

Based on the calculated temperature and air flow field, Case D leads to more comfortable thermal conditions; therefore, PMV values are calculated for that case. PMV values are displayed at three different heights, z = 0.6 m, z = 1.1 m and z = 1.7 m (Fig. 10). It can be seen from Fig. 15 that PMV values are much higher when solar radiation is included and that the recommended values are significantly exceeded even for category IV of indoor environments, as defined by [12].

As the quality of the installed windows is very low, such results were more or less as expected. To be able to cope with the increased air temperature in the room the cooling capacity of the wall-mounted A/C unit should be appropriately increased. As an alternative, high reflectivity window films could be used but they also block the sun's heat in the winter. Shading is often implemented to protect against overheating during the warm months. Most shading devices are attached to the exterior of the building, such as overhangs and louvers.

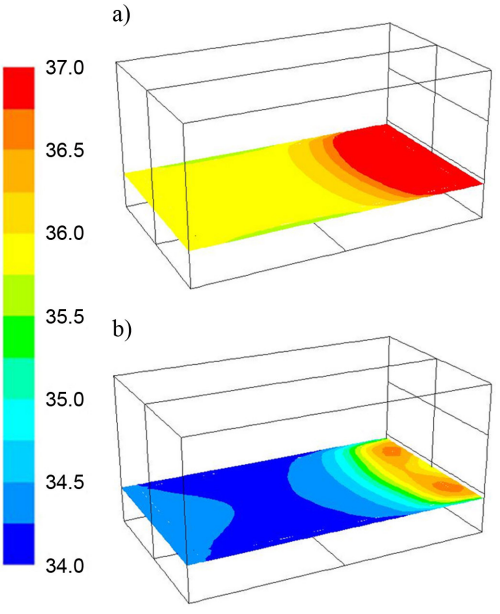

Fig. 13. *MRT at z = 0.6 m (sitting position) for a) Case C and b) Case D*

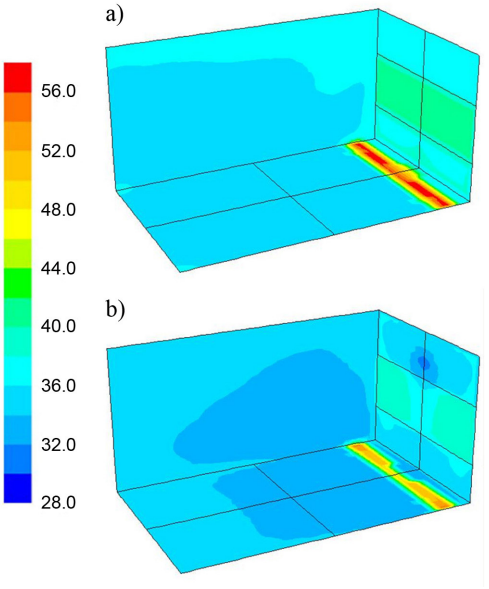

Fig. 14. *Surface temperatures for a) Case C and b) Case D*

It has to be emphasized that the implemented numerical simulation includes some simplifications as mentioned before. It was found in [17] that the presence of furniture in the room could induce complicated flow re-circulations and high local air velocities around the edges of the furniture. The study

also showed that there was little influence on room temperature and airflow buoyancy strength compared with that of an empty room. Including occupants, however, did have an impact on the temperature field through the formation of strong thermal plumes, with increased air temperature in comparison to the case of the unoccupied room.

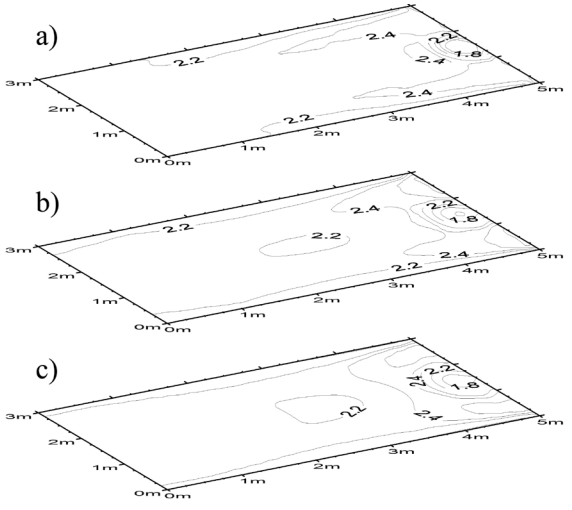

Fig. 15. *PMV values at three different levels for Case D; a) z = 1.7 m, b) z = 1.1 m, and c) z = 0.6 m*

3 CONCLUSION

In this paper, cooling of the indoor space is simulated using CFD software. Numerical analysis is used to calculate the fluid flow and the heat transfer in an indoor space. A steady state solution was achieved using an unsteady solver and resulted in air temperature distribution, mean radiant temperature, and air velocity field with or without the influence of solar radiation through the window. No additional heat sources were present in the room.

A theoretical analysis has shown that when certain boundary conditions are met, average values of air temperature and air flow velocity in the room can be in an acceptable range, although local distortions from standard optimal comfort values could exist. Considerable differences in thermal comfort conditions are observed in cooling periods, taking into account solar radiation through the window. In cases where solar radiation is included in the simulation, average temperatures in the room are approximately 4 °C higher than in cases without a solar radiation source. Furthermore, some differences were observed depending upon the air flow angle from the A/C unit, where a temperature drop in the lower layers occurred due to buoyancy effects. In this case, to eliminate the buoyancy effects, it is necessary to increase the air flow velocity from the A/C unit, which could lead to local air velocity distortions resulting in disturbed optimal comfort values.

Both measurement and CFD modeling revealed significant temperature rises of the floor area directly exposed to the sun. Although, a relatively small area, it greatly influences comfort conditions by raising the average temperature of the air and by introducing strong buoyancy.

Even though the simulation of the room is simplified by omitting occupants, furniture, and additional heat sources, it could be concluded that solar radiation is a very important factor in estimating comfortable thermal environments. To properly predict heat balance and comfort conditions in the room, it must be included in numerical simulations.

The presented numerical analysis can be relatively easily expanded to similar technical problems from the field of heating, ventilation and air-conditioning. It could also include air humidity internal heat sources, such as people, computers, monitors, etc. Furthermore, time-dependent boundary conditions could be included as a variable air flow outlet angle achieved by swinging flaps on an indoor A/C unit. Including those factors leads to more realistic simulations but a major limiting factor in simulating such, more complex problems is the available CPU power, i.e. calculation time.

4 NOMENCLATURE

C	constant
g	acceleration due to gravity, [m/s²]
H	height, [m]
k	turbulence kinetic energy, [m2/s²]
q	heat flux, [W/m²]
S	source term
t	time, [s]
T	temperature, [K]
u,v,w	velocity, [m/s]
x,y,z	Cartesian coordinates
α	heat transfer coefficient, [W/m²K]
Γ	diffusivity
ε	turbulent dissipation rate, [m²/s³]
ε	emissivity
λ	Thermal conductivity, [W/mK]
μ	dynamic viscosity, [Pa·s]
ν	kinematic viscosity, [m²/s]
ρ	density, [kg/m³]
σ	Stefan-Boltzmann constant, $5.67 \cdot 10^8$ [W/m²K⁴]

σ_k turbulent Prandtl number for k
σ_ε turbulent Prandtl number for ε
φ transported scalar
Φ angle, [°]

Subscripts
o outdoor
∞ radiation source
in inlet
int internal surface
ext external surface

5 REFERENCES

[1] Fanger, P.O., Melikov, A.K., Hanzawa, H., Ring, J. (1998). Air turbulence and sensation of draught. *Energy and Buildings*, vol. 12, no. 1, p. 21-39, **DOI:10.1016/0378-7788(88)90053-9**.

[2] Olesen, B.W., Parsons, K.C. (2002). Introduction to thermal comfort standards and to the proposed new version of EN ISO 7730, *Energy & Buildings*, vol. 34, no. 6, p. 537-548, **DOI:10.1016/S0378-7788(02)00004-X**.

[3] Stritih, U., Butala, V. (2011). Energy savings in building with a PCM free cooling system. *Strojniški vestnik - Journal of Mechanical Engineering*, vol. 57, no. 2, p. 125-134, **DOI:10.5545/sv-jme.2010.066**.

[4] Dovjak, M., Shukuya, M., Krainer, A. (2012). Exergy analysis of conventional and low exergy systems for heating and cooling of near zero energy buildings *Strojniški vestnik - Journal of Mechanical Engineering*, vol. 58, no. 7-8, p. 453-461. **DOI:10.5545/sv-jme.2011.158**.

[5] Rutman, E., Inard, C., Viličić, I., Franković, B., Bailly, A. (2000). A global approach of air conditioned indoor environment quality considering thermal comfort, acoustic comfort and air diffusion. *Energy and the Environment, Conference Proceedings*, vol. 2, p. 149-158.

[6] Rutman, E., Fournier, F., Jurkowski, R., Bailly, A., Franković, B., Viličić, I. (2002). Industrial approach for CFD modelling applications for air-conditioning and heat exchanger systems. *Energy and the Environment, Conference Proceedings*, vol. 2, p. 11-18.

[7] Wolf, I. (2010). *Numerical and Experimental Analysis of Thermal Comfort Parameters in an Air-Conditioned Room*, PhD thesis. University of Rijeka, Faculty of Engineering. (in Croatian)

[8] Dovrtel, K., Medved, S. (2011). Weather-predicted control of building free cooling system. *Applied Energy*, vol. 88, no. 9, p. 3088-3096, **DOI:10.1016/j.apenergy.2011.03.010**.

[9] Kuznik, F., Rusaouën, G., Hohotă, R. (2006). Experimental and numerical study of a mechanically ventilated enclosure with thermal effects. *Energy and Buildings*, vol. 38, no. 8, p. 931-938, **DOI:10.1016/j.enbuild.2005.08.016**.

[10] Sevilgen, G., Kilic, M. (2011). Numerical analysis of air flow, heat transfer, moisture transport and thermal comfort in a room heated by two-panel radiators. *Energy and Buildings*, vol. 43, no. 1, p. 137-146, **DOI:10.1016/j.enbuild.2010.08.034**.

[11] Aziz, M.A., Gad, I.A.M., Mohammed, E.S.F.A., Mohammed, R.H. (2012). Experimental and numerical study of influence of air ceiling diffusers on room air flow characteristics. *Energy and Buildings*, vol. 55, p. 738-746, **DOI:10.1016/j.enbuild.2012.09.027**.

[12] CEN Standard EN15251 (2007). *Indoor environmental input parameters for design and assessment of energy performance of buildings addressing indoor air quality, thermal environment, lighting and acoustics*. European Committee for Standardization, Bruxelles.

[13] ASHRAE Standard 55 (2010). *Thermal Environmental Conditions for Human Occupancy*. American Society of Heating Refrigeration and Air-Conditioning Engineers, Atlanta.

[14] ISO 7730 (2005). *Ergonomics of the Thermal Environment - Analytical Determination and Interpretation of Thermal Comfort using Calculation of the PMV and PPD Indices and Local Thermal Comfort Criteria*. International Organization for Standardization, Geneva.

[15] Olesen, B.W., Schoeler, M., Fanger, P.O. (1979). Discomfort caused by vertical air temperature differences. *Indoor Climate*, Fanger, P.O., Valbjorn, O., (eds.) Danish Building Research Institute, Copenhagen, p. 561-579

[16] ISO 7726 (1998). *Ergonomics of the Thermal Environment - Instrument for Measuring Physical Quantities*, International Organization for Standardization, Geneva.

[17] Horikiri, K., Yao, Y., Yao, J. (2015). Numerical optimisation of thermal comfort improvement for indoor environment with occupants and furniture. *Energy and Buildings*, vol. 88, p. 303-315, **DOI:10.1016/j.enbuild.2014.12.015**.

[18] Viličić, I., (1994). Energy modelling with meteorological parameters of test referent year. *Energy and the Environment, Conference Proceedings*, vol. 2, p. 525-534.

[19] Henkes, R.A.W.M., Hoogendoorn, C.J. (1994). Scaling of the turbulent natural convection flow in a heated square cavity. *Journal of Heat Transfer*, vol. 116, no. 2, p. 400-408, **DOI:10.1115/1.2911412**.

[20] Rouaud, O., Havet, M. (2002). Computation of the airflow in a pilot scale clean room using K-ε turbulence models. I*nternational Journal of Refrigeration*, vol. 25, no. 2, p. 351-361, **DOI:10.1016/S0140-7007(01)00014-7**.

[21] FLUENT 6.3 (2006). *User's Guide*, FLUENT Inc., New York.

[22] Patankar, S.V. (1980). *Numerical Heat Transfer and Fluid Flow*. Hemisphere, Washington DC.

[23] Fanger, P.O. (1970). *Thermal Comfort: Analysis and Applications in Environmental Engineering*. Mc Graw Hill, New York.

Strojniški vestnik - Journal of Mechanical Engineering 61(2015)11, 651-662

DOI:10.5545/sv-jme.2015.2562 Original Scientific Paper
Received for review: 2015-03-18
Received revised form: 2015-07-31
Accepted for publication: 2015-10-01

The Experimental Investigation of Effects of Multiple Parameters on the Formability of the DC01 Sheet Metal

Hakan Gürün* – İbrahim Karaağaç
Gazi University Faculty of Technology, Department of Manufacturing Engineering, Turkey

The formability of sheet metal materials through the deep drawing process is affected by various parameters, such as die chamber pressure, die radius and sheet thickness, all of which directly influence the product's quality. This paper investigates the formability of the DC01 sheet metal material. DC01 is a carbon steel sheet, which has a wide range of usages from the automotive industry to the manufacture of radiators by means of hydro-mechanical and conventional deep deep drawing methods. This study, for the first time, empirically investigates the effects of die chamber pressure, die radius and sheet thickness on the formability of DC01 sheet metal material through hydro-mechanical and conventional deep deep drawing methods. The study also helps to determine the forming parameters for this material. With regard to the hydro-mechanical deep drawing process, the drawing ratio increased from 2.16 to 2.33, solely due to an increase in die chamber pressure. The results of the experiment revealed suitable forming parameters through hydro-mechanical and conventional deep drawing methods for samples of DC01 material having a cylindrical geometry.

Keywords: deep drawing, hydro-mechanical deep drawing, conventional deep drawing

Highlights

- *The effects of die chamber pressure, die radius, and sheet thickness on the formability of DC01 sheet metal material were empirically investigated.*
- *The formability properties of DC01 sheet material were compared using conventional and hydro-mechanical deep drawing processes.*
- *The effect of each parameter and suitable parameter values were empirically identified and evaluated.*
- *The biggest drawing ratio in the hydro-mechanical deep drawing process was obtained as 2.33.*
- *The biggest drawing ratio in the conventional deep drawing process was obtained as 2.16.*
- *The maximum thickness change in the hydro-mechanical deep drawing process was observed to be a 12 % decrease.*

0 INTRODUCTION

The deep drawing process is widely used for forming sheet metal products. Medication and perfume tubes, pots and pans, household appliances, automotive parts and defence industry products are examples of the different applications of this process. In products formed using deep drawing, homogenous sheet thickness distribution and achievement of the highest drawing ratio is expected.

Conventional deep drawing is one of the most widely used sheet metal-forming methods for turning blank sheets into hollow pieces. The process includes forming the sheet metal with compression and tensile forces. In the process, the punch pulls the sheet material through the space between the punch and the die ring and shapes it [1]. In this process, the blank-holding slide transfers the blank-holding force via the blank holder onto the blank and the draw die. The die and the ejector are located in the lower die on the press bed. During forming, the blank holder brings the sheet metal into contact with the die, the punch descends from above into the die and shapes the part, while the sheet metal can flow without any wrinkling of the blank-holding area. In this case, the drawing process is carried out with a fixed blank holder and moving punch. The conventional deep drawing process is shown schematically, in Fig. 1.

When analysing previously performed studies, it was found that there are experimental-analytical and numerical research results. Through the finite element method (FEM), which is a numerical method, Volk et al. attempted to determine the optimal blank-holding force, through the finite element method, by changing the geometry and the structure of the blank holder. The best results were obtained with flexible, segmented blank holders [2]. Trzepieciński and Lemu worked on the effect of sheet metal surface roughness, lubricant conditions and sample orientation on the value of the friction coefficient in the draw-bead region of the sheet metal-forming processes. They ascertained several relationships showing the effect of surface profile and lubrication on the value of the friction coefficient. Simulations have been performed to study the stress/strain state in the stretched sample during draw-bead simulator tests [3]. Assempour and

*Corr. Author's Address: Gazi University Faculty of Technology, Department of Manufacturing Engineering, Turkey, hgurun@gazi.edu.tr

Taghipour worked to evaluate the effect of normal stress in the hydromechanical deep drawing (HDD) process. Analyses were carried out for axisymmetric elements of the formed cup-shaped part for increments of the punch travel. They found some differences between thickness values, radial and circumferential strains and stresses, and punch force under plane stress and three-dimensional stress conditions [4].

Numerical simulation methods were also used to aid in the development of the forming tool and the determination of the process parameter. Jurendić and Gaiani developed a numerical simulation method to aid in forming tool development and process parameter determination. They used the Barlat 1989 material model and employed an experimental strain-hardening curve to consider the anisotropic hardening of the material [5]. Garcia et al. used a Hill-48 associate plasticity model to analyse the modelling and experimental validation of the Erichsen test, a cylindrical cup test, and an industrial sheet metal-forming process [6].

The hydro-mechanical deep drawing process is forming using liquid pressure. Hydromechanical deep drawing (HDD), as a combination of conventional deep drawing with sheet hydroforming, has been widely used in the forming of complex-shaped sheet materials [7]. Onder and Tekkaya worked to determinate the optimum sheet metal-forming process and process parameters for various cross-sectional workpieces by comparing the numerical results of high-pressure sheet metal forming, hydromechanical deep drawing and conventional deep drawing simulations. The analyses revealed that certain processes are preferable for obtaining satisfactory products depending on the workpiece geometry and dimensional properties. Furthermore, it has been found that hydromechanical deep drawing is mostly suitable for deeper products where the flange is large [8]. Khandeparkar and Liewald worked on the advantages of hydro-mechanical deep drawing, such as increased deep drawing ratio, transfer of complex contours from a punch to the blank surface, reduction of drawing stages and better part quality. The process was simulated using the LS-DYNA FEM solver [9]. Sharma and Rout developed a finite element (FE) model for simulating the sheet hydromechanical forming process using LS-DYNA dynamic explicit commercial code. The analysis revealed that higher cup depth with minimum thinning, for forming dominated by stretching mode, can be achieved with material of a higher anisotropy ratio and strain hardening exponent by using a rough punch and

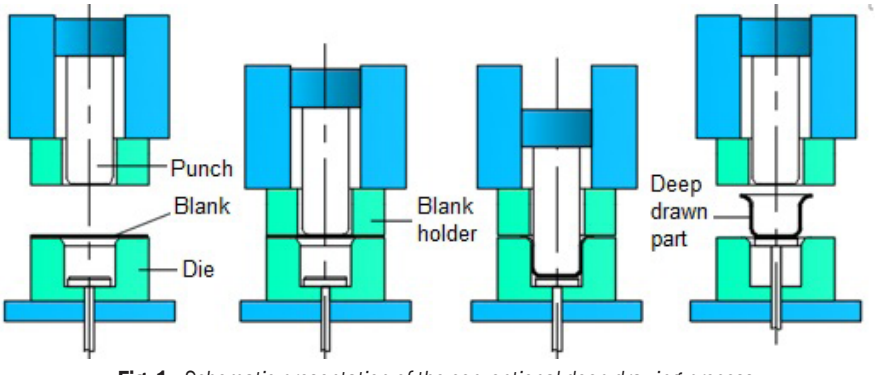

Fig. 1. *Schematic presentation of the conventional deep drawing process*

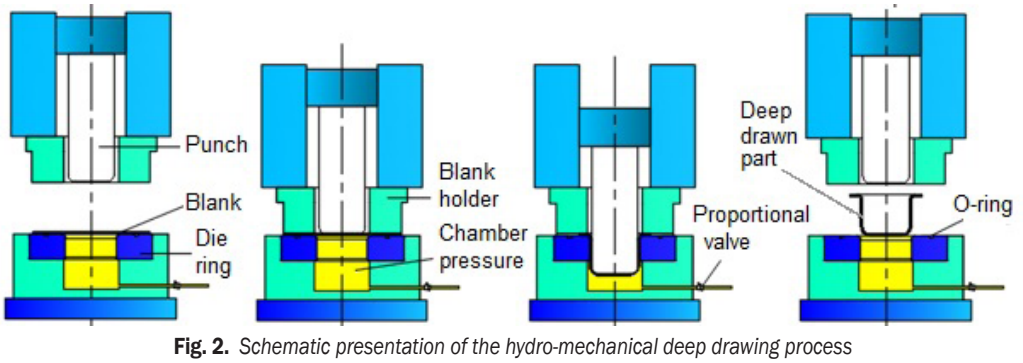

Fig. 2. *Schematic presentation of the hydro-mechanical deep drawing process*

effective lubrication at blank-die-blank holder interfaces [10].

As shown in Fig. 2, the lower die is a pressure medium reservoir or water container or chamber. The upper part of the die consists of the blank holder and the draw punch. In this process, to form the sheet metal the forming punch moves toward a high-pressure liquid mass in a controlled manner. As the drawing punch enters the chamber filled with the liquid, the pressure of the fluid starts to increase. During the deformation, the sheet material is pressed around the drawing punch. The pressure activated through the entry of the drawing punch into the pressured liquid has a multi-directional effect. Because of the pressure, the sheet material is forced to wrap around the punch. As a result of this force, the friction between the punch and the sheet material increases. This increase in the friction prevents the sheet material from irregularly tapering and being torn or cracked. As a result of the pressure inside the die, the drawing forces reach a higher level than what is expected from the conventional deep drawing process [11] and [12]. The hydro-mechanical deep drawing process is shown schematically, in Fig. 2.

With the use of the DC01 sheet material, many products in different sectors are being produced using the deep drawing process. Because the sheet material has widespread usage, it was chosen as the experimental material. The aim of this experimental study is to find the forming parameters that allow achieving the highest experimentally observed forming of a drawing ratio. Furthermore, it was aimed comparison of formability properties of DC01 sheet material using conventional and hydro-mechanical deep drawing processes in terms of drawing force. By identifying ideal forming parameters, trial and error, and the preparation that take place in the production of a product can be eliminated, reducing the product and die costs for similar geometry and forming parameters.

1 MATERIAL AND METHODOLOGY

1.1 Experimental Setup

Experimental studies were conducted using the experimental setup that was designed, produced and calibrated. The experimental setup was designed to be able to use both the conventional and hydro-mechanical forming processes and realize the process of data acquisition in real time while being controlled electromechanically.

In general, the experimental setup has three main parts: mechanical construction and dies; hydraulic power unit; and electronic control and data acquisition software. The experimental setup is shown in Fig. 3.

The mechanical components of the experimental setup are the main construction, forming punch, blank holder, die group, and a liquid chamber. A detailed schematic of the mechanical construction of the experimental setup, die group, and liquid chamber is shown in Figs. 4 and 5, respectively.

The electronic control of the experimental setup and data acquisition process is done through software and a data acquisition card. The imposed forming speed, punch displacement, blank holder force and chamber pressure are entered into the system through the designed software. Forming speed can be adjusted via the speed adjustment valves controlling the forming cylinders. The punch displacement is observed using the coordinate reader scale connected to the punch cylinder; when the displacement entered by the user is achieved, the process is complete. The

Fig. 3. *The experimental setup*

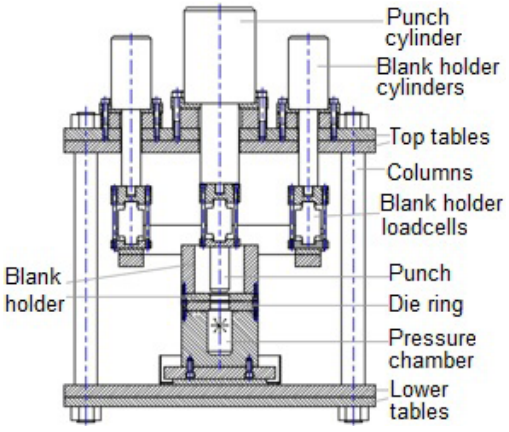

Fig. 4. *Detailed view of the mechanical construction of experimental setup*

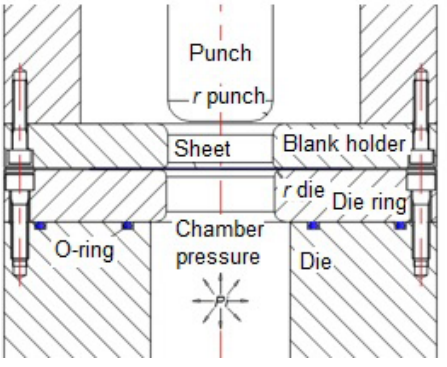

Fig. 5. *Detailed view of the die group and liquid chamber*

blank holder force can be observed and controlled via the pressure of the cylinders controlling the blank holder, which is adjusted using the pressure adjustment valve. The forces read from the load cells, according to the configured pressure value, are simultaneously observable using the software. The control of chamber pressure is done through the reading of data collected from a pressure transducer inside the die. This reading is compared to the value entered into the software, leading to the opening and closing of the proportional pressure valve that controls the pressure inside the die until the expected value is achieved. Fig. 6 shows a screenshot of the software designed for data acquisition and electronic control.

In the hydro-mechanical deep drawing experiments, hydraulic oil that conforms to ISO 11158 standard with a kinematic viscosity of 46 mm/s² at 40 °C (Hydro-Oil Aw 46, Petrol Ofisi, Turkey) was used as the forming liquid.

1.2 Experimental Study

In the experimental study, the parameters that are effective in the forming processes and that need to be inspected were primarily identified. The values of the identified parameters are:

- Sheet thickness, t [mm]: 0.5, 0.8 and 1.0.
- Die radius, r [mm]: 4, 6 and 8.
- Chamber pressure, p [MPa]: 10, 20 and 30.
- Initial blank diam. D [mm]: 120, 130 and 140.
- Punch shape and size: cylindrical, Ø60 mm.
- Punch velocity, v: 6 mm/s.

Mechanical and chemical specifications of the experimental material have been obtained through the identification of experimental parameters. To obtain the mechanical properties, tensile test samples

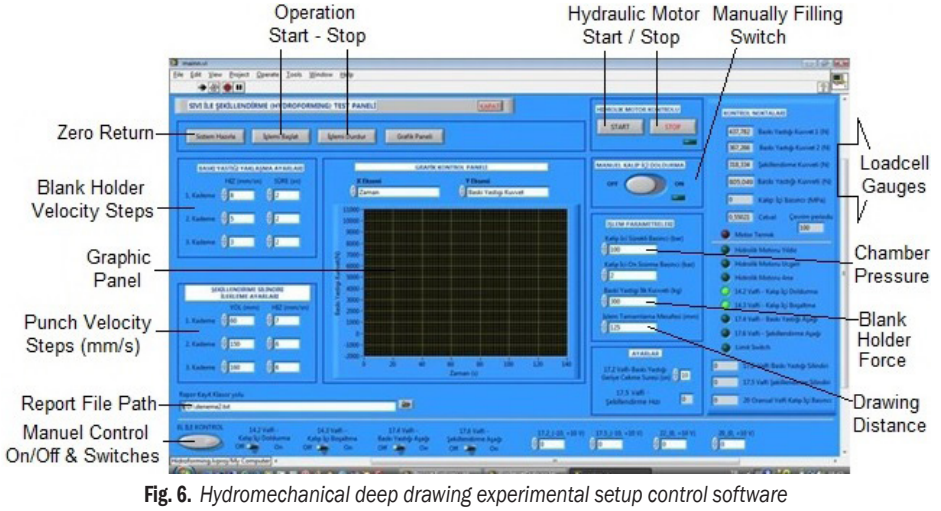

Fig. 6. *Hydromechanical deep drawing experimental setup control software*

with 1 mm sheet thickness in ASTM E8-M standards have been prepared in 0°, 45° and 90° to the rolling direction and have been subjected to tensile tests, which were done three times in each direction. Fig. 7 shows images of the experimental samples on which the tensile tests were done.

Fig. 7. *DC01 sheet material tensile test experimental samples*

The material in which the same properties are measured in any direction is termed isotropic, but most industrial sheets will show a difference in properties measured in test-pieces aligned with the rolling direction, and at 90° and 45° to the rolling direction. Different material properties working in different directions can have a significant effect on the degree of difficulty of the forming operation. In particular, the textures and orientation of the crystal structure to the rolling direction of the sheet metal lead to anisotropic directional behaviour. The anisotropy of the plastic behaviour of sheet metals is characterized by the Lankford's coefficient *r* **[13]**, which is determined by uniaxial tensile tests. In such tests, the ultimate tensile results are achieved in the rolling direction. In the case of a 45° direction, tensile stress decreased, and in the case of a 90° direction, the lowest values of tensile stress were obtained. The results of tensile tests were used only to determine the blank holder forces. The tensile stress values obtained as a result of the tests is shown in Table 2; the other properties of the sample are shown in Table 3, and the chemical composition of the material is shown in Table 4.

The recommended drawing speed value between 5 mm/s to 10 mm/s for hydro-mechanical deep drawing processes was found in the relevant literature **[14]** to **[18]**. In the experimental study, the drawing speed for the forming DC01 sheet material using hydro-mechanical deep drawing was kept constant at 6 mm/s. The blank holder force was kept constant during the experimental study. In the study, constant blank holder force values for both conventional and hydro-mechanical deep drawing processes were calculated separately. In the calculation of the blank holder pressure value used in the conventional deep drawing experiments Eq. 1 was used and in the calculation of the blank holder pressure value used in the hydro-mechanical deep drawing experiments Eq. 2 was used. In the calculation of blank holder forces for both processes, Eq. 3 was used. The blank holder forces used in experimental studies are given in Table 5.

Table 2. *Sample orientation with respect to roll direction*

DC01	Rolling Direction		
	0 °	45 °	90 °
	Ultimate tensile stress [MPa]		
1. Test	360.6	344.1	342.3
2. Test	356.5	344.8	339.6
3. Test	356.9	345.9	340.6

Blank holder pressure *p* **[1]**:

$$p = [(\beta-1)^2 + D/200t] \cdot (R_m/400), \quad (1)$$

$$p = 0.002\,[(\beta-1)^2 + D/200t] \cdot R_m, \quad (2)$$

where β is the drawing ratio, D is the initial blank diameter, t is sheet material thickness [mm] and R_m is the ultimate tensile stress.

Blank holder force F_{BH} **[1]**:

$$F_{BH} = (A_{BH})(p), \quad (3)$$

where A_{BH} is the area the blank holder is effective on the sheet material [mm^2] and p is the blank holder pressure.

The one-sided space measured between die and punch in deep drawing dies is called the drawing clearance. In the experimental studies, dies with different drawing clearances for each sheet material thickness ($t = 0.5$ mm, $t = 0.8$ mm, $t = 1.0$ mm) were

Table 3. *DC01 sheet material mechanical properties*

Material	Tensile stress [MPa]	Yield stress [MPa]	Elongation [%]	Modulus of elasticity [GPa]	Poisson rate	Specific gravity, [g/cm^3]
DC01	350.0	253.0	18.81	142.0	0.28	7.83

Table 4. *Chemical composition of DC01 sheet material*

Material	C [%]	Mn [%]	P [%]	S [%]	Cr [%]	Fe [%]	Others %
DC01	0.094	0.224	0.002	0.007	0.027	99.4	0.246

Table 5. *Blank holder forces*

	Hydro-mechanical deep drawing			Conventional deep drawing		
	Sheet thickness, *t*			Sheet thickness, *t*		
	0.5 mm	0.8 mm	1.0 mm	0.5 mm	0.8 mm	1.0 mm
Initial Blank Diameter	Blank Holder Force [kN]			Blank Holder Force [kN]		
120 mm	13.056	10.385	9.495	16.320	12.981	11.869
130 mm	19.448	15.885	14.697	24.310	19.856	18.372
140 mm	27.939	23.323	21.784	34.923	29.154	27.230

Table 6. *Experimental results obtained using the hydro-mechanical deep drawing process*

Sheet material: DC01	Die radius, *r*: 4 mm			Die radius, *r*: 6 mm			Die radius, *r*: 8 mm		
	Chamber pressure [MPa]			Chamber pressure [MPa]			Chamber pressure [MPa]		
	10	20	30	10	20	30	10	20	30
D: 120 mm, *t* = 1.0 mm	√	√	√	√	√	√	√	√	√
D: 130 mm, *t* = 1.0 mm	√	√	√	√	√	√	√	√	√
D: 140 mm, *t* = 1.0 mm	×	×	×	×	√	√	√	√	√
D: 120 mm, *t* = 0.8 mm	√	√	√	√	√	√	√	√	√
D: 130 mm, *t* = 0.8 mm	√	√	√	√	√	√	√	√	√
D: 140 mm, *t* = 0.8 mm	×	×	×	√	√	√	√	√	√
D: 120 mm, *t* = 0.5 mm	√	√	√	√	√	√	√	√	√
D: 130 mm, *t* = 0.5 mm	√	√	√	√	√	√	√	√	√
D: 140 mm, *t* = 0.5 mm	X	√	√	√	√	√	√	√	√

(√: Successful forming process, ×: Tearing and unsuccessful forming process)

produced. The calculation of the drawing clearances between the die and the punch is given by:

$$w = t + k\,, \tag{4}$$

where w is drawing clearance value [mm], t is sheet thickness [mm] and k is material constant (k = 0.07 mm for steel material **[1]** and **[13]**. The drawing-clearance values were calculated according to sheet material thickness and used in the experimental study.

Experimental studies have been conducted using both the conventional and the hydro-mechanical deep drawing processes according to the identified experimental parameters. In the study, 27 experiments for the conventional drawing process and 81 experiments for the hydro-mechanical deep drawing process were done. For trials using both methods, each experiment was repeated three times.

2 RESULTS

The results obtained from hydro-mechanical deep drawing experiments are shown in Table 6, and the results obtained from conventional deep drawing experiments are shown in Table 7. The obtained results have been evaluated according to the effects of chamber pressure, die radius, and sheet material thickness experimental parameters to the drawing ratio and the drawing force.

Table 7. *Experimental results obtained using the conventional deep drawing process*

Sheet Material: DC01	Die radius *r*: 4 mm	Die radius *r*: 6 mm	Die radius *r*: 8 mm
D: 120 mm, *t* = 1.0 mm	√	√	√
D: 130 mm, *t* = 1.0 mm	√	√	√
D: 140 mm, *t* = 1.0 mm	×	×	×
D: 120 mm, *t* = 0.8 mm	√	√	√
D: 130 mm, *t* = 0.8 mm	×	√	√
D: 140 mm, *t* = 0.8 mm	×	×	×
D: 120 mm, *t* = 0.5 mm	√	√	√
D: 130 mm, *t* = 0.5 mm	×	×	×
D: 140 mm, *t* = 0.5 mm	×	×	×

(√: Successful forming process, ×: Tearing and unsuccessful forming process)

The drawing ratio is the ratio of the maximum sheet diameter drawn without any wrinkling or tearing (D) to the punch diameter (d). The aim of the deep drawing process is to produce parts with no defects within the required tolerances. In the experimental studies, while a maximum drawing ratio of 2.33 was obtained using the hydro-mechanical deep drawing

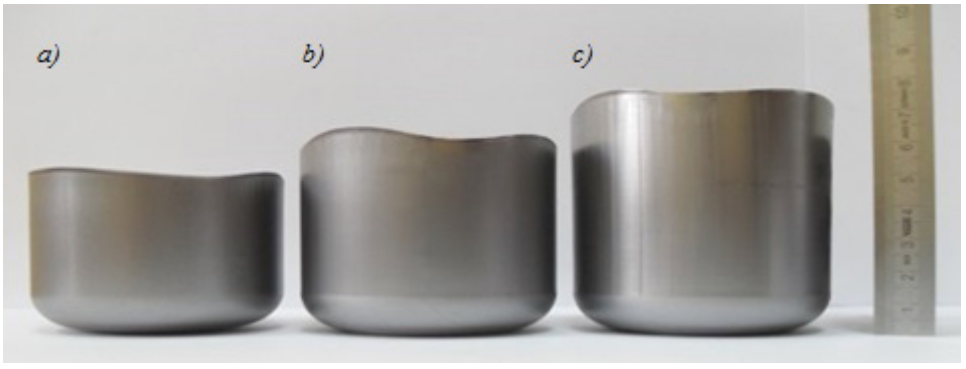

Fig. 8. *Parts formed at different drawing ratios from DC01 sheet material; a) β = 2, b) β = 2.16, c) β = 2.33*

process, a maximum drawing ratio of 2.16 was obtained using the conventional deep drawing process. More than one reason was observed for the fact that the drawing ratio for the hydro-mechanical deep drawing is larger than that for the conventional drawing process. In the hydromechanical deep drawing process, as the forming medium is lubricated, the friction between the sheet material and the die lessens, and the forming process becomes easier. In contrast, the pressure created inside the die presses the sheet metal into the punch, increasing the friction between the sheet metal and the punch, thus preventing it from tearing as a result of non-homogeneous thinning of the material. As the pressure inside the die is the same on the sheet material from all directions, non-homogeneous thinning is again prevented. Another function of the pressure inside the die is observed as the die radius friction is reduced, and the forming is improved, resulting from the sheet material being pressured toward the punch. The effect of chamber pressure was observed clearly in the experimental study regarding the hydro-mechanical deep drawing process. In this study, while for 0.5 mm sheet material thickness, a 4 mm die radius and 10 MPa chamber pressure, a maximum of 2.16 drawing ratio could be obtained, as the chamber pressure was increased to 20 MPa, a maximum of 2.33 drawing ratio was obtained. In another experimental group, while at 1.0 mm sheet material thickness, 6 mm die radius and 10 MPa chamber pressure a maximum drawing ratio of 2.16 could be obtained, as the chamber pressure was increased to 20 MPa, a maximum drawing ratio of 2.33 was obtained. Images of sheet materials shaped in different drawing ratios in the experimental study are shown in Fig. 8. It was observed that as the chamber pressure is increased, the drawing force is increased, this being a result of the force being in the reverse direction of the punch movement. The punch forces obtained using 0.5 mm, 0.8 mm, and 1 mm sheet material thicknesses with 4 mm die radius and 120 mm initial sheet material diameter at chamber pressures of 10 MPa, 20 MPa, and 30 MPa in the experimental studies are given in Fig. 9.

Table 8. *Punch forces of the conventional deep drawing process, kN*

Sheet Material: DC01	Die radius *r*: 4 mm	Die radius *r*: 6 mm	Die radius *r*: 8 mm
D: 120 mm, *t* = 1.0 mm	101.493	96.163	89.642
D: 130 mm, *t* = 1.0 mm	115.426	110.665	106.382
D: 140 mm, *t* = 1.0 mm	Tearing	Tearing	Tearing
D: 120 mm, *t* = 0.8 mm	99.718	94.588	82.726
D: 130 mm, *t* = 0.8 mm	Tearing	104.472	99.926
D: 140 mm, *t* = 0.8 mm	Tearing	Tearing	Tearing
D: 120 mm, *t* = 0.5 mm	58.625	56.384	54.447
D: 130 mm, *t* = 0.5 mm	Tearing	Tearing	Tearing
D: 140 mm, *t* = 0.5 mm	Tearing	Tearing	Tearing

When the die radius value is increased, the sheet material's flow into the die becomes easier and the drawing ratio increases while the tensile force decreases. As a small die radius creates resistance to the sheet metal material flow in the opposite direction to the shear direction during forming; this situation makes the forming of the sheet material more difficult. As a result of this, thinning of the sheet material and, in the end, tears were observed. In the experimental studies, regarding both the hydro-mechanical deep drawing process and the conventional deep drawing process, the effect of die radius can be observed clearly. In the hydro-mechanical deep drawing process, while sheet materials of 0.5 and 0.8 mm thickness cannot be formed using 140 mm initial sheet material diameter and 10 MPa chamber pressure with 4 mm die radius, as the die radius is increased to 6 mm and 8 mm they can be successfully formed.

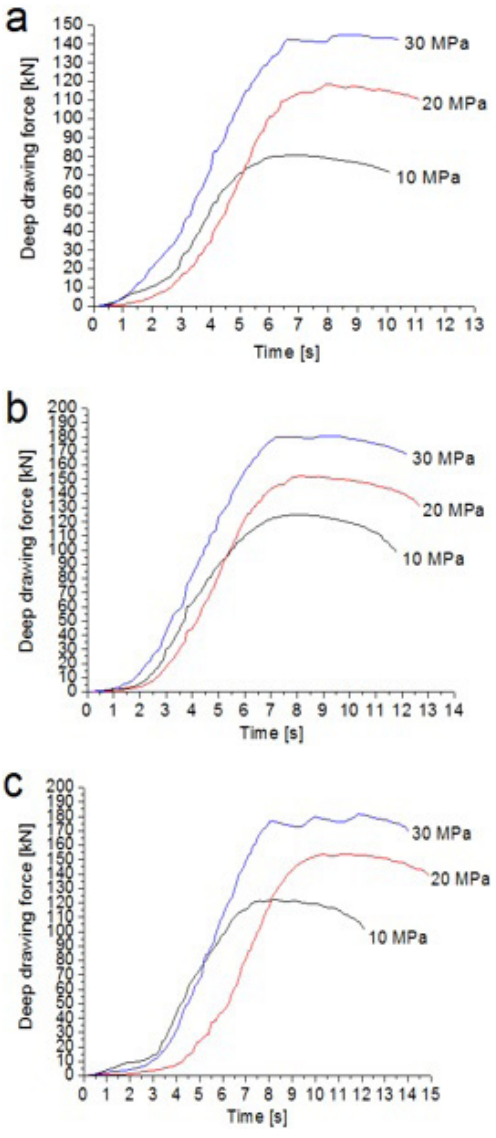

Fig. 9. *Deep drawing force at different sheet material thicknesses and chamber pressures; a) t = 0.5 mm, b) t = 0.8 mm, c) t = 1.0 mm*

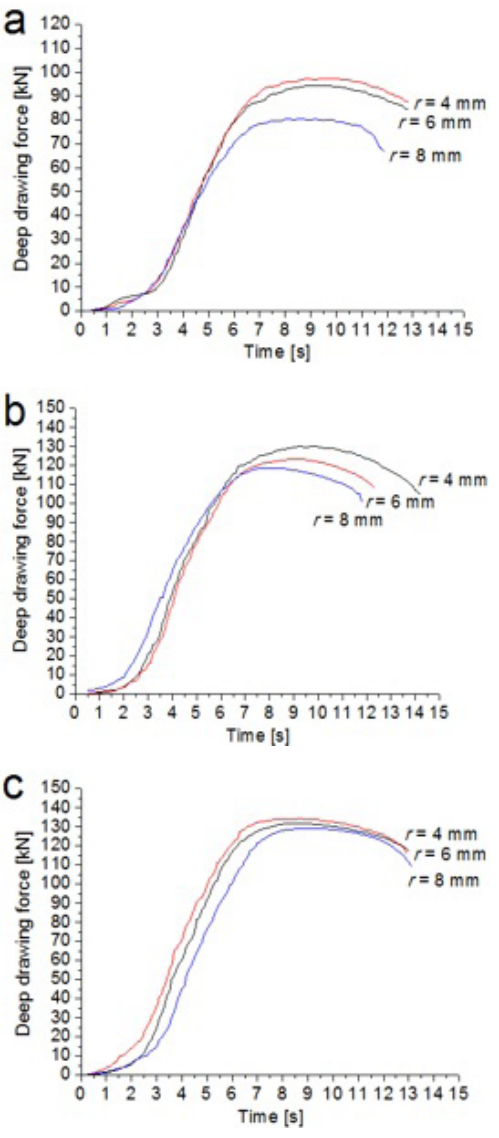

Fig. 10. *Forming forces at different die radius measures (D=130 mm, p=10 MPa); a) t=0.5 mm, b) t=0.8 mm, c) t=1 mm*

In the conventional deep drawing process, while 0.8 mm sheet material thickness, a 130 mm initial sheet material diameter experimental sample could not be formed with a 4 mm die radius when the die radius value was increased to 6 mm, the forming process could be completed. In Fig. 10, the forming forces, obtained at different die radius values belonging to forming studies at different die radii are shown. The punch forces obtained from conventional deep drawing processes have been given in Table 8.

It can be observed that as sheet material thickness increases, the drawing ratio increases. The drawing ratio for sheets with smaller thicknesses decreases during forming because the sheet material is more prone to wrinkling [19]. It was observed that the increase in sheet material thickness increases the formability in forming with conventional deep drawing. However, in the hydro-mechanical deep drawing process, it was found that chamber pressure must be increased depending on the sheet material thickness increase. When the liquid pressure was not being increased, it was found that the hydraulic liquid pressure was not enough to pressure the sheet material onto the punch. Furthermore, insufficient

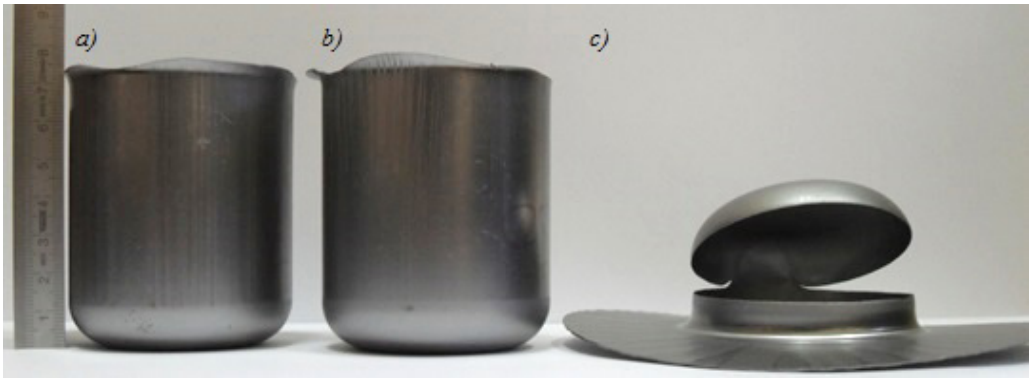

Fig. 11. *Forming studies at different die radii using hydro-mechanical deep drawing process-1; D = 140 mm, p = 10 MPa, t = 0.5 mm, a) r = 8 mm, b) r = 6 mm, c) r = 4 mm*

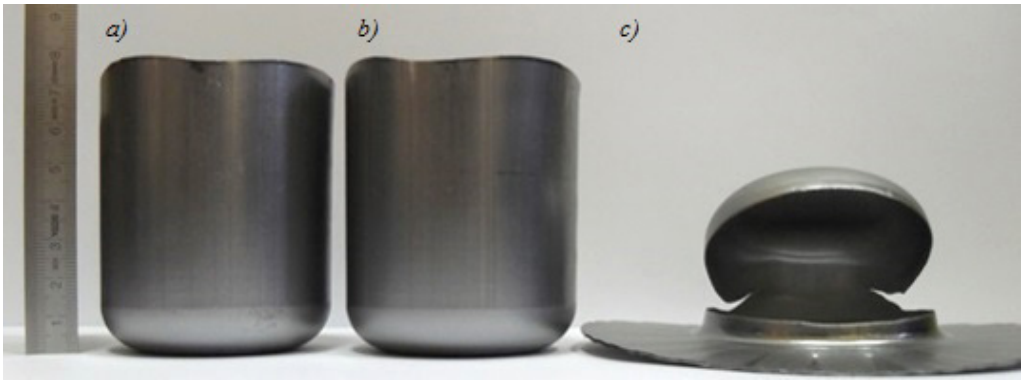

Fig. 12. *Forming studies at different die radii using hydro-mechanical deep drawing process-2 D = 140 mm, p = 10 MPa, t = 0.8 mm, a) r = 8 mm, b) r = 6 mm, c) r = 4 mm*

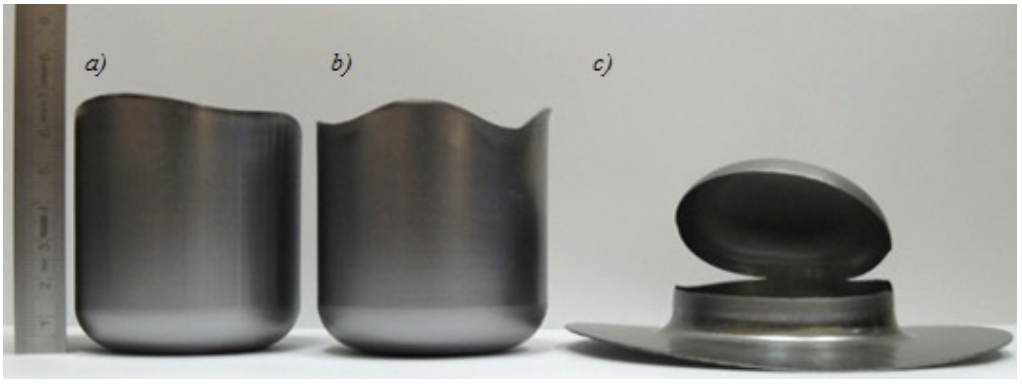

Fig. 13. *Forming studies at different die radii using conventional deep drawing process D = 130 mm, t = 0.8 mm, a) r = 8 mm b) r = 6 mm c) r = 4 mm*

pressure causes a large contact area on the die radius. In this case, the effect of the most important parameter of the hydro-mechanical forming process, chamber hydraulic liquid pressure decreases, and the positive effect chamber pressure provides to the forming process cannot be fully observed. In the deep drawing process, a thickness increase in the sheet material postpones wrinkling and lets the sheet material be better formed without wrinkling. Using the conventional deep drawing processes, sheet metal cannot be formed using 0.5 mm thick sheet material, although when using 0.6 mm and 1.00 mm thick sheets, the forming process can be completed. It was found that this situation is caused by the thin sheet material starting to wrinkle and tearing right at the beginning of the forming process.

In the deep drawing process, tearing is an important aspect: tears with higher amplitude were observed in the conventional deep drawing process.

In the formability of sheet metal materials, the control of thickness change is an important parameter that can affect product quality. Minimum thickness change indicates that the forming of the product has been done successfully. Cups with the maximum drawing ratio value obtained in experimental studies were cut on a wire EDM in order to examine thickness change, which were measured from the measurement points indicated in Fig. 14a using a 0.01 sensitive micrometer. Measurement results are given in Fig. 14b.

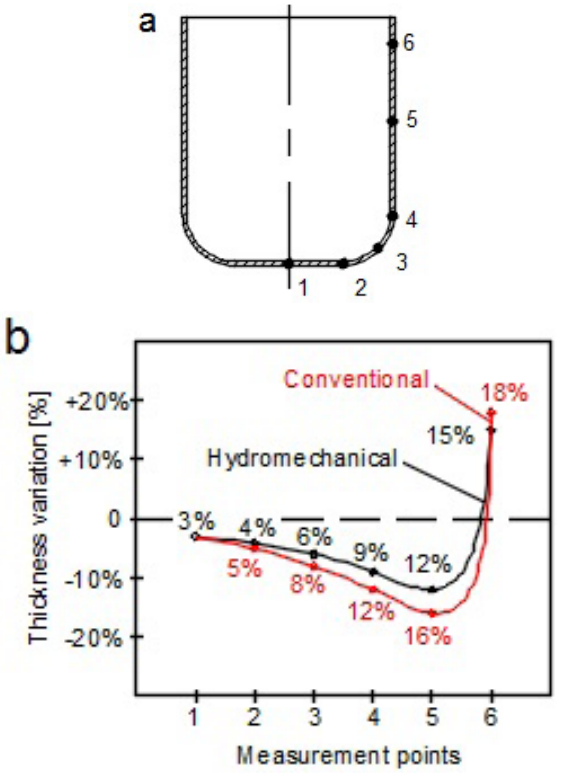

Fig. 14. *Thickness variation measurements of DC01 sheet material a) measurement points, b) measurement results*

Maximum thickness thinning was observed at the ending points of the punch radius (4th point) and wall (5th point) for both processes. However, an increase in thickness was observed at the flanges (6th point). In the hydro-mechanical deep drawing method, because the contact to sheet material shaped by the liquid is the same in every direction, the unstable thinning of the sheet material is prevented; thus, thickness change is more homogeneous compared to the conventional deep drawing process.

In the investigation of the experimental specimens' thickness change, it was observed that the thinning in thickness change did not exceed 12% in the hydro-mechanical deep drawing process. This result shows that thickness change in the product is considerably homogeneous compared to the conventional forming method.

3 DISCUSSIONS

This is the first study in which the effects of parameters such as die radius, sheet thickness and die chamber pressure affecting the formability of DC01 sheet metal material through hydro-mechanical and conventional deep drawing methods are together empirically investigated. The rate of the effect of each parameter and suitable values of these parameters were empirically identified and evaluated. The results of the study are provided below.

Die chamber pressure is a key parameter in the forming processes of the hydro-mechanical deep drawing method. Prebulge pressure is usually applied in the hydro-mechanical deep drawing method in order to avoid and decrease in advance the sheet material contacting the die radius, thus helping to increase the drawing ratio. In the empirical study, die chamber pressure tended to increase once the punch penetrated into the die. The present study yielded the smallest die radius of 4 mm and a drawing ratio of 2.33 at the smallest die thickness of 0.5 mm for DC01 sheet material, although prebulge pressure had been applied in advance. In conventional drawing experiments, the highest drawing ratio, 2.16, was obtained in 0.8 mm and 1.0 mm thick sheets, which are the higher sheet thicknesses, or in bigger die radiuses.

Die chamber pressure, die radius, and sheet material thickness affect the forming force. In the hydro-mechanical deep drawing method, a higher drawing force is obtained because the die chamber pressure generates a reverse force on the punch. If the die chamber pressure is increased by 10 MPa, the forming force increases by approximately 30 kN. An increase in the die radius causes a decrease in the forming force. This arises because the sheet material is exposed to less tension at a higher die radius size. Where die radius increases by 2 mm, forming force decreases by approximately 5 kN.

Because the forming environment using the hydro-mechanical deep drawing method is very efficiently lubricated, there is little friction between the sheet material on the die (flange region) and the die. Moreover, because there is a pressured thin fluid layer between the die and the sheet material, the sheet

material has decreased contact with the die radius. This contributes to obtaining better surface quality in the parts that are formed. Although the empirical studies did not go as far as extremely high die chamber pressure values (>30 MPa), the sheet material could be drawn to the end without any wrinkles on it. In the conventional forming methods, however, scratches appearing on the punch along with the scratches and burrs on the sheet material are among the factors that decrease formability and surface quality.

The thickness of sheet material is an important parameter in the drawing and forming processes. Die chamber pressure and sheet material thickness are closely related parameters, and die chamber pressure must be specified according to sheet material thickness during the hydro-mechanical deep drawing process. Die chamber pressure in the hydro-mechanical deep drawing process must have a value that will uniformly press the sheet material on the punch and decrease its contact with the die radius. Otherwise, the impact of the hydro-mechanical deep drawing process could not be notably observed. In empirical studies, the biggest drawing ratio, 2.16, was obtained in 0.8 mm thick sheet material and at a die radius of 4 mm under 20 MPa of die chamber pressure, while a drawing ratio of 2.33 was obtained in the 0.5 mm thick sheet material under the same conditions. It was due to the fact that the effect of die chamber pressure increases as the sheet material thickness decreases.

As the value of the die radius increases, the formability of the sheet material also increases. However, the impact of the die radius may decrease in the hydro-mechanical deep drawing method under high die chamber pressure in case of elimination of the contact between the die radius and the sheet material due to the pressure. In the empirical studies, the effect of the die radius was fully observed in both methods. It was also observed that as the die radius increases, the drawing ratio increases in both methods, while the forming force decreases.

The desired end product cannot be obtained taking into account a single parameter in the forming processes through hydro-mechanical and conventional deep drawing methods. As indicated by the empirical studies, die chamber pressure, die radius and sheet material thickness parameters are interrelated and cannot be considered separately. In the forming processes in which all these parameters are taken into account, the biggest drawing ratio, 2.33, in the hydro-mechanical deep drawing process, and the biggest drawing ratio, 2.16, in the conventional deep drawing process were obtained in a pressure range of 0 to 30 MPa for DC01 sheet material.

4 CONCLUSIONS

The following shows the results obtained from the experimental study.

- Die chamber pressure, die radius and sheet material thickness parameters are interrelated parameters, and cannot be considered separately.
- The biggest drawing ratio, 2.33, in the hydro-mechanical deep drawing process was obtained in a pressure range of 0 MPa to 30 MPa for DC01 sheet material.
- The biggest drawing ratio, 2.16, in the conventional deep drawing process was obtained.
- In the hydro-mechanical deep drawing process, the forming force rises with increasing chamber pressure.
- An increase in the die radius causes a decrease in the forming force.
- In the hydro-mechanical deep drawing method, the forming environment is very efficiently lubricated. This situation allows the sheet material to be drawn to the end without any wrinkling.
- Die chamber pressure and sheet material thickness are closely related parameters, and die chamber pressure must be specified according to sheet material thickness during a hydro-mechanical deep drawing process.
- The thickness change in the hydro-mechanical deep drawing process was observed as a maximum 12 % decrease. This phenomenon has a lower value than thickness decreases in parts formed by the conventional deep drawing method.

5 ACKNOWLEDGEMENTS

The present work is supported by the Gazi University Scientific Research Department with project number 07/2010-31.

6 REFERENCES

[1] Tschaetsch, H. (2006). *Metal Forming Practise*. Springer Verlag, Berlin, Heidelberg.

[2] Volk, M., Nardin, B., Dolšak, B. (2011). Application of numerical simulations in the deep drawing process and the holding system with segments' inserts. *Strojniški vestnik - Journal of Mechanical Engineering*, vol. 57, no. 9, p. 697-703, **DOI:10.5545/sv-jme.2010.258**.

[3] Trzepieciński, T., Lemu, H.G. (2014). Frictional conditions of AA5251 aluminium alloy sheets using drawbead simulator tests and numerical methods. *Strojniški vestnik - Journal of Mechanical Engineering*, vol. 60, no. 1, p. 51-60, **DOI:10.5545/sv-jme.2013.1310**.

[4] Assempour, A., Taghipour, E. (2011). The effect of normal stress on hydro-mechanical deep drawing process. *International Journal of Mechanical Sciences*, vol. 53, no. 6, p. 407-416, **DOI:10.1016/j.ijmecsci.2011.03.003**.

[5] Jurendić, S., Gaiani, S. (2013). Numerical simulation of cold forming of α-titanium alloy sheets. *Strojniški vestnik - Journal of Mechanical Engineering*, vol. 59, no. 3, p. 148-155, **DOI:10.5545/sv-jme.2012.415**.

[6] Garcia, C., Celentano, D., Flores, F., Ponthot, J.-P., (2006). Numerical modelling and experimental validation of steel deep drawing processes. Part I. Material characterization. *Journal of Materials Processing Technology*, vol. 172, no. 3, p. 451-460, **DOI:10.1016/j.jmatprotec.2005.11.015**.

[7] Janbakhsh, M., Riahi, M., Djavanroodi, F. (2013). A practical approach to analysis of hydro-mechanical deep drawing of superalloy sheet metals using finite element method. *International Journal of Advanced Design and Manufacturing Technology*, vol. 6, no. 1, p. 1-7.

[8] Onder, E., Tekkaya, A.E. (2008). Numerical simulation of various cross sectional workpieces using conventional deep drawing and hydroforming technologies. *International Journal of Machine Tools & Manufacture*, vol. 48, no. 5, p. 532-542, **DOI:10.1016/j.ijmachtools.2007.06.012**.

[9] Khandeparkar, T., Liewald, M. (2008). Hydromechanical deep drawing of cups with stepped geometries. *Journal of Materials Processing Technology*, vol. 202, no. 1-3, p. 246-254, **DOI:10.1016/j.jmatprotec.2007.08.072**.

[10] Sharma, A.K., Rout, D.K. (2009). Finite element analysis of sheet Hydromechanical forming of circular cup. *Journal of Materials Processing Technology*, vol. 209, no. 3, p. 1445-1453. **DOI:10.1016/j.jmatprotec.2008.03.070**.

[11] Consulting editor: Altan, T. (1998). *Metal Forming Handbook,* Schuler Springer Verlag Berlin Heidelberg.

[12] Zhang, S.H., Wang, Z.R., Xu, Y., Wang, Z.T., Zhou, L.X. (2004). Recent developments in sheet hydroforming technology. *Journal of Materials Processing Technology*, vol. 151, no. 1-3, p. 237-241, **DOI:10.1016/j.jmatprotec.2004.04.054**.

[13] Banabic, D., Bunge, H.-J., Pohlandt, K., Tekkaya, A.E. (2000). *Formability of Metallic Materials*. Springer Verlag, Berlin, Heidelberg, DOI:**10.1007/978-3-662-04013-3**.

[14] Choi, H., Ni, J., Koc, M. (2007). A study on the analytical modelling for warm hydro-mechanical deep drawing of lightweight materials. *International Journal of Machine Tools & Manufacture*, vol. 47, p. 1752-1766, **DOI:10.1016/j.ijmachtools.2006.12.005**.

[15] Zhang, S.H., Lang, L.H., Kang, D.C., Danckert, J., Nielsen, K.B. (2000). Hydromechanical deep drawing of aluminium parabolic workpieces-experiments and numerical simulation. *International Journal of Machine Tools & Manufacture*, vol. 40, no. 10, p. 1479-1492, **DOI:10.1016/S0890-6955(00)00006-7**.

[16] Zhang, S.H., Jensen, M.R., Nielsen, K.B., Danckert, J., Lang, L.H., Kang, D.C. (2003). Effect of anisotropy and prebulging on hydro-mechanical deep drawing of mild steel cups. *Journal of Materials Processing Technology*, vol. 142, no. 2, p. 544-550, **DOI:10.1016/S0924-0136(03)00656-3**.

[17] Dachang, K., Yu, C., Yongchao, X. (2005). Hydromechanical deep drawing of superalloy cups. *Journal of Materials Processing Technology*, vol. 166 no. 2, p. 243-246, **DOI:10.1016/j.jmatprotec.2004.08.024**.

[18] Zhang, S.H., Nielsen, K.B., Danckert, J., Kang, D.C., Lang, L.H. (2000). Finite element analysis of the hydro-mechanical deep drawing process of tapered rectangular boxes. *Journal of Materials Processing Technology*, vol. 102, no- 1-3, p. 1-8, **DOI:10.1016/S0924-0136(99)00446-X**.

[19] Hezam, L.M.A., Hassan, M.A., Hassab-Allah, I.M., El-Sebaie, M.G. (2009). Development of a new process for producing deep square cups through conical dies. *International Journal of Machine Tools & Manufacture*, vol.49, no. 10, p. 773-780, **DOI:10.1016/j.ijmachtools.2009.04.001**.

Strojniški vestnik - Journal of Mechanical Engineering 61(2015)11, 663-668
DOI:10.5545/sv-jme.2015.2772
Original Scientific Paper
Received for review: 2015-06-17
Received revised form: 2015-09-28
Accepted for publication: 2015-10-06

A Study of Disorder Shell Effects on the Mechanical Properties of SiC Nanowires

Bin Zheng* – Huiling Du
[1]Xi'an University of Science and Technology, School of Materials Science and Engineering, China

The mechanical properties of SiC nanowires were investigated using molecular dynamics simulation method. The results show that the disorder shell layer reduced the elastic modulus of SiC nanowires. This reduction mainly depends on the thickness and the atomic type of the disorder shell. Thicker C and Si disorder layers can strengthen and weaken the nanowires, respectively. Also, the core-shell wires have size-dependent strength, which can be understood by examining the variation of Young's modulus and the volume fraction of the isolated core and isolated shell. Furthermore, the disorder coating was found to facilitate the brittle-ductile transition in the SiC core. The simulation results are expected to help the design and manufacturing of complex nanoscale architectures with desired mechanical properties.
Keywords: core/shell nanowire, mechanical properties, Young's modulus, molecular dynamics simulation

Highlights
- *The disorder shell layer reduces the elastic modulus of SiC nanowires.*
- *Thicker C and Si disorder layers can strengthen and weaken the nanowires, respectively.*
- *The bigger the SiC core, the larger Young's modulus of the core-shell nanowires.*
- *The modulus of the crystal core dominates the strength of the whole wire.*
- *The disorder shell induces the amorphization of the crystal core and makes the semiconductor core-shell nanowires ductile.*

0 INTRODUCTION

The core-shell heterostructure of nanomaterials is critical to the extraordinary tunability of the properties of nanomaterials [1]. The crystalline phase structure has been the subject of many experimental investigations. More recently, crystalline core-disorder shell materials have attracted attention, owing to their interface boundary effect applied in lithium ion batteries and high-conversion energy solar cell devices [2] and [3].

The application performance of crystalline-disorder core-shell materials depends on their stable mechanical properties. Recently, there has been considerable interest in studying the effect of the core-shell interface on the mechanical properties of nanowires (NWs) [4] and [5]. Some investigations have shown that high internal stress gradients, owing to lattice mismatch, develop at the interface, which then results in an unusual deformation mechanism in metallic nanomaterials [6]. For brittle semiconductor materials, the disorder shell is considered to play a significant role in stabilizing the crystalline core [7] and [8] and in dominating the brittle-ductile (B-D) transition [9]. Therefore, the core-shell structure can modulate the elastic modulus of NWs and induce plastic deformation. Despite the progress in understanding the mechanical deformation of core-shell NWs, knowledge of the tuneable properties of such nano-hetero-structures remains limited.

In this paper, we focused on the mechanical properties of core-shell NWs with silicon carbide (SiC) crystalline core and disorder carbon (*d*-C) or silicon (*d*-Si) shell, which have been synthesized experimentally by many routes [10] and [11]. We performed calculations for the SiC-*d*-C and SiC-*d*-Si core-shell NWs to evaluate their mechanical properties and to understand the core-shell interface effect.

1 SIMULATION MODEL

The simulation model consists of the [111]-oriented 3C–SiC crystalline core and the disorder layer. We built the atomic model of the SiC core with a hexagonal cross section (Fig. 1). The size of the nanowire cores (1 nm, 1.3 nm, and 1.7 nm diameters) is defined as the average from the centre to the corner and edge distances. To obtain the disorder shell, crystalline C and Si diamond specimens were heated above their melting points (C: 3820 K and Si: 2500 K), and then cooled to room temperature at 200 K/picosecond (ps) to obtain disorder bulk materials for cutting the hexagonal disorder shells [12] and [13]. Subsequently, core-shell NWs were assembled (Fig. 1) by inserting the crystalline core into disorder shells with thicknesses of 0.3 nm, 0.6 nm, and 0.9 nm. An initial distance of 0.15 nm between core and shell was designed for interface structure relaxation.

*Corr. Author's Address: Xi'an University of Science and Technology, Xi'an, PR China, zhengbin@xust.edu.cn

Molecular dynamics (MD) simulations were used to perform uniaxial deformation under simulated quasistatic conditions and to obtain the mechanical properties of SiC-disorder core-shell NWs. The LAMMPS software [14] with a time step of 1 femtosecond (fs) was used to carry out the MD simulations. Before loading, two order steps were performed to establish the atomic rearrangement of the free surface or the core-shell interface. First, energy minimization based on the conjugate gradient (CG) algorithm was used to guarantee the atomic optimization position at zero temperature. Second, the internal stresses of the initial nanostructure were released by relaxation under constant atmosphere pressure for 1 ns and constant volume for another 1 ns to thermally equilibrate the system at 300 K using a Nosé-Hoover thermostat [15] and [16]. In a stepwise manner, the compressive force was loaded along the axial direction with periodic boundary conditions. For each step, the uniform displacement increment was 0.1 nm and the relaxation time at constant temperature was 500 ps. An equivalent 0.2 m/s (0.002 % ps^{-1}) compressive rate was obtained. No significant difference appeared when the compressive rate decreased to 0.1 m/s (0.001 % ps^{-1}). All the reported numerical simulations were performed using the Tersoff potential for C, Si, and SiC, where the total energy of the system with one-body, two-body, and three-body contributions and testing indicated its transferability from the molecular to the bulk regime, making it a good choice for atomistic simulations [17].

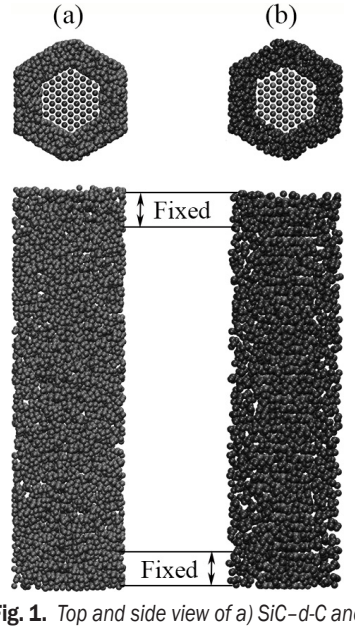

Fig. 1. *Top and side view of a) SiC–d-C and b) SiC–d-Si core-shell nanowire*

In the simulations, uniaxial loading was applied along the z direction. The reported stresses (σ^{zz}) were calculated by summing the stress tensor (f_i^z) of all atoms along the *z*-direction and then dividing them by the volume of the system (V), as shown in Eq. (1). The volume V is the product of the hexagonal cross-sectional area and the equilibrium length in every loading step. For strain from –3.0 % to 3.0 %, linear regression, and the stress-strain curves were used to estimate Young's modulus (Y) with Eq. (2).

$$\sigma^{zz}=\frac{1}{V}\sum_{i}^{N} f_i^z, \tag{1}$$

$$\sigma^{ZZ}=Y\varepsilon_Z. \tag{2}$$

2 RESULTS AND DISCUSSION

The stress–strain curves for SiC-disorder core-shell nanowire materials loaded both in compression and tension are shown in Fig. 2, from which we find the typical characteristics of the mechanical properties of semiconductor nanowires: ultra-strength and super ductility. Their elastic strains are larger than 3 %, and failure strength reaches to above 10 GPa for all nanowires. Also, Fig. 2 shows the tuneable mechanical properties of the nanowires through the thickness and the type of shell layer.

Young's modulus can be extracted from the stress-strain curves, as shown in Table 1. The elastic strength of wires was compared with the different sizes of core and shell. Furthermore, the Si core was employed to show the effect of the disorder shell on Young's modulus of core/shell NWs.

From Table 1, it is clear that Young's modulus of naked NWs is bigger than that of wires coated with disorder layers; this observation is consistent with previous reports [18].

Previous publications [1] showed that the high internal stress gradients, owing to lattice mismatch, exist at the core/shell interface, which can change the mechanical properties of the wires, although the shell layers are crystallized structures. In this work, the shell layer becomes a disordered structure, which potentially will saturate those dangling bonds on the core surface due to no limitation of the lattice. The atomic stress distribution will be analyzed to understand the strength of the wires coated by the disorder shell, as shown in Fig. 3.

From Fig. 3a, we found that most of the atoms in naked NW are under compressive stress state (peak 1). All those atoms located on the surface of the nanowire

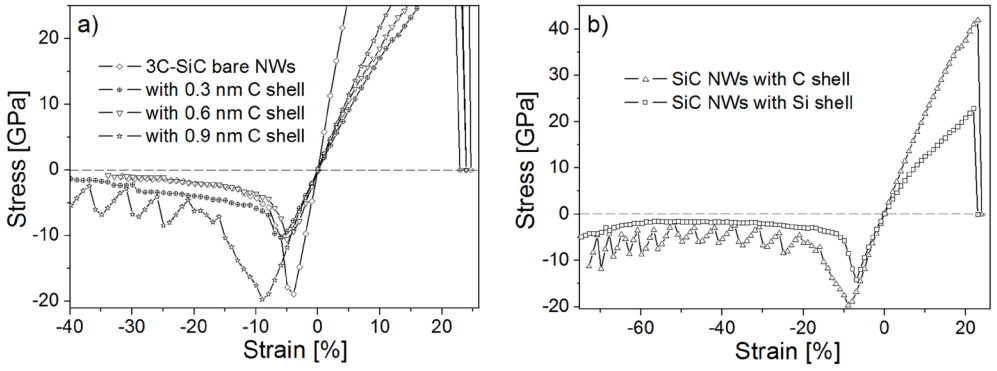

Fig. 2. *Stress vs. strain curves for a) 3C–SiC nanowires with different thicknesses of disorder carbon shell and b) the SiC nanowires coated with different types of disorder shell*

Table 1. *Young's modulus of crystalline–disorder core-shell nanowires with different core diameters and shell thicknesses; the values were obtained using linear regression from the stress–strain curves for strain from –3.0 % to 3.0 %*

	Young's modulus (GPa) of the core/shell NWs									
	SiC core, $D = 1$ nm		SiC core, $D = 1.3$ nm		SiC core, $D = 1.7$ nm		SiC core, $D = 2$ nm		Si core, $D = 4.2$ nm	
Shell size [nm]	*d*-C shell	*d*-Si shell	*d*-C shell	*d*-Si shell	*d*-C shell	*d*-Si shell	Shell size [nm]	*d*-SiC shell	Shell size [nm]	*d*-Si shell
0	561	561	547	547	544	544	0	520	0	131.1
0.3	250	209	269	259	276	248	0.3	440	0.3	113.9
0.6	258	94	272	189	288	218	0.6	435	0.6	103.6
0.9	259	92	273	151	292	173	0.9	430	0.9	82.7

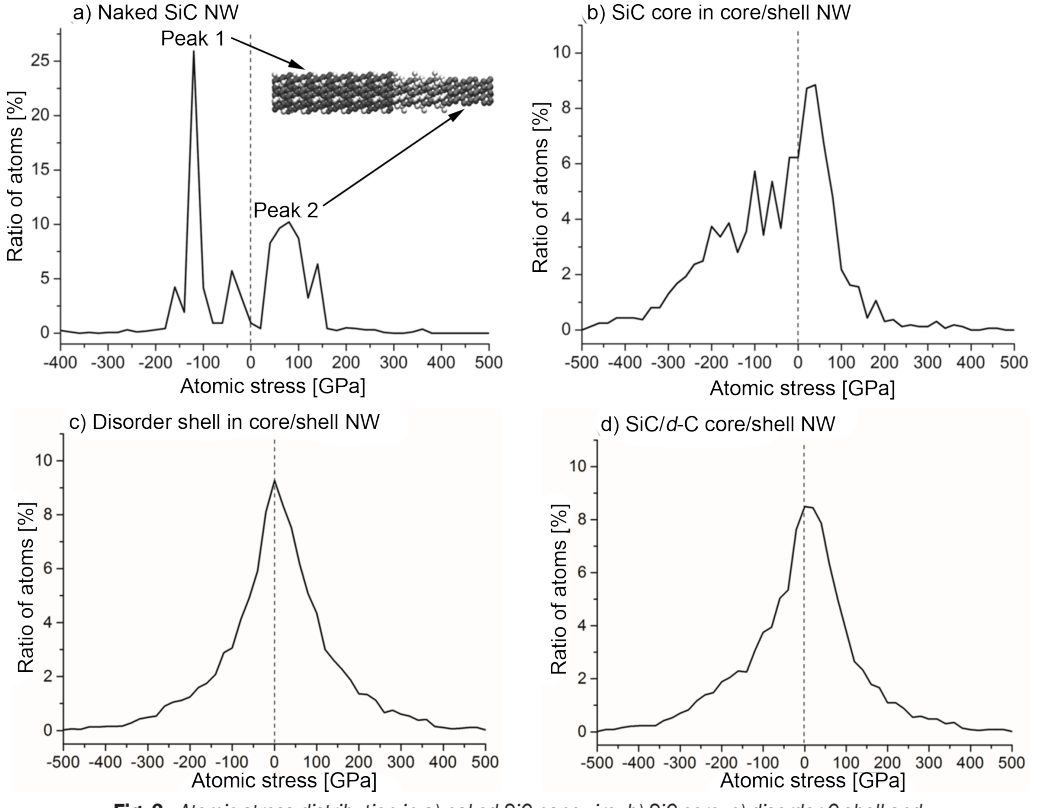

Fig. 3. *Atomic stress distribution in a) naked SiC nanowire, b) SiC core, c) disorder C shell and d) the whole core/shell nanowire; the strain of all nanowires is 0%*

Table 2. *Young's modulus and volume fraction of core-shell nanowires*

	0.9 nm *d*-C shell			0.6 nm *d*-C shell			0.3 nm *d*-C shell		
Core size [nm]	1	1.3	1.7	1	1.3	1.7	1	1.3	1.7
Y [GPa] of core/shell	259	273	292	258	272	288	250	269	276
Y [GPa] of core	426	441	449	415	445	461	446	457	471
$V_{core}/V_{core\text{-}shell}$ [%]	14	19	24	23	27	33	40	44	46
Y [GPa] of shell	231	235	244	211	212	204	168	124	113
$V_{shell}/V_{core\text{-}shell}$ [%]	86	81	76	77	73	67	60	56	54

and the surface dangling bonds result in their high compressive state. To reach the force equilibrium of the whole wire, the atoms in the inner region are under a tension stress state (peak 2 in Fig. 3a). When stretching the naked NWs, the external force has to overcome an additional barrier coming from the surface atoms in a compressive state. Furthermore, the compressive loading will be resisted by the inner atoms under tension. The high fraction of surface atoms in nanowires guarantees above non-uniform stress distribution and then strengthen the whole wire. This is especially true in thinner nanowires, i.e. size effect.

The disorder shell can change the stress distribution of the SiC core, reflecting the fact that most of the atoms in the wire are close to the zero stress state (Fig. 3b). The shell atoms at the interface saturate those dangling bonds in the surface of the SiC core and then the surface stress in the naked state is almost released. In addition, we observed that most of the atoms in the disorder shell are in a zero stress state (Fig. 3c), regardless of the existence of a free surface. This can be understood by the disorder structure, in which atoms can freely choose their coordination atoms to eliminate the surface stress. Therefore, most of the atoms in SiC-disorder core-shell nanowires are in near a zero stress state (Fig. 3d), and then the wires are softer than their naked counterparts.

Another interesting trend in Table 1 is that SiC-*d*-C and SiC-*d*-Si NWs stiffen because of the large crystalline core, for fixed disorder shell thickness. In order to understand this size effect, we rearrange the calculation equation of Young's modulus of the core-shell NWs, as shown below.

According to Eq. (1), the deformation stresses of the core-shell NWs under loading are:

$$\sigma^{zz}_{core-shell} = \frac{1}{V_{core-shell}}\left(\sum_{i=1}^{N_{core}} f_i^z + \sum_{i=N_{core}+1}^{N} f_i^z\right) = \\ = \frac{V_{core}}{V_{core-shell}}\sigma^{zz}_{core} + \frac{V_{shell}}{V_{core-shell}}\sigma^{zz}_{shell}. \quad (3)$$

We then obtained the Young's modulus of the core-shell NWs by integrating Eqs. (2) and (3) **[19]**.

$$Y_{core-shell} = \frac{V_{core}}{V_{core-shell}}Y_{core} + \frac{V_{shell}}{V_{core-shell}}Y_{shell}. \quad (4)$$

From the above formula, we see that the Young's modulus of core-shell NWs is the weighted combination of the Young's modulus of the cores and

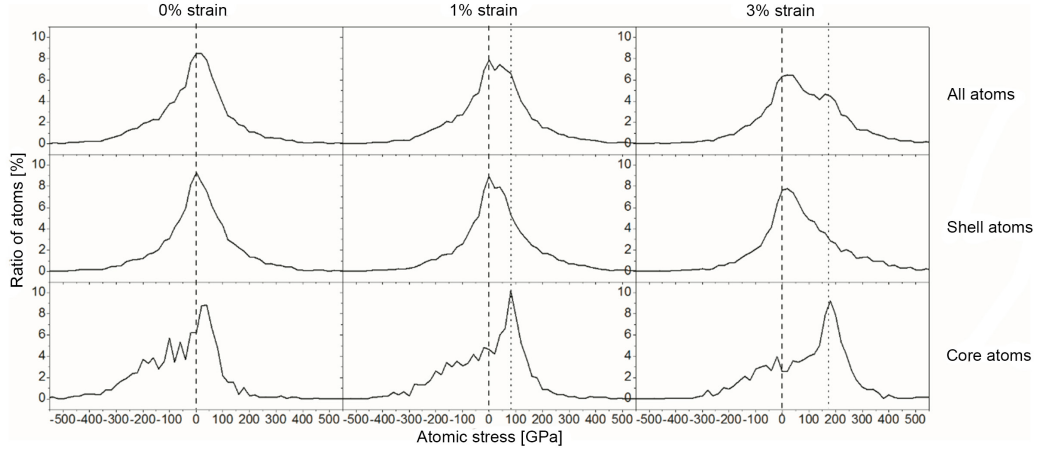

Fig. 4. *Atomic stress distribution in SiC–d-C core-shell nanowires with different strains*

the shells. The weight factor is the fractional volume $V_{core}/V_{core\text{-}shell}$ ($V_{shell}/V_{core\text{-}shell} = 1 - V_{core}/V_{core\text{-}shell}$). These values are represented in Table 2. From this table, we found that both of the modulus values of the core and the shell increases with the rising of the core size. Moreover, the Young's modulus of the core is 2 to 3 times larger than that of the shell. Although the value of $V_{shell}/V_{core\text{-}shell}$ becomes small in the large core, the whole nanowires still stiffen due to the more important role of the core in deciding the strength of the core/shell wires. The role of the core and the shell in the deformation of core-shell NWs is confirmed by the atomic stress distribution of wires under loading (Fig. 4). This figure shows that most of the atoms in core enter a tensile stress state in respond to the external stretching force (peak right shift). Comparatively, the peak of atoms fraction in shell still locates in the zero stress position during loading.

The volumes in Table 2 are nominal values, and we ignored the temperature and core-shell interface space. The latter can cause difficulties in defining the volumes of the isolated cores and shells in core-shell NWs. Liu et al. [19] defined the geometric and physical volumes. The physical volume is due to the existence of the core-shell interface region. The basis for this definition is the division of the interface region into two parts that belong to the core and the shell. Liu et al. [19] also calculated the physical volume according to the ratio of the bond lengths of the core and the shell. In the proposed core-shell model, the ratio of bond lengths was not obtained owing to the disordered structure. Instead, we used the ratio of the average atomic potential energy of the core and the shell to divide the interface region and then calculated the physical volume as well as the Young's modulus of the isolated core and the isolated shell, as shown in Tables 2 and 3.

For fixed crystalline core diameter, the Young's modulus of SiC-*d*-Si, SiC-*d*-SiC, and Si-*d*-Si core/shell NWs decreases as the thickness of the disorder shell increases (Table 1). An opposite trend was observed in SiC-*d*-C core/shell NWs, i.e. the thicker the disorder carbon shell is, the larger the modulus. This difference can be understood by comparing the strength of disorder carbon and disorder silicon. In disorder carbon, we do find some ultra-strong local structures (diamond-like carbon), which results in the relatively high strength in SiC-*d*-C core/shell NWs.

In addition to affecting the strength, the disorder coating can cause plastic deformation in semiconductor materials, as shown in Fig. 5, from which it can be seen that NWs with or without disorder coating buckle under uniaxial compression. Makeev et al. [20] also reported the buckling modes of SiC NWs. Buckling is related to the smaller diameter for a given length of nanowires regardless of the core-shell structure. No structural defects appeared in naked SiC wires below the critical strain (31 %) with additional compression. Upon exceeding the critical strain, the abrupt rupture of the Si-C bond outside the buckling region and the subsequent clean cut indicates brittle behaviour. In contrast, for core-shell NWs, no clean rupture was observed in the isolated core and shell during deformation, as indicated by the plastic deformation of SiC NWs owing to the disorder layer. Comparing the configuration of the naked wire and the isolated core in Fig. 5, we see that the structure of the latter is more disordered. We believe that the amorphization of the core induced by the disorder shell is the main contributor to the ductile properties of core-shell NWs.

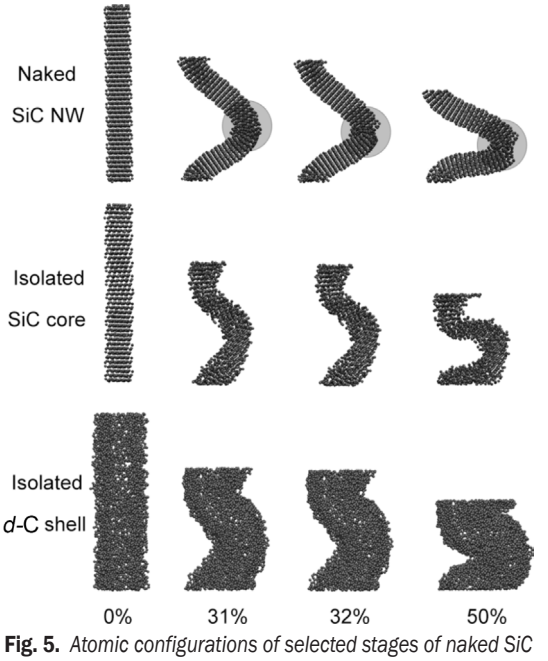

Fig. 5. *Atomic configurations of selected stages of naked SiC nanowires with 1.3 nm diameter, isolated SiC core with 1.3 nm diameter, and a disorder layer with 0.6 nm thickness*

3 CONCLUSION

We used molecular dynamics to simulate the mechanical deformation of SiC-*d*-C and SiC-*d*-Si core-shell nanowires and studied the Young's modulus and plastic deformation due to the disorder shell. We found that the strength of SiC nanowires decreased after the application of disorder coating, as can be attributed to the release of the interface atomic stress by the disorder shell. Furthermore, the size effect was

observed, i.e. the bigger the SiC core, the larger the Young's modulus of the core-shell nanowires. The interface effect was considered to divide the core-shell interface into two parts belonging to the core and the shell, and the modulus of the crystal core dominates the strength of the whole wire. Additional deformation beyond the elastic region suggests that the disorder shell induces the amorphization of the crystal core and makes the semiconductor core-shell nanowires ductile. The simulation showed that the mechanical properties of the semiconductor core-shell nanowires depend on the type and thickness of the disorder shell, which will facilitate their application to nanoscale devices.

4 ACKNOWLEDGEMENTS

This work was supported by the Natural Science Foundation of China under grant 21503165 and 51372197, the Key Innovation Team of Shaanxi Province (2014KCT-04), the Major International Joint Research Program of Shaanxi Province (2012KW-10), and the Science and Technology Program of Shaanxi Province (2013KJXX-42).

5 REFERENCES

[1] Zheng, B., Wang, Y.N., Qi, M., Williams, E.H. (2009). Phase boundary effects on the mechanical deformation of core/shell Cu/Ag nanoparticles. *Journal of Materials Research*, vol. 24, no. 7, p. 2210-2214, **DOI:10.1557/jmr.2009.0263**.

[2] Chen, H., Xu, J., Chen, P.C., Fang, X., Qiu, J., Fu, Y., Zhou, C. (2011). Bulk synthesis of crystalline and crystalline core/amorphous shell silicon nanowires and their application for energy storage. *ACS Nano*, vol. 5, no. 10, p. 8383-8390, **DOI:10.1021/nn203166w**.

[3] Li, Z.Q., Li, X.D., Liu, Q.Q., Chen, X.H., Sun, Z., Liu, C., Ye, X.J., Huang, S.M. (2012). Core/shell structured NaYF4:Yb3+/Er3+/Gd+3 nanorods with Au nanoparticles or shells for flexible amorphous silicon solar cells. *Nanotechnology*, vol. 23, no. 2, paper 025402, **DOI:10.1088/0957-4484/23/2/025402**.

[4] Khachadorian, S., Papagelis, K., Ogata, K., Hofmann, S., Phillips, M.R., Thomsen, C. (2013). Elastic properties of crystalline-amorphous core-shell silicon nanowires. *The Journal of Physical Chemistry C*, vol. 117, no. 8, p. 4219-4226, **DOI:10.1021/jp309842c**.

[5] Sandmann, B., Happ, B., Perevyazko, I., Rudolph, T., Schacher, F.H., Hoeppener, S., Mansfeld, U., Hager, M.D., Fischer, U.K., Burtscher, P., Moszner, N., Schubert, U.S. (2015). Incorporation of core-shell particles into methacrylate based composites for improvement of the mechanical properties. *Polymer Chemistry*, vol. 6, no. 29, p. 5273-5280, **DOI:10.1039/C4PY01544D**.

[6] Fang, Q.H., Liu, Y.W., Jin, B., Wen, P.H. (2009). Interaction between a dislocation and a core-shell nanowire with interface effects. *International Journal of Solids and Structures*, vol. 46, no. 6, p. 1539-1546, **DOI:10.1016/j.ijsolstr.2008.11.026**.

[7] Yang, Z.X., Jun, Y.J., Zhu, F., Zhang, Y. (2005). Helical nanocables with SiC core and SiO_2 shell. *Physica E*, vol. 25, no. 4, p. 395-398, **DOI:10.1016/j.physe.2004.07.006**.

[8] Zhang, H.F., Wang, C.M., Wang L.S. (2002). Helical crystalline SiC/SiO_2 core-shell nanowires. *Nano Letter*, vol. 2, no. 9, p. 941-944, **DOI:10.1021/nl025667t**.

[9] Dai, L., Sow, C.H., Lim, C.T., Cheong, W.C.D., Tan V.B.C. (2009). Numerical investigations into the tensile behavior of TiO2 nanowires: Structural deformation, mechanical properties, and size effects. *Nano Letter*, vol. 9, no. 2, p. 576-582, **DOI:10.1021/nl8027284**.

[10] Shen, G., Chen, D., Tang, K., Qian, Y., Zhang, S. (2003). Silicon carbide hollow nanospheres, nanowires and coaxial Nanowires. *Chemical Physics Letters*, vol. 375, no. 1-2, p. 177-184, **DOI:10.1016/S0009-2614(03)00877-7**.

[11] Yang, G.Z., Cui, H., Sun, Y., Gong, L., Chen, J., Jiang, D., Wang, C.X. (2009). Simple catalyst-free method to the synthesis of β-SiC nanowires and their field emission properties. *The Journal of Physical Chemistry C*, vol. 113, no. 36, p. 15969-15973, **DOI:10.1021/jp906167s**.

[12] Lu, Q., Marks, N., Schatz, G.C., Belytschko, T. (2008). Nanoscale fracture of tetrahedral amorphous carbon by molecular dynamics: Flaw size insensitivity. *Physical Review B*, vol. 77, no. 1, p. 014109, **DOI: 10.1103/PhysRevB.77.014109**.

[13] Mathioudakis, C., Kopidakis, G., Kelires, P. C., Wang, C.Z., Ho, K.M. (2004). Physical trends in amorphous carbon: A tight-binding molecular-dynamics study. *Physical Review B*, vol. 70, no. 12, p. 125202, **DOI:10.1103/PhysRevB.70.125202**.

[14] Plimpton, S. (1995). Fast parallel algorithms for short-range molecular-dynamics. *Journal of Computational Physics*, vol. 117, no. 1, p. 1-19, **DOI:10.1006/jcph.1995.1039**.

[15] Hoover, W.G. (1985). Canonical dynamics: Equilibrium phase-space distributions. *Physical Review A*, vol. 31, no. 3, p. 1695-1697, **DOI:10.1103/PhysRevA.31.1695**.

[16] Nosé, S. (1984). A unified formulation of the constant temperature molecular-dynamics methods. *The Journal of Chemical Physics*, vol. 81, no. 1, p. 511-519, **DOI:10.1063/1.447334**.

[17] Erhart, P., Albe, K. (2005). Analytical potential for atomistic simulations of silicon, carbon, and silicon carbide. *Physical Review B*, vol. 71, no. 3, p. 035211, **DOI:10.1103/PhysRevB.71.035211**.

[18] Jing, Y., Meng, Q. (2010). Molecular dynamics simulations of the mechanical properties of crystalline/amorphous silicon core/shell nanowires. *Physica B*, vol. 405, no. 10, p. 2413-2417, **DOI:10.1016/j.physb.2010.02.056**.

[19] Liu, X.W., Hu, J., Pan, B.C. (2008). The composition-dependent mechanical properties of Ge/Si core-shell nanowires, Physica E, vol. 40, no. 10, p. 3042-3048, **DOI:10.1016/j.physe.2008.03.011**.

[20] Makeev, M.A., Srivastava, D., Menon, M. (2006). Silicon carbide nanowires under external loads: An atomistic simulation study. *Physical Review B*, vol. 74, no. 16, p. 165303, **DOI:10.1103/PhysRevB.74.165303**.

Strojniški vestnik - Journal of Mechanical Engineering 61(2015)11, 669-679

DOI:10.5545/sv-jme.2015.2818 Original Scientific Paper
Received for review: 2015-06-30
Received revised form: 2015-09-15
Accepted for publication: 2015-09-17

Numerical Study of the Effect of the Reynolds Numbers on Thermal and Hydrodynamic Parameters of Turbulent Flow Mixed Convection Heat Transfer in an Inclined Tube

Farhad Vahidinia* – Mohadeseh Miri
University of Zabol, Department of Mechanical Engineering, Iran

A numerical investigation of the effect of the Reynolds number on the thermal and hydrodynamic parameters of mixed convection heat transfer of the water-Al_2O_3 nanofluid turbulent flow in an inclined circular channel is the subject of this article. The upper wall of the channel was under non-uniform heat flux and its lower part was isolated. The two-phase mixture model, the finite volume method, and the second-order upstream difference scheme were used to solve the governing equations. After reviewing the results, it was found that by increasing Reynolds number, the convective heat transfer coefficient and shear stress increase, but the surface friction coefficient decreases. In the case of Nusselt number and the surface friction coefficient, some equations were extracted.

Keywords: mixed convection, inclined channel, turbulent flow, Reynolds number, surface friction coefficient

Highlights

- *New correlations are proposed to calculate the Nusselt number and surface friction coefficient in an inclined tube which is a function of the Reynolds number and the angle of the tube from the horizon surface.*
- *The convective heat transfer coefficient increases with the increase of Reynolds number in an inclined tube.*
- *In an inclined tube, the surface friction coefficient of the length tube decreases when the Reynolds number is increased.*
- *By increasing volume fraction of the nanoparticles in an inclined tube, the convection heat transfer coefficient is increased.*

0 INTRODUCTION

Convective heat transfer in inclined tubes has long been considered. One of the most important applications of the inclined tube is their use in solar collectors and refrigerant distillation in condensers of heat transfer systems [1] to [3], since introducing the subject of adding nanoparticles to the base fluid to improve the efficiency of heat transfer systems, extensive studies were done both numerically and experimentally in horizontal tubes with different boundary conditions and various cross sections [4] to [6]. Saha and Paul [7] studied numerically turbulent flow forced convection heat transfer of two nanofluids and concluded that by increasing the Reynolds number, the Nusselt number increases. Azmi et al. [8] investigated experimental convection heat transfer of nanofluids turbulent flow under constant heat flux of the wall in a circular tube and indicated that the convection heat transfer coefficient increases with increasing the Reynolds Numbers in different volume fractions. Forced convective heat transfer of the water/Al_2O_3 nanofluids turbulent flow was numerically investigated in a horizontal circular tube by Hejazian et al. [9]. They concluded that convective heat transfer coefficient increases with an increased Reynolds Numbers and volume fraction. Furthermore, these studies were widely investigated using nanofluids in the vertical tubes. [10] to [12]. He et al. [13] examined experimental heat transfer and flow behaviour in a vertical tube and concluded that by increasing the Reynolds Numbers, convective heat transfer coefficient and the flow pressure drop increase. Saberi et al. [14] investigated the numerically forced convective heat transfer of laminar flow with nanofluids under wall uniform heat flux in a vertical circular tube. They found that the convective heat transfer coefficient and the Nusselt number increase with increased Reynolds Numbers.

The inclined tubes also were selected for the studies [15] and [16]. Solar collectors are the most important devices which use of the inclined tubes to investigate heat transfer by using nanofluids is studied in them [17]. Numerical study of the mixed convective heat transfer water/Al_2O_3 nanofluids laminar flow is conducted in the horizontal and inclined tubes by Akbari et al. [18]. They indicated that by increasing the inclination of the tube, surface friction coefficient continuously increases, but convective heat transfer coefficient has maximum value at an angle of 45°. Cimpean and Pop [19] investigated mixed convective heat transfer of laminar flow in an inclined channel and concluded that use of nanofluids increases heat transfer. Allahyari et al. [20] studied numerically mixed convective heat transfer of water/Al_2O_3 nanofluids laminar flow with the wall non-uniform heat flux in an inclined circular tube; they concluded

*Corr. Author's Address: University of Zabol, Department of Mechanical Engineering, Zabol, Iran, f.vahidinia@gmail.com

that convective heat transfer coefficient increases with enhancing nanoparticles volume fraction, but it decreases with increasing the tube angle from the horizontal surface. Mansour et al. [21] examined experimentally mixed convective heat transfer of water/Al_2O_3 nanofluids laminar flow in an inclined tube. They observed that by increasing nanoparticles volume fraction and the Reynolds number, the Nusselt number decreases. On the other hand, the Nusselt number increases with increasing the Grashhof number. Investigating pressure drop of nanofluids laminar flow under the wall uniform heat flux studied experimentally in an inclined tube by Pirhayati et al. [22]. They made a conclusion that pressure drop increases with increasing volume fraction of nanoparticles, but increasing the inclination of the tube from the horizon from 0 degrees to 30 degrees for Reynolds number less than 170, reduces the pressure drop. Derakhshan and Akhavan-Behabadi [23] used fin and flat inclined tubes to evaluate the flow characteristic, pressure drop, and friction coefficient by using MWCNT– oil nanofluid. They observed that by increasing the inclination of the tube from 0 degrees to 90 degrees, the pressure drop and friction coefficient increase. Also, pressure drop in the fin tubes is more than the flat tubes. Maré, et al. [24] also analyzed experimentally mixed convective heat transfer of laminar flow in a circular inclined tube.

In this paper, the effect of Reynolds number on thermal and hydrodynamic parameters including convective heat transfer coefficient, Nusselt number, surface friction coefficient is investigated numerically in mixed convective heat transfer Al_2O_3/water nanofluids turbulent flow within an inclined copper tube under non-uniform heat flux of the upper wall and insulation of the lower wall by using two phase mixture model. According to the obtained numerical results, some equations are extracted to calculate the average Nusselt number and the wall surface friction coefficient in terms of Reynolds number changes and different inclinations of tube.

1 MATHEMATICAL MODELING

Turbulent mixed convection of a nanofluid consisting of water and Al_2O_3 in a horizontal circular tube with non-uniform heat flux on the upper wall and insulation in the lower wall has been considered. In order to discretize of governing equations the upstream difference scheme of second-order and finite volume method are used. Fig. 1 shows the considered geometrical configuration. The tube has a diameter of 0.01 m and a length of 1 m. Tube thickness to diameter ratio of 0.1 is assumed. In this paper, the two phase mixture model is employed for the simulation. The nanofluid is a mixture of water and particles of Al_2O_3 and the size is uniform 32 nm.

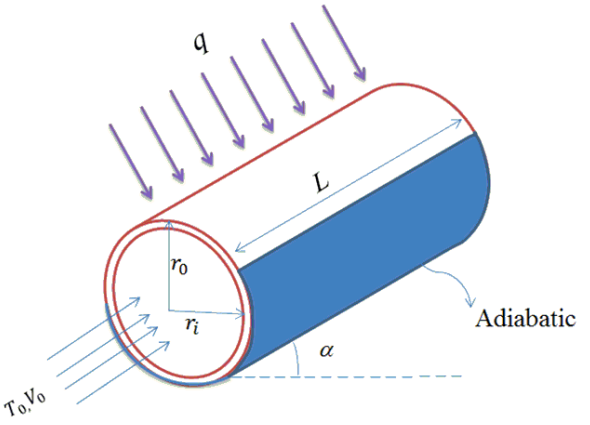

Fig. 1. *Studied geometry (schematic of an inclined tube)*

The conservation equations for steady state mixture model with assumption incompressible and Newtonian of flow are as follows [25]:
Continuity equation:

$$\nabla \cdot (\rho_m \mathbf{V}_m) = 0. \tag{1}$$

Conservation of momentum:

$$\nabla.\left(\rho_m \mathbf{V}_m \mathbf{V}_m\right) = -\nabla p_m + \nabla.\left[\tau - \tau_t\right] - \\ -\rho_{eff}\beta_{eff}(T - T_0)g + \\ +\nabla.\left(\sum_{k=1}^{n} \phi_k \rho_k \mathbf{V}_{dr,k} \mathbf{V}_{dr,k}\right). \tag{2}$$

Conservation of energy:

$$\nabla \cdot (\phi_k \mathbf{V}_k (\rho_k h_k + p)) = \nabla \cdot (\lambda_{eff} \nabla T - C_p \rho_m \overline{vt}). \tag{3}$$

Conservation of energy:

$$\nabla \cdot \left(\phi_p \rho_p \mathbf{V}_m\right) = -\nabla \cdot \left(\phi_p \rho_p \mathbf{V}_{dr,p}\right), \tag{4}$$

where $\mathbf{V}_m$ and ρ_m are defined as:

$$\mathbf{V}_m = \frac{\sum_{k=1}^{n} \phi_k \rho_k \mathbf{V}_k}{\rho_{eff}}, \quad \rho_m = \sum_{k=1}^{n} \phi_k \rho_k, \tag{5}$$

In Eq. (2), $\mathbf{V}_{dr,k}$ is the drift velocity for the secondary phase k, i.e. the nanoparticles in the present study which is defined as:

$$\mathbf{V}_{dr,k} = \mathbf{V}_k - \mathbf{V}_m, \tag{6}$$

and in Eq. (2), τ and τ_t are the viscous shear stress and turbulent shear stress which are defined as:

$$\tau = \mu_m \nabla \mathbf{V}_m, \quad \tau_t = -\sum_{k=1}^{n} \phi_k \rho_k \overline{v_k v_k}, \tag{7}$$

where μ_m is defined as:

$$\mu_m = \sum_{k=1}^{n} \phi_k \mu_k. \tag{8}$$

$\mathbf{V}_{pf}$ is the slip velocity or relative velocity that defines as the velocity of a secondary phase (p) relative to the velocity of the primary phase (f).

$$\mathbf{V}_{pf} = \mathbf{V}_p - \mathbf{V}_f. \tag{9}$$

The drift velocity is related to the relative velocity which is defined as:

$$\mathbf{V}_{dr,k} = \mathbf{V}_{pf} - \sum\nolimits_{k=1}^{n} \frac{\phi_k \rho_k}{\rho_m} \mathbf{V}_{fk}. \tag{10}$$

The relative velocity is determined from Eq. (9) proposed by Manninen et al. **[26]**:

$$\mathbf{V}_{pf} = \frac{\rho_p d_p^2}{18 \mu_f f_{drag}} \frac{\left(\rho_p - \rho_m\right)}{\rho_p} \mathbf{a}. \tag{11}$$

In this equation the drag function, f_{drag} is calculated by Schiller and Naumann **[27]**:

$$f_{drag} = \begin{cases} 1 + 0.15 Re_p^{0.687}, & Re_p \le 1000 \\ 0.0183 Re_p, & Re_p \ge 1000 \end{cases}. \tag{12}$$

The acceleration (**a**) in Eq. (11) is:

$$\mathbf{a} = \mathbf{g} - (\mathbf{V}_m \cdot \nabla)\mathbf{V}_m. \tag{13}$$

2 TURBULENCE MODELING

Turbulence is modeled with the Launder and Spalding **[28]** k–ε turbulence model for the mixture. It is expressed by Eqs. (14) to (16):

$$\nabla \cdot (\rho_m \mathbf{V}_m k) = \nabla \cdot (\frac{\mu_{t,m}}{\sigma_k} \nabla k) + G_{k,m} - \rho_m \varepsilon, \tag{14}$$

$$\nabla \cdot (\rho_m \mathbf{V}_m \varepsilon) = \nabla \cdot (\frac{\mu_{t,m}}{\sigma_\varepsilon} \nabla k) + \frac{\varepsilon}{k} (c_1 G_{k,m} - c_2 \rho_m \varepsilon), \tag{15}$$

where:

$$\mu_{t,m} = \rho_m c_\mu \frac{k^2}{\varepsilon}, \quad G_{k,m} = \mu_{t,m} (\nabla V_m + (\nabla V_m)^T),$$
$$c_1 = 1.44, c_2 = 1.92, c_\mu = .09, \sigma_k = 1, \sigma_\varepsilon = 1.3, \tag{16}$$

where c_1 and c_2 are constants.

3 BOUNDARY CONDITION

The boundary conditions are expressed as follows:

- At inlet of tube ($Z = 0$):

$$V_z = V_0, \quad V_\theta = V_r = 0, \quad T = T_0, \quad I = I_0. \tag{17}$$

Turbulent intensity calculated based on the formula **[29]**:

$$I_0 = 0.16 \left(Re\right)^{\frac{-1}{8}}. \tag{18}$$

- At the tube wall ($r = r_0$):

$$0 \le \theta \le \pi: \quad -\lambda_s \frac{\partial T_s}{\partial r} = q_w, \tag{19}$$

$$\pi \le \theta \le 2\pi: \quad -\lambda_s \frac{\partial T_s}{\partial r} = 0. \tag{20}$$

- At the solid/fluid interface: ($r = r_i$):

$$T_w = T_{nf}, \quad \lambda_s \frac{\partial T_w}{\partial r} = \lambda_{eff} \frac{\partial T_{nf}}{\partial r}, \quad V_z = V_r = V_\theta = 0. \tag{21}$$

- At the tube outlet:
  The diffusion fluxes are set to zero at the exit for all dependent variables and an overall mass balance correction is obeyed.

4 NANOFLUID THERMO-PHISICAL PROPERTIES

The physical properties are:

Effective density:

The nanofluid density is given by **[30]**:

$$\rho_m = \left(1 - \phi\right)\rho_f + \phi \rho_p, \tag{22}$$

where the volumetric concentration is given by:

$$\phi = \frac{\rho_f \phi_m}{\rho_f \phi_m + \rho_p \left(1 - \phi_m\right)}, \tag{23}$$

and where ϕ_m is the mass fraction.

An accurate equation is used for calculating the effective heat capacitance:

$$\left(C_p\right)_{eff} = \left[\left(1 - \phi\right)\left(\rho C_p\right)_f + \phi\left(\rho C_p\right)_p\right] \Big/ \rho_m. \tag{24}$$

The thermal conductivity of the nanofluid is calculated from Chon et al. **[31]** correlation, which considers the Brownian motion and mean diameter of the nanoparticles.

$$\lambda_{eff} \Big/ \lambda_f = 1 + 64.7 \times \phi^{0.746} \times \left(d_f / d_p\right)^{0.369} \times$$
$$\times \left(\lambda_p / \lambda_f\right)^{0.746} \times Pr^{0.9955} \times Re^{1.2321}, \tag{25}$$

$$\lambda_{eff}/\lambda_f = 1+64.7\times\phi^{0.746}\times\left(d_f/d_p\right)^{0.369}\times \times\left(\lambda_p/\lambda_f\right)^{0.746}\times Pr^{0.9955}\times Re^{1.2321}, \quad (25)$$

where Pr and Re in Eq. (25) are defined as:

$$Pr=\frac{\mu_f}{\rho_f\alpha_f}, \quad Re=\frac{\rho_f B_c T}{3\pi\mu^2 l_{bf}}, \quad \mu=A\times 10^{\frac{B}{T-C}},$$
$$C=140, \qquad B=247, \qquad A=2.414\mathrm{e}^{-5}. \quad (26)$$

l_{bf} is the mean free path of water and B_c is Boltzman constant (B_c = 1.3807×10–23 J/K).

Effective viscosity is calculated by the following equation proposed by Masoumi et al. [32] that considers the effects of volume fraction, density, and average diameter of nanoparticles and physical properties of the base fluid:

$$\mu_{eff}=\mu f+\frac{\rho_P V_B d_p^2}{72C\delta},$$
$$V_B=\frac{1}{d_p}\sqrt{\frac{18K_bT}{\pi\rho_p d_p}}, \quad \delta=\sqrt[3]{\frac{\pi}{6\phi}}d_p, \quad (27)$$

$$C=\mu_f^{-1}\left[\left(c_1 d_p+c_2\right)\phi+\left(c_3 d_p+c_4\right)\right], \quad (28)$$

where c_1, c_2, c_3 and c_4 are:

$$c_1=-0.000001133, \quad c_2=-0.000002721,$$
$$c_3=-0.00000009, \quad c_4=-0.000000393.$$

Thermal expansion coefficient proposed by Khanafer et al. [33]:

$$\beta_{eff}=\beta_p/\left(1+\left(1-\phi\right)\rho_f/\phi\rho_p\right)\beta_f + +1/\left(1+\phi\rho_p/\left(1-\phi\right)\rho_f\right). \quad (29)$$

5 NUMERICAL METHOD AND VALIDATION

In this work, the fluid enters the tube with a constant inlet temperature T_0 of 293 K and with uniform axial velocity of V_0. The Reynolds number for simulation and selection grid of 5000 is assumed. This set of coupled nonlinear differential equations is discretized with the control volume technique. For the convective and diffusive terms the second order upwind method is used while the SIMPLEC procedure is introduced for the velocity–pressure coupling. A structured non-uniform grid distribution has been used to discretize the computation domain. It is finer near the tube inlet and near the wall where the velocity and temperature gradients are large. Several different grid distributions have been tested to ensure that the calculated results are grid independent.

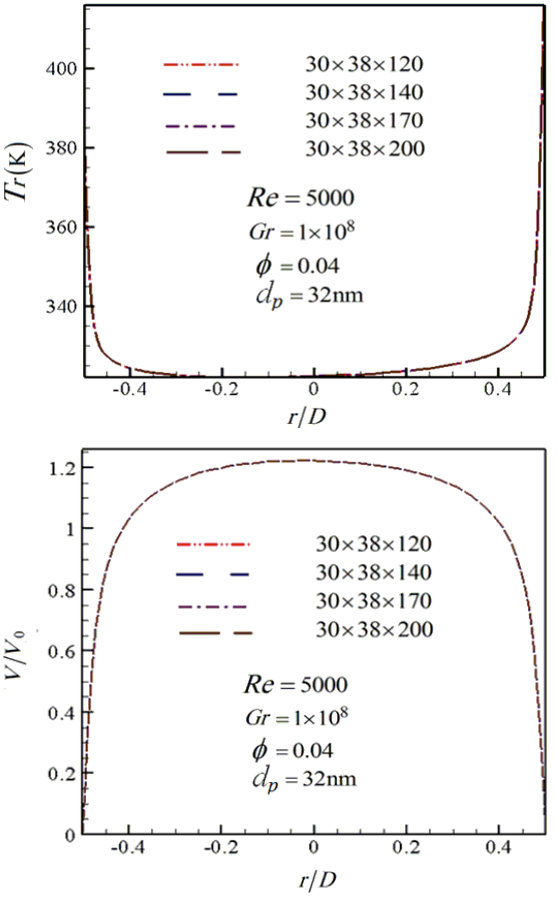

Fig. 2. *Grid independence test: a) fully developed temperature, b) centerline axial velocity*

The selected grid for the present calculations consisted of 170, 30 and 38 nodes, respectively, in the axial, radial and circumferential directions.

As shown in Fig. 2 increasing the grid numbers do not significantly change the velocity and temperature of the nanofluid. Other axial and radial profiles have also been verified to be sure the results are grid independent.

In order to demonstrate the validity and also precision of the model and numerical procedure, comparisons with the available experimental and numerical simulation have been done. As it is shown in Fig. 3, good agreements between the results are observed.

Fig. 3a shows the comparison of the calculated results with the results obtained by Gnielinski and

Sruher [34] and experimental results obtained by Wusiman et al. [35].

Another comparison has also been performed with the experimental results obtained by Torii [36]. (See Fig. 3b).

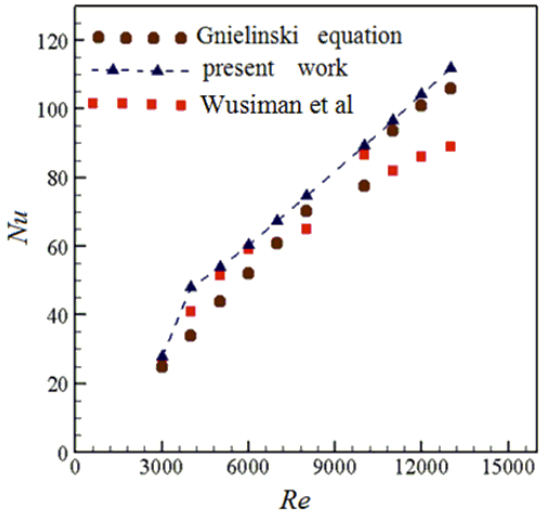

a)

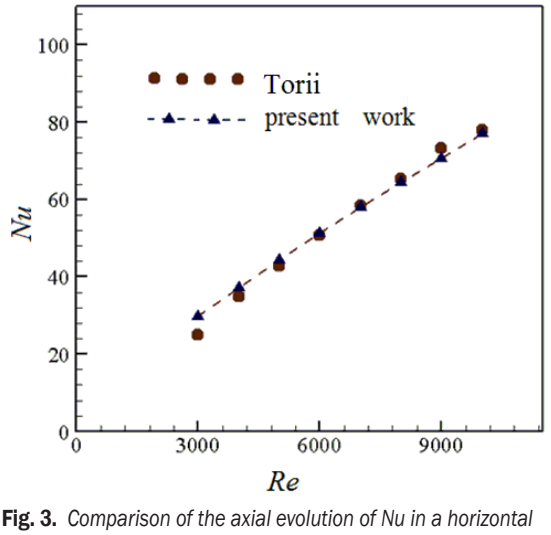

b)

Fig. 3. *Comparison of the axial evolution of Nu in a horizontal tube with the results obtained by a) Gnielinski and Sruher [34] and Wusiman et al. [35]; and b) Torii [36]*

6 RESULTS

One important factor in the study of mixed convective heat transfer of the turbulent flow is to investigate the Reynolds number changes and its effect on thermal and hydrodynamic parameters. The Reynolds number, the volume fraction of nanoparticles and Grashof number are considered 4000 to 6000, 4 %, $Gr = 1\times10^8$ respectively. In this study, the inclination of the tube from horizon is considered 45 degrees and flow of Aluminum oxide/water nanofluids is investigated. Considering that the Reynolds number is the ratio of inertial forces to viscosity forces, with constant volume fraction of the nanoparticles and thus constant viscosity forces, increase or decrease of the Reynolds number will increase or decrease the inertial forces. On the other hand, the Richardson number was defined as the ratio of the Grashof number to the square of Reynolds number in reference [20] and [38]. According to the reference [37], if the above ratio is ($Gr/Re^2 \ll 1$), there will be forced convection heat transfer and we can neglect the effect of natural convection. If, ($Gr/Re^2 \gg 1$), we will have natural convection heat transfer and can neglect the effect of forced convection. Regarding this subject, the references [20], [25] and [38] deal with the study of mixed convection heat transfer. Reference [38], shows the mixed convection heat transfer of nanofluid in laminar flow at Richardson numbers of (Ri = 0.33, 1.66 and 5) in a horizontal tube and reference [20], studied this matter in an inclined tube. Reference [25], also studied the mixed convection heat transfer of nanofluid of turbulent flow in a curved horizontal tube at similar Richardson numbers. As can be seen in references [20], [25] and [38], we will have mixed convection heat transfer at Richardson number (Ri = 4) that is assumed in the present paper. It means that we will have both the effects of buoyancy forces and inertia forces.

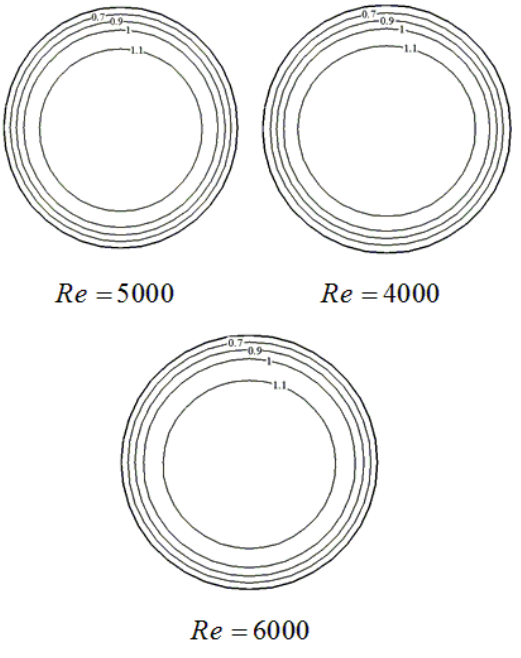

Fig. 4. *Dimensionless axial velocity contours in the radial direction for different Reynolds numbers of Z/D = 94, ϕ = 0.04 and α = 45*

Fig. 4 indicates dimensionless axial velocity contours for Grashof number $Gr = 1\times10^8$ at 4 % volume fraction in different Reynolds numbers and an angle of 45 degrees from horizon.

As figure shows, dimensionless axial velocity contours become longer in the vertical direction with increase of the Reynolds number and it will not have any movement to the up or down of the wall.

Fig. 5 shows dimensionless axial velocity profile in an inclined tube at an angle of 45 degrees from horizon at different Reynolds numbers. As can be seen, in this case velocity profile becomes more uniform with increasing the Reynolds number. Fig. 6 indicates dimensionless axial velocity profile on the tube centerline in an inclined tube at an angle of 45 degrees from horizon at different Reynolds numbers. It is shown in this figure that flow rate is reached to a maximum value after the tube inlet and then is developed. The reason for this is that after the tube inlet, the growth of the tube boundary layer causes contraction and conducts flow towards the tube centerline, thus increases the velocity on the tube centerline. By increasing the Reynolds number, the velocity maximum point inclines down, since by increasing the Reynolds number, the axial momentum and turbulence production in the flow direction increase.

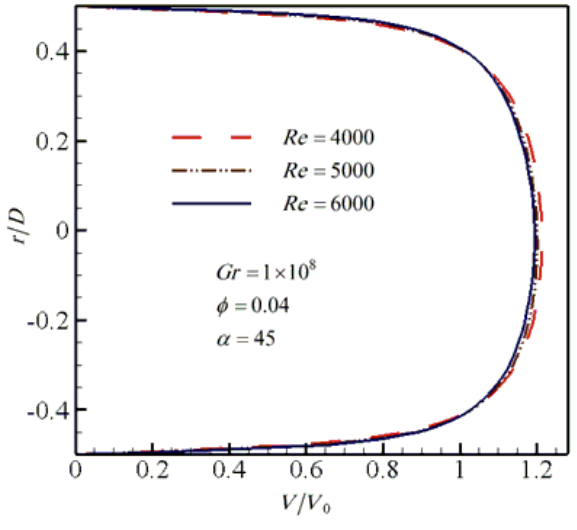

Fig. 5. *Dimensionless axial velocity profile in the radial direction for different Reynolds numbers of Z/D = 94*

The dimensionless axial velocity maximum and the amount of development reduce with increase of Reynolds number and the most important reason for this process is that the velocity profile become more uniform with the increase of Reynolds number.

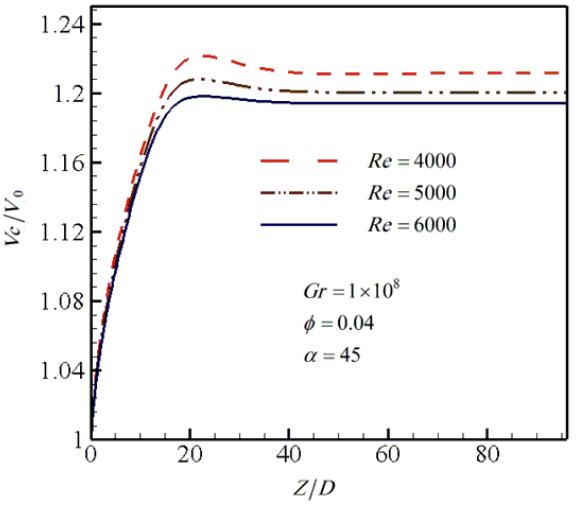

Fig. 6. Dimensionless axial velocity profile in the tube centerline for different Reynolds numbers

Fig. 7 displays dimensionless temperature contours on $Z/D = 94$ of an inclined tube with an angle of 45 degrees from horizon, constant Grashof number $Gr = 1\times10^8$, and 4 % volume fraction at different Reynolds numbers. As can be seen in the figure, dimensionless temperature decreases with the increase of the Reynolds number. At the end of the tube at high Reynolds, fluid has enough time to get the heat. So the temperature contours are asymmetric.

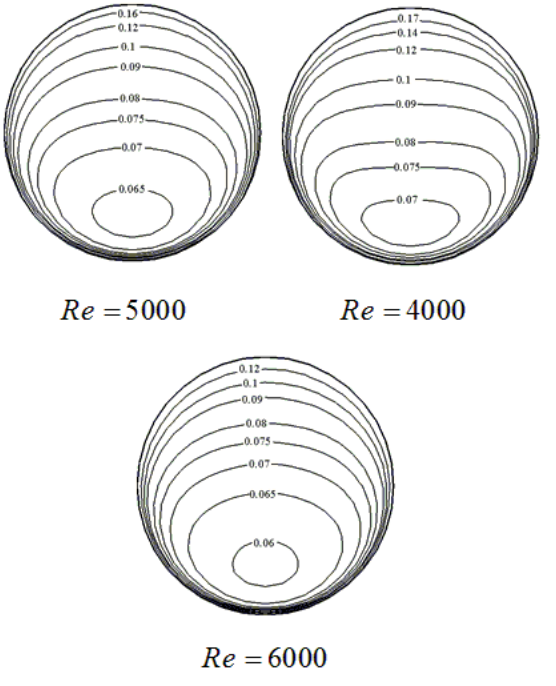

Fig. 7. Dimensionless temperature contours for different Reynolds numbers of Z/D = 94, ϕ = 0.04, Gr = 1×10^8 and α = 45

Fig. 8 shows the turbulent kinetic energy profile on Z/D = 94 of an inclined tube with an angle of 45 degrees from horizon at Grashof number $Gr = 1\times10^8$, and different Reynolds numbers. In this figure, the turbulent kinetic energy increases with increase of the Reynolds number and its main reason will be increase of velocity and turbulences. Fig. 9 indicates changes of convective heat transfer coefficient in the tube dimensionless length within an inclined tube at different Reynolds numbers. At the beginning of the tube after the inlet, the convective heat transfer coefficient is very high due to the proximity of the wall temperature and the fluid bulk temperature. This coefficient reaches to the minimum value with distance from the inlet and there is maximum temperature difference between the wall temperature and the fluid bulk temperature in this area. Then, it remains constant due to the same temperature difference in the developed area. As observed in this figure, convective heat transfer coefficient increases with the increase of Reynolds number and its main reason is the increase of turbulent kinetic energy and turbulences.

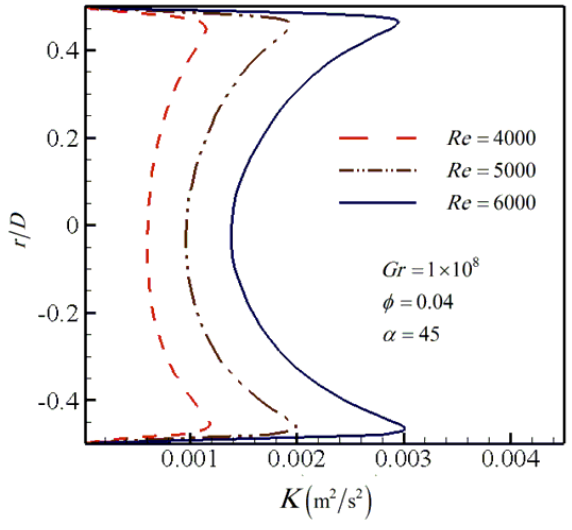

Fig. 8. Turbulent kinetic energy profiles in the radial direction for different Reynolds numbers of Z/D = 94

Fig. 10 displays the shear stress changes in the dimensionless length of an inclined tube with Grashof number $Gr = 1\times10^8$, and solid to liquid volume ratio of 4 % at different Reynolds numbers. By increasing Reynolds number in a constant volume fraction, the flow rate increases resulting in increased velocity gradient. With increase of the velocity gradient and constant viscosity, the shear stress increases. Fig. 11 shows changes of surface friction coefficient in the

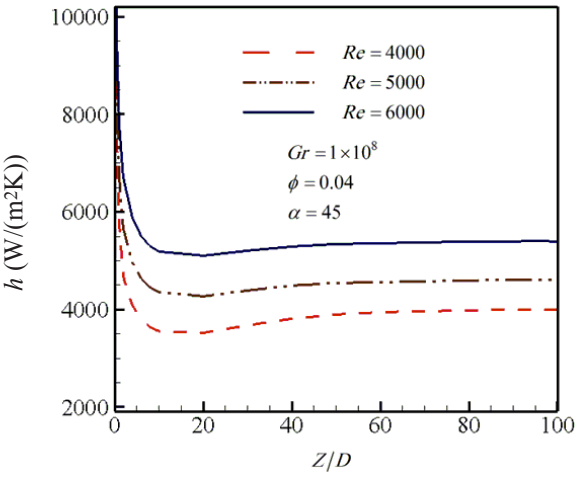

Fig. 9. *Changes of convective heat transfer coefficient for different Reynolds numbers in the tube dimensionless length*

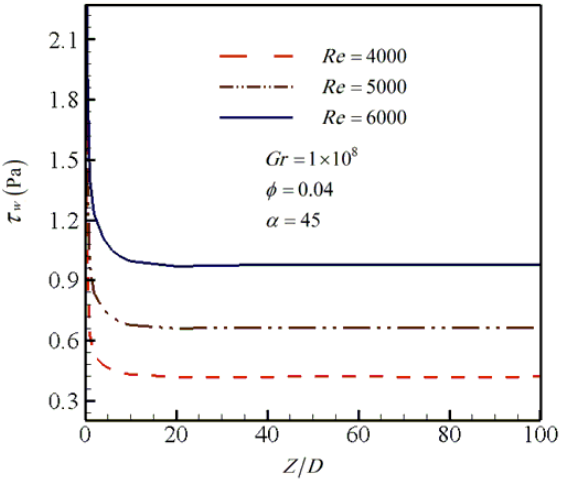

Fig. 10. Changes of shear stress in the dimensionless length of the tube for different Reynolds numbers

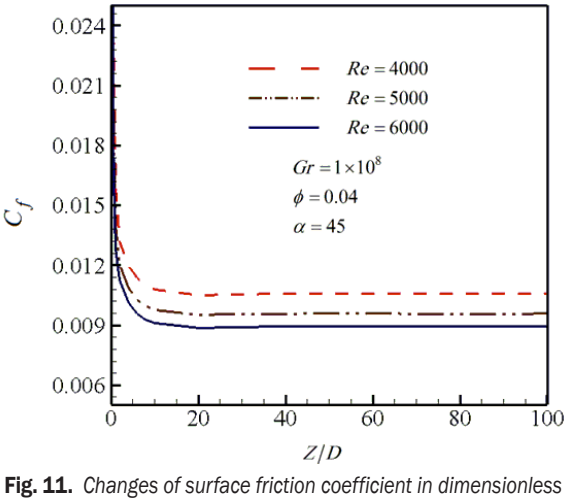

Fig. 11. *Changes of surface friction coefficient in dimensionless length of the tube for different Reynolds numbers*

tube dimensionless length within a horizontal inclined tube with Grashhof number $Gr = 1\times10^8$, and solid to liquid volume ratio of 4 % at different Reynolds numbers. By increasing the Reynolds number, the surface friction coefficient of the tube decreases; this is because of interactions between shear stress and flow rate changes with increase of the Reynolds number.

Fig. 12 shows changes of convection heat transfer coefficient in dimensionless length of the tube at Grashof number $Gr = 1\times10^8$, Reynolds number $Re = 5000$, and with an angle of 45 degrees from horizon in different volume fraction of solid-liquid particles. As can be seen in this figure, by increasing volume fraction of the nanoparticles in an inclined tube, the convection heat transfer coefficient increases; the main reason is the fluid's thermo-physical characteristics improving with increase of nanoparticles volume fraction.

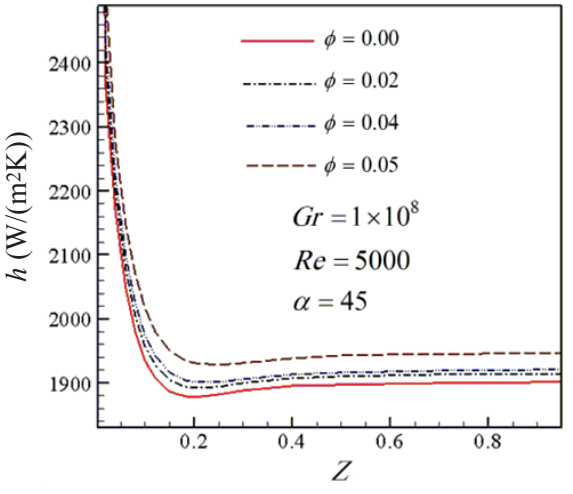

Fig. 12. *Changes of convective heat transfer coefficient in dimensionless length of the tube for different volume fraction*

7 EXTRACTED EQUATIONS FROM THIS STUDY

The behavior of nanofluids heat transfer depends on various parameters such as thermal conductivity, convective heat transfer coefficient, viscosity, heat capacity, angle of the tube from horizon, and volume fraction of nanoparticles. Considering investigation of the hydrodynamic and thermal behavior of nanofluids in an inclined tube, the following equations are obtained to calculate average Nusselt number and surface friction coefficient of the wall.

The following equations are for Nusselt number and surface friction coefficient in an inclined tube which is a function of the Reynolds number and angle of the tube from the horizon surface. In the volume fraction $\phi = 0.04$ for the developed area, it obtains:

$$Nu_{av} = 0.115Re^{0.801}(34.408+\alpha)^{-0.189}, \quad (30)$$

$$C_f = 0.31Re^{-0.391}(0.684+\alpha)^{0.011}. \quad (31)$$

Fig. 13 displays changes of the average Nusselt number in terms of the Reynolds number in different angles within an inclined tube. As observed, the Nusselt number increases with increase of the Reynolds number. On the other hand, by increasing angle of the tube from horizon, the Nusselt number decreases in a certain Reynolds number. By comparing the obtained values from the Eq. (30) and numerical

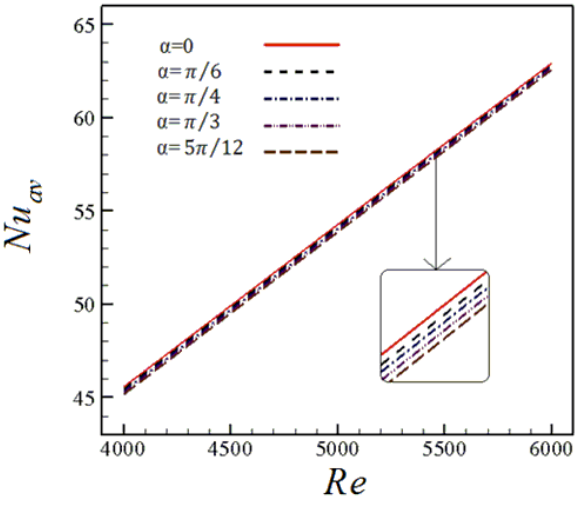

Fig. 13. *Changes of average Nusselt number in terms of Reynolds number for different inclinations of tube*

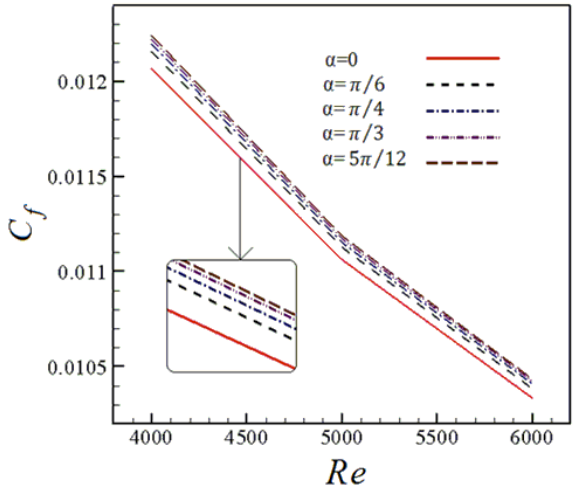

Fig. 14. *Changes of surface friction coefficient in terms of Reynolds number for different inclinations of tube*

data of the thesis, the correlation coefficient is equal to $R^2 = 0.9998$ for the Eq. (30).

Fig. 14 indicates changes of surface friction coefficient in terms of the Reynolds number in different angles within an inclined tube. As can be seen, by increasing the Reynolds number, the surface friction coefficient decreases. On the other hand, by increasing angle of the tube from horizon, the surface friction coefficient increases in a certain Reynolds number. By comparing the obtained values from the Eq. (31) and numerical data of the thesis, the correlation coefficient is equal to $R^2 = 0.9997$ for the Eq. (31).

8 CONCLUSION

In this paper, the effect of Reynolds number on thermal and hydrodynamic characteristics of the nanofluids turbulent flow mixed convective heat transfer within an inclined tube is numerically studied with non-uniform heat flux on the upper wall of the tube and insulation in the lower wall by using two phase mixture model. The results indicated that dimensionless axial velocity becomes more uniform with increase of the Reynolds number in a certain Grashof number and constant volume fraction. By increasing the Reynolds number, the axial momentum increases and turbulence produces in the flow direction. Dimensionless axial velocity maximum and the amount of development decreases with increase of the Reynolds number and the most important reason of this process is that the velocity profile becomes more uniform with increase of the Reynolds number. By increasing the Reynolds number, the turbulent kinetic energy increases and this is because of increase of velocity and thus the turbulences in the fluid. By increasing Reynolds number, the convective heat transfer coefficient and shear stress increase but the surface friction coefficient decreases.

9 NOMENCLATURES

a acceleration [ms^{-2}]
C_f average skin friction coefficient
C_p specific heat of the fluid [Jkg^{-1}K^{-1}]
d_f molecular diameter of base fluid [nm]
d_p nanoparticle diameter [nm]
D tube diameter [m]
g gravity acceleration [ms^{-2}]
Gr Grashof number
h average convective heat transfer coefficient [Wm^{-2}K^{-1}]
K turbulent kinetic energy [m^{2}s^{-2}]
L channel length [m]
n number of phase
p pressure [Pa]
q average wall heat flux [Wm^{-2}]
r radial coordinate [m]
Re Reynolds number
t fluctuating temperature [K]
T temperature [K]
V velocity [ms^{-1}]
Z axial coordinate [m]

Greek letters
α Thermal diffusivity and inclination of tube [Wm^{-2}]
β Volumetric expansion coefficient [K^{-1}]
ε Dissipation of turbulent kinetic energy [m^{2}s^{-1}]
θ Angular coordinate
ϕ particle volume concentration
λ thermal conductivity of the fluid [Wm^{-1}K^{-1}]
μ fluid dynamic viscosity [Kgm^{-1}s^{-1}]
ν kinematic viscosity [m^{2}s^{-1}]
ρ fluid density [Kgm^{-3}]
τ shear stress [Pa]

Subscript
b bulk value
dr drift
eff effective
f primary phase
k k^{th} phase
m mixture
nf nanofluid
p particle, secondary phase
s solid
t turbulent
w wall
0 inlet condition

10 REFERENCES

[1] Mozafari, M., Akhavan-Behabadi, M.A., Qobadi-Arfaee, H., Hanafizadeh, P., Fakoor-Pakdaman, M. (2015). Experimental study on condensation flow patterns inside inclined U-bend tubes. *Experimental Thermal and Fluid Science*, vol. 68, p. 276-287, **DOI:10.1016/j.expthermflusci.2015.05.003**.

[2] Garcia, A., Martin, R.H., Perez-Garcia, J. (2013). Experimental study of heat transfer enhancement in a flat-plate solar water collector with wire-coil inserts. *Applied Thermal Engineering*, vol. 61, no. 2, p. 461-468, **DOI:10.1016/j.applthermaleng.2013.07.048**.

[3] Meyer, J.P., Dirker, J., Adelaja, A.O. (2014). Condensation heat transfer in smooth inclined tubes for R134a at different saturation temperatures. *International Journal of Heat and Mass Transfer*, vol. 70, p. 515-525, **DOI:10.1016/j.ijheatmasstransfer.2013.11.038**.

[4] Sokhansefat, T., Kasaeian, A.B., Kowsary, F. (2014). Heat transfer enhancementin parabolic trough collector tube using Al2O3/synthetic oil nanofluid. *Renewable and Sustainable Energy Reviews*, vol. 33, p. 636-644, **DOI:10.1016/j.rser.2014.02.028**.

[5] Derakhshan, M.M., Akhavan-Behabadi, M.A., Mohseni, S.G. (2015). Experiments on mixed convection heat transfer and performance evaluation of MWCNT–Oil nanofluid flow in horizontal and vertical microfin tubes. *Experimental Thermal and Fluid Science*, vol. 61, p. 241-248, **DOI:10.1016/j.expthermflusci.2014.11.005**.

[6] Moghadassi, A., Ghomi, E., Parvizian, F. (2015). A numerical study of water based Al2O3 and Al2O3-Cu hybrid nanofluid effect on forced convective heat transfer. *International Journal of Thermal Sciences*, vol. 92, p. 50-57, **DOI:10.1016/j.ijthermalsci.2015.01.025**.

[7] Saha, G., Paul, M.C. (2015). Heat transfer and entropy generation of turbulent forced convection flow of nanofluids in a heated pipe. *International Communications in Heat and Mass Transfer*, vol. 61, p. 26-36, **DOI:10.1016/j.icheatmasstransfer.2014.11.007**.

[8] Azmi, W.H., Sharma, K.V., Sarma, P.K., Mamat, R., Najafi, G. (2014). Heat transfer and friction factor of water based TiO2 and SiO2 nanofluids under turbulent flow in a tube. *International Communications in Heat and Mass Transfer*, vol. 59, p. 30-38, **DOI:10.1016/j.icheatmasstransfer.2014.10.007**.

[9] Hejazian, M., Moraveji, M.K., Beheshti, A. (2014). Comparative study of Euler and mixture models for turbulent flow of Al2O3 nanofluid inside a horizontal tube. *International Communications in Heat and Mass Transfer*, **DOI:10.1016/j.icheatmasstransfer.2014.01.022**.

[10] Aminfar, H., Mohammadpourfard, M., Narmani Kahnamouei, Y. (2011). A 3D numerical simulation of mixed convection of a magnetic nanofluid in the presence of non uniform magnetic field in a vertical tube using two phase mixture model. *Journal of Magnetism and Magnetic Materials*, vol. 323, no. 15, p. 1963-1972, **DOI:10.1016/j.jmmm.2011.02.039**.

[11] Behzadmehr, A., Laneville, A., Galanis, N. (2008). Experimental study of onset of laminar–turbulent transition in mixed convection in a vertical heated tube. *International Journal of Heat and Mass Transfer*, vol. 51, no. 25-26, p. 5895–5905, **DOI:10.1016/j.ijheatmasstransfer.2008.04.005**.

[12] Behzadmehr, A., Galanis, N., Nguyen, C.T. (2006). Predicted effects of inlet turbulent intensity on mixed convection in vertical tubes with uniform wall heat flux. *International Journal of Thermal Sciences*, vol. 45, no. 5, p. 433-442, **DOI:10.1016/j.ijthermalsci.2005.08.004**.

[13] He, Y., Jin, Y., Chen, H., Ding, Y., Cang, D., Lu, H. (2007). Heat transfer and flow behaviour of aqueous suspensions of TiO2 nanoparticles (nanofluids) flowing upward through a vertical pipe. *International Journal of Heat and Mass Transfer*, vol. 50, no. 11-12, p. 2272-2281, **DOI:10.1016/j.ijheatmasstransfer.2006.10.024**.

[14] Saberi, M., Kalbasia, M., Alipourzadeh, A. (2013). Numerical Study of Forced Convective Heat Transfer of Nanofluids inside a Vertical Tube. *International Journal of Thermal Technologies*, vol. 3, no. 1, p. 10-15.

[15] Mansour, R.B., Galanis, N., Nguyen, C.T. (2009). Developing laminar mixed convection of nanofluids in an inclined tube with uniform wall heat flux. *International Journal of Numerical Methods for Heat & Fluid Flow*, vol. 19, no. 2, p. 146-164, **DOI:10.1108/09615530910930946**.

[16] Busedra, A.A., Soliman, H.M. (2000). Experimental investigation of laminar mixed convection in an inclined semicircular duct under buoyancy assisted and opposed conditions. *International Journal of Heat and Mass Transfer*, vol. 43, no. 7, p. 1103-1111, **DOI:10.1108/09615530910930946**.

[17] Mahian, O., Kianifar, A., Sahin, A.Z., Wongwises, S. (2014). Entropy generation during Al2O3/water nanofluid flow in a solar collector: Effects of tube roughness, nanoparticle size, and different thermophysical models. *International Journal of Heat and Mass Transfer*, vol. 78, p. 64-75, **DOI:10.1016/j.ijheatmasstransfer.2014.06.051**.

[18] Akbari, M., Behzadmehr, A., Shahraki, F. (2008). Fully developed mixed convection in horizontal and inclined tubes with uniform heat flux using nanofluid. *International Journal of Heat and Fluid Flow*, vol. 29, no. 2, p. 545-556, **DOI:10.1016/j.ijheatfluidflow.2007.11.006**.

[19] Cimpean, D.S., Pop, I. (2012). Fully developed mixed convection flow of a nanofluid through an inclined channel filled with a porous medium. *International Journal of Heat and Mass Transfer*, vol. 55, no. 4, p. 907-914, **DOI:10.1016/j.ijheatmasstransfer.2011.10.018**.

[20] Allahyari, Sh., Behzadmehr, A., Hosseini Sarvari, S.M. (2011). Conjugate heat transfer of laminar mixed convection of a nanofluid through an inclined tube with circumferentially non-uniform heating. *Nanoscale Research Letters*, vol. 6, **DOI:10.1186/1556-276X-6-360**.

[21] Mansour, R.B., Galanis, N., Nguyen, C.T. (2011). Experimental study of mixed convection with water-Al2O3 nanofluid in inclined tube with uniform wall heat flux. *International Journal of Thermal Sciences*, vol. 50, no. 3, p. 403-410, **DOI:10.1016/j.ijthermalsci.2010.03.016**.

[22] Pirhayati, M., Akhavan-Behabadi, M.A., Khayat, M. (2012). Pressure drop of CuO-base oil nanofluid flow inside an inclined tube. *International Journal of Advances in Engineering & Technology*, vol. 5, no. 1, p. 122-129.

[23] Derakhshan, M.M., Akhavan-Behabadi, M.A. (2015). An empirical study on fluid properties and pressure drop of nanofluid flow inside inclined smooth and microfin tubes. *International Communications in Heat and Mass Transfer*, vol. 65, p. 111-116, **DOI:10.1016/j.icheatmasstransfer.2015.04.013**.

[24] Maré, T., Galanis, N., Voicu, I., Miriel, J. (2006). Experimental analysis of mixed convection in inclined tubes. *Applied Thermal Engineering*, vol. 26, no. 14-15, p. 1677–1683, **DOI:10.1016/j.applthermaleng.2005.11.011**.

[25] Ghaffari, O., Behzadmehr, A., Ajam, H. (2010). Turbulent mixed convection of a nanofluid in a horizontal curved tube using a two-phase approach. *International Communications in Heat and Mass Transfer*, vol. 37, no. 10, p. 1551-1558, **DOI:10.1016/j.icheatmasstransfer.2010.09.003**.

[26] Maninnen, M., Taivassalo, V., Kallio, S., (1996). *On the Mixture Model for Multiphase Flow*. VTT Energy, Espoo.

[27] Schiller, L., Naumann, A. (1935). *A Drag Coefficient Correlation*, Z. Ver. Deutsch. Ing, vol. 77, p. 318-320.

[28] Launder, B.E., Spalding, D.B. (1972). *Lectures in Mathematical Models of Turbulence*, Academic Press, London.

[29] Hussein, A.M., Sharma, K.V., Bakar, R.A., Kadirgama, K. (2013). The effect of nanofluid volume concentration on heat transfer and friction factor inside a horizontal tube. *Journal of Nanomaterials*, vol. 2013, **DOI:10.1155/2013/859563**.

[30] Pak, B.C., Cho, Y.I., (1998). hydrodynamic and heat transfer study of dispersed fluids with submicron metallic oxide particles. *Experimental Heat Transfer: A Journal of Thermal Energy Generation, Transport, Storage, and Conversion*, vol. 11, no. 2, p. 151-170, **DOI:10.1080/08916159808946559**.

[31] Chon, C.H., Kihm, K.D., Lee, S.P., Choi, S.U.S. (2005). Empirical correlation finding the role of temperature and particle size for nanofluid (Al2O3) thermal conductivity enhancement. *Applied Physics Letters*, vol. 87, **DOI:10.1063/1.2093936**.

[32] Masoumi, N., Sohrabi, N., Behzadmehr, A. (2009). A new model for calculating the effective viscosity of nanofluids. *Journal of Physics D: Applied Physics*, vol. 42, **DOI:10.1088/0022-3727/42/5/055501**.

[33] Khanafer, Kh., Vafai, K., Lightstone, M., (2003). Buoyancy-driven heat transfer enhancement in a two-dimensional enclosure utilizing nanofluids. *International Journal of Heat and Mass Transfer*, vol. 46, no. 19, p. 3639-3653, **DOI:10.1016/S0017-9310(03)00156-X**.

[34] Gnielinski, V., Sruher, K. (1975). *Neue Gleichungen für den Wärme- und Stoffübergang in turbulent durchströmten Rohren und Kanälen, Forschung Ingenieurwesen*, vol. 41, p. 8-16, **DOI:10.1007/BF02559682**.

[35] Wusiman, K.E.B.J., Chung, H.S., Md, J.N., Handry, A., Eon., Y.S., Kim, J,H., Jeong, H.M. (2013). Heat transfer characteristics of nanofluid through circular tube. *Journal of Central South University*, vol. 20, no. 1, p. 142-148, **DOI:10.1007/s11771-013-1469-z**.

[36] Torii, S. (2010). Turbulent heat transfer behavior of nanofluid in a circular tube heated under constant heat flux. *Advances in Mechanical Engineering*, **DOI:10.1155/2010/917612**.

[37] Bergman, Th.L., Lavine, A.S., Incropera, F.P., DeWitt, D.P. (2011). *Fundamentals of Heat and Mass Transfer, 7th edition*, Wiley & Sons, Hoboken

[38] Allahyari, Sh., Behzadmehr, A., Hosseini Sarvari, S.M. (2011). Conjugate heat transfer of laminar mixed convection of a nanofluid through a horizontal tube with circumferentially non-uniform heating. *International Journal of Thermal Sciences*, vol. 50, no. 10, p. 1963-1972, **DOI:10.1016/j.ijthermalsci.2011.03.025**.

Strojniški vestnik - Journal of Mechanical Engineering 61(2015)11, 680-686
DOI:10.5545/sv-jme.2015.2698
Original Scientific Paper
Received for review: 2015-05-22
Received revised form: 2015-09-09
Accepted for publication: 2015-09-17

Experimental Study and Analysis of the Dynamic Mechanical Properties of Aluminium Bronze

Jinquan Li* – Hailin Guo – Peipei Zhou
Shenyangligong University, School of Mechanical Engineering, China

Accurate stress-strain curves of aluminium bronze (QAL9-4) under different temperatures and different strain rates were obtained using a dynamic compression test using a split Hopkinson pressure bar (SHPB). The dynamic mechanical properties of QAL9-4 were analysed. The Johnson-Cook (J-C) constitutive equation was obtained with experimental data fitting and the dynamic damage characteristics of QAL9-4 were studied using the mechanical response and microstructure analysis. The results show that QAL9-4 has an obvious strain-hardening effect and thermal softening effect, that the flow stress is not sensitive to the strain rate, and that the strain rate has almost no influence on the flow stress at room temperature and has a small effect at temperatures ranging from 300 °C to 700 °C. The fitting curves of the J-C constitutive model coincide well with the true stress-strain curves from the test.

Key words: dynamic mechanical property, aluminium bronze, constitutive relation

Highlights

- *Established the J-C constitutive model of QAL9-4.*
- *Obtained the true stress-strain curves describing the dynamic mechanical properties of QAL9-4.*
- *Analysed the dynamic damage characteristics of QAL9-4.*
- *Analysed the influence of J-C constitutive parameters on the mechanical properties of QAL9-4.*

0 INTRODUCTION

Aluminium bronze (QAL9-4) is widely used in many fields because it possesses high strength, hardness, wear resistance, good thermal conductivity, and because it can replace stainless steel and Ni-based alloys, among other factors. Therefore, there is a higher requirement for its dynamic mechanical properties. At present, extensive studies on aluminum bronze have primarily focused on alloy smelting, performance testing [1] and [2] and the influence of alloying treatment [3] and [4], or heat treatment [5] and [6] on microstructure [7] and properties [8]. However, less research has been done on the constitutive relation for QAL9-4.

The constitutive relation can reflect the inherent attribute of materials, which is the foundation for studying their dynamic properties. The constitutive relationship describing the dynamic mechanical behaviour of materials mainly includes the J-C model [9], the Zerrilli-Amstrong model [10], the Follanshbee-Kocks model [11], and so on. Of the above models, the J-C model not only can reflect the influences of strain, strain rate and temperature on the flow stress but also has a simple mathematical expression structure. Therefore, it has been the most widely used.

In this paper, the dynamic mechanical properties of QAL9-4 were investigated using the SHPB test at a high strain rate and high temperature, and then the true strain-stress curves were obtained. The J-C constitutive model parameters were calculated using the mathematical fitting method; moreover, the dynamic mechanical properties and failure characteristics of QAL9-4 were researched, combining the mechanical response and microstructural analysis to provide the design basis for the application of QAL9-4.

1 EXPERIMENTAL

In this paper, the SHPB tests were performed. The experimental material was QAL9-4, its chemical composition that was measured by the experiments is shown in Table 1. The shape of the sample was cylindrical with dimension ø 5 mm and ø 2 mm. When the strain rate was more than 5500 s^{-1}, the small-sized samples were used, and the specifications of the incident bar and transmission bar is 5 mm; when the strain rate was less than 5500 s^{-1}, the large-sized samples were used, and the specifications of the incident bar and transmission bar is 12.7 mm in both cases. The bullet length used in the test is 140 mm, the effective pressure was 0 MPa to 0.6 MPa, samples were heated with an electric heating furnace in the temperature range of 0 ºC to 700 ºC. The temperature was measured using quick response thermocouples and controlled with a feedback system. The experiments were conducted in the strain rate region of 2.5×10^3 s^{-1} to 1.0×10^4 s^{-1} and a temperature range of 20 ºC to 700 ºC, and the relevant data were

*Corr. Author's Address: Corr.Author's Address: No.6 Nanping Centre Road, Hunnan New District, Shenyang 110159, China, li_jinquan@163.com

recorded. Tests were conducted several times for each experimental condition to obtain three groups of similar data and to ensure the validity and reliability of the experimental results. The metallographic samples were made with workpiece material to observe their microstructures.

2 RESULTS AND DISCUSSION

2.1 Dynamic Mechanical Analysis of QAL9-4

The true stress-strain curves of QAL9-4 at various temperatures and different strain rates are shown in Fig. 1. As can be seen from Fig. 1a, when the strain rate is 2500 s^{-1}, 5500 s^{-1} and 10000 s^{-1}, the failure strain of the material is about 0.28, 0.35 and 0.5, respectively, at normal temperatures. This demonstrates that QAL9-4 has an obvious plasticity-increasing effect. The results are similar within the temperature range of 300 ºC to 700 ºC, and the flow stress increases with an increase in strain under the three different strain rates; there is a stronger strain-hardening effect. However, at a normal temperature, the increasing range of the flow stress is larger with the increase of strain, which shows that the strain-hardening effect is strongest. Conversely, the increasing range decreases gradually with the increase of strain as the temperature rises. When the temperature reaches 700 ºC, there is almost no strain-hardening effect, which indicates that the strain-hardening effect decreases with the increase of temperature, as shown in Fig. 1.

As can also be seen from Fig. 1, the flow stress decreases to a certain extent with the increase of temperature under three different strain rates; in particular, when the temperature is 700 ºC, the drop of flow stress is largest, and the thermal softening

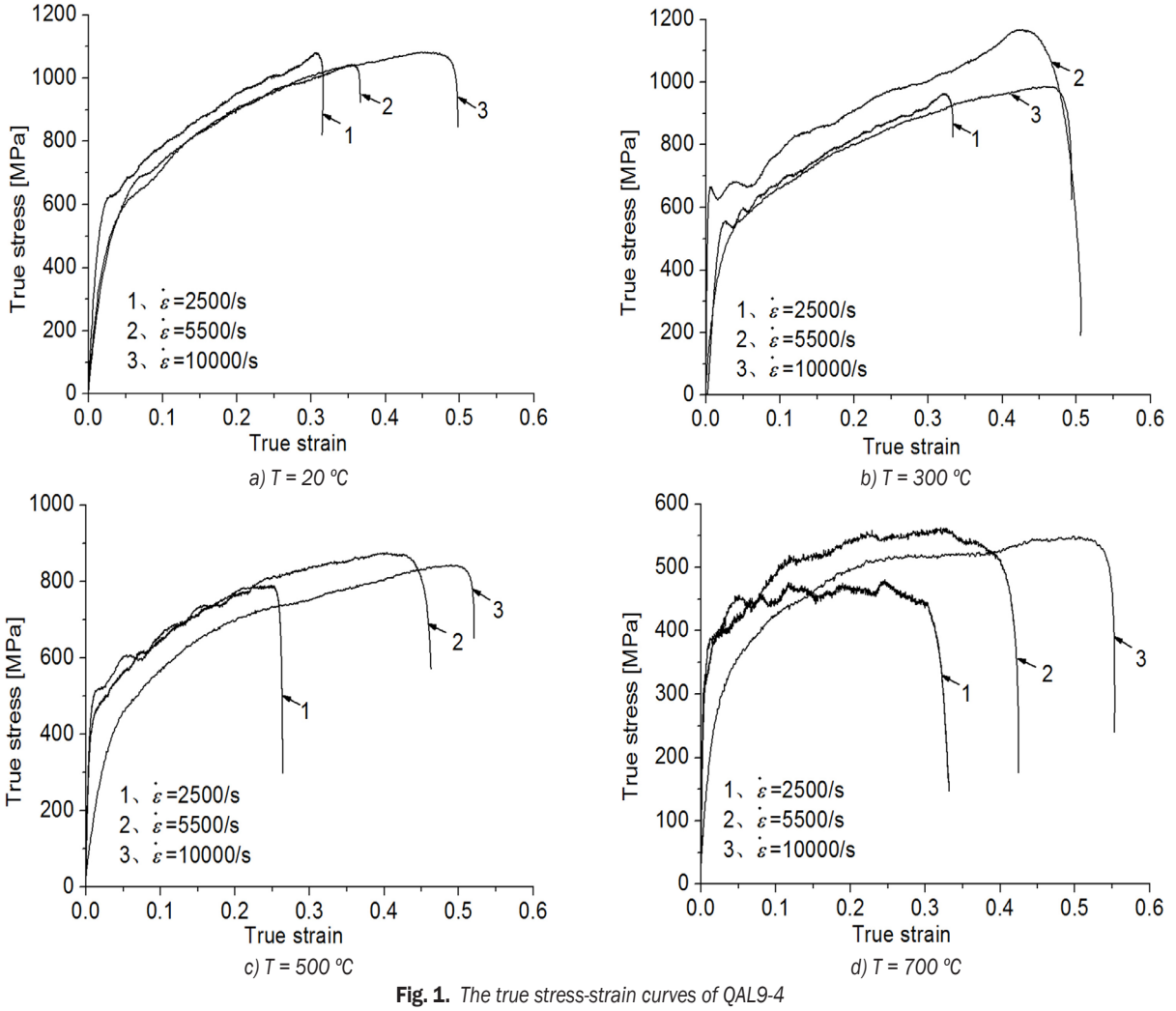

Fig. 1. *The true stress-strain curves of QAL9-4*

Table 1. *The chemical composition of QAL9-4 (wt %)*

Cu	Al	Fe	Pb	Mn	Zn	Sn	P	Si	impurity
allowance	9.28	3.04	≤0.01	≤0.5	≤1.0	≤0.1	≤0.01	≤0.1	≤1.7

effect is strongest, which indicates that the flow stress of QAL9-4 is sensitive to temperature. However, the change range of the flow stress is very small with an increase in the strain rate; the flow stress is not sensitive to the strain rate, and the strain rate hardening effect is weak.

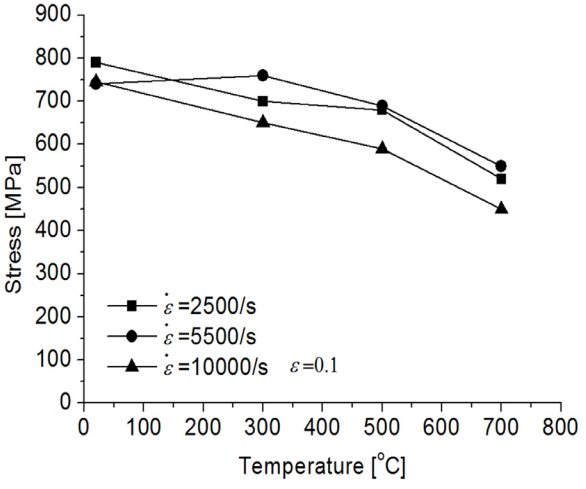

Fig. 2. *The influence of temperatures and strain rates on flow stress*

The influence of the strain rate on flow stress can almost be ignored at room temperature, and the influence is weak at 300 ºC to 700 ºC, which does not fully reflect the strain rate hardening effect. The flow stress even reduces with the increase in the strain rate. In other words, the strain rate strengthening effect and weakening effect appear alternately.

Take the strain $\varepsilon = 0.1$; stress-temperature curves are obtained at different strain rates using the data from Fig. 1, as shown in Fig. 2. As can be seen from Fig. 2, the flow stress decreases from 750 MPa to 800 MPa (at 20 ºC) to 450 MPa to 550 MPa (at 700 ºC) with the increase of temperature at three different strain rates. The change amplitude of the flow stress is biggest when the temperature is 300 ºC.

The above test results can be explained by the dislocation dynamics. The plastic deformation is dislocation motion in nature. According to the theory of dislocation dynamics, the dislocation movement in the crystal lattice will continuously encounter hindrance; this hindrance increases the difficulty of the dislocation motion, which makes the material possess a certain strength and hardness. When the dislocation moves from one equilibrium position of an atom to the next, it must overcome an energy barrier, that is to say, the dislocation is subject to the force. However, the heat energy makes the amplitude of the atomic vibration increase, which helps the dislocation to overcome the energy barrier.

The heat energy expression is **[12]**:

$$\Delta G = kT \ln \frac{\dot{\varepsilon}_0}{\dot{\varepsilon}}, \tag{1}$$

where ΔG is heat energy, k is correlation coefficient, T is temperature, $\dot{\varepsilon}_0$ is the reference strain rate, $\dot{\varepsilon}$ strain rate.

Eq. (1) shows that the heat energy increases with the increase in temperature and decreases with the increase of strain rate. The heat energy increases with the increase of temperature, which is conducive to overcoming energy barrier and causing the thermal softening phenomenon. Therefore, the heat energy is smaller at room temperature, the extent of thermal softening is lower, and the strain-hardening effect is strongest (Fig. 1a). The heat energy and thermal softening effect increases gradually with the increase of temperature, which results in the gradual decrease of the strain-hardening effect (Fig. 1b and c). When the temperature is 700 ºC, the heat energy is the greatest, and the thermal softening effect is the strongest, the strain-hardening effect is the weakest. The deformation of the workpiece is the largest (Fig. 1d).

In theory, the strain expression is **[12]**:

$$\varepsilon = \frac{bl\rho}{M}, \tag{2}$$

where ε is the strain, b is the dislocation Burgers vector, l is the movement distance of dislocation, M is the direction factor, and ρ is the dislocation density.

As can be seen from Eq. (2), the dislocation density increases with the increase of the strain, which makes the interaction among dislocations increase and produces a strain-hardening effect. Eq. (2) divided by time is the equation of the strain rate. It can be seen that the dislocation density also increases with the increase of the strain rate, which shows the strain rate hardening effect. However, that effect is not obvious under this experimental

condition; a strain rate weakening effect even occurs. The strain rate has almost no influence on flow stress at room temperature (Fig. 1a) and has a small effect at the temperature ranging from 300 ºC to 700 ºC, as shown in Figs. 1b, c and d. The values of stress under the strain rate of 10000 s^{-1} are always lower than those under the strain rates of 2500 s^{-1} and 5500 s^{-1} at the four different temperatures. This is because the flow stress is affected by the coupling of strain, strain rate, and temperature. Strain rate is not the only parameter determining the stress in the given strain and temperature. The dislocation density increases with the increase of the strain rate. At the same time, the dislocation movement speed also increases, which makes the temperature rise and results in producing a thermal softening effect to a certain degree, and that microscopic damage, such as adiabatic shear band (ASB), micro-void and micro-crack, and so on, will occur inside material under a high strain rate (see section 2.4), which makes the properties deteriorate and strength drop. All of these factors offset some or all of the strain rate hardening effect, which shows the decrease of stress values under the effect of a high strain rate (10000 s^{-1}).

The above thermal softening effect and strain-hardening effect compete with each other during the process of high-speed deformation. It is assumed that the stress of the material is a function relation of strain, strain rate and temperature, i.e. $\sigma = f(\varepsilon, \dot{\varepsilon}, T)$, and the stress increment is given by:

$$d\sigma = \frac{\partial \sigma}{\partial \varepsilon} d\varepsilon + \frac{\partial \sigma}{\partial \dot{\varepsilon}} d\dot{\varepsilon} + \frac{\partial \sigma}{\partial T} dT. \quad (3)$$

In Eq. (3), $\partial\sigma/\partial\varepsilon > 0$ and $\partial\sigma/\partial\dot{\varepsilon} > 0$ express strain hardening and strain rate hardening, respectively, and $\partial\sigma/\partial T < 0$ expresses thermal softening.

In the early deformation, strain hardening is dominant, that is $d\sigma/d\varepsilon > 0$. The adiabatic temperature rises gradually as the plastic work is constantly converted into heat. Therefore, the thermal softening effect increases gradually. If the strain-hardening effect and thermal softening effect reach balance, then $d\sigma/d\varepsilon = 0$, which reaches the critical condition producing ASB, then the thermal softening effect increases continuously. When the thermal softening effect exceeds the strain-hardening effect, that is, $d\sigma/d\varepsilon < 0$, the material will generate local thermoplastic shear instability phenomenon that results in producing ASBs [13].

2.2 The Establishment of a QAL9-4 J-C Constitutive Model

At present, the J-C thermoplastic constitutive model is commonly used to describe dynamic mechanical behaviours. Based on the experimental phenomenon that materials exhibit the hardening effect with the increase of the strain and strain rate, and the softening effect with the increase of temperature, the flow stress of the material can be expressed as follows:

$$\sigma(\varepsilon, \dot{\varepsilon}, T) = f(\varepsilon) f(\dot{\varepsilon}) f(T), \quad (4)$$

where

$$f(\varepsilon) = A + B\varepsilon^n, \quad (5)$$

$$f(\dot{\varepsilon}) = 1 + C \ln\left(\frac{\dot{\varepsilon}}{\dot{\varepsilon}_0}\right), \quad (6)$$

$$f(T) = 1 - (T^*)^m. \quad (7)$$

Eqs. (5) to (7) are the strain-hardening function, the strain rate hardening function, and the thermal softening function, respectively. Therefore, the expression of the J-C constitutive model is given by:

$$\sigma(\varepsilon, \dot{\varepsilon}, T) = \left(A + B\varepsilon^n\right)\left[1 + C \ln\left(\frac{\dot{\varepsilon}}{\dot{\varepsilon}_0}\right)\right]\left[1 - (T^*)^m\right], \quad (8)$$

where σ is flow stress, ε is the plastic strain, $\dot{\varepsilon}$ is the plastic strain rate, $\dot{\varepsilon}_0$ is the reference strain rate.

$T^* = (T - T_0)/(T_m - T_0)$ where T_0 is the room temperature, T is the workpiece temperature, T_m is the melting temperature of the material, A is the initial yield stress [MPa], B is the hardening modulus, n is the work-hardening exponent, C is the coefficient depending on the strain rate, and m is the thermal softening coefficient. There are five parameters in this constitutive relation: A, B, C, n and m, respectively. At present, these parameters cannot be predicted and only are obtained via experiments.

Taking $\dot{\varepsilon} = \dot{\varepsilon}_0$, under the normal temperature condition ($T = T_0$), there is no strain rate hardening effect or thermal softening effect; Eq. (8) is simplified then as follows:

$$\sigma(\varepsilon) = A + B\varepsilon^n. \quad (9)$$

Therefore, according to the experimental data obtained under the normal temperature and quasi-static conditions, parameter A is the value of stress when ε is 0. Then, B and n can be obtained through data fitting using MATLAB software.

At room temperature ($T = T_0$), Eq. (8) is simplified, as follows:

$$\sigma = (A + B\varepsilon^n)[1 + C\ln(\frac{\dot{\varepsilon}}{\dot{\varepsilon}_0})], \quad (10)$$

namely,

$$\sigma = M + MC\ln(\frac{\dot{\varepsilon}}{\dot{\varepsilon}_0})]. \quad (11)$$

Taking $\dot{\varepsilon}_0 = 0.001\,\text{s}^{-1}$, $M = A + B\varepsilon^n$ is a constant for a given strain value. According to the $\sigma-\varepsilon$ experimental data at the normal temperature, the value of flow stress that corresponds to the given strain value can be calculated under different strain rates after obtaining the values of A, B and n. Therefore, the relation curve between σ and $\ln(\dot{\varepsilon}/\dot{\varepsilon}_0)$ is a linear relationship. The C value can then be obtained by calculating the slope MC.

After the above parameters are obtained, according to Eq. (8), there is:

$$1-\left(T^*\right)^m = \frac{\sigma}{\left(A+B\varepsilon^n\right)\left[1+C\ln\left(\frac{\dot{\varepsilon}}{\dot{\varepsilon}_0}\right)\right]}. \quad (12)$$

A series of stress values can be obtained by Eq. (12) for the given strain and strain rate values according to the $\sigma-\varepsilon$ experimental data under different temperature conditions, then Eq. (12) becomes a function of T^*, and then the value of m can be obtained by mathematic fitting.

Based on the J-C constitutive model and dynamic mechanical properties data of QAL9-4 obtained with SHPB tests, the parameters can be obtained by the above method and nonlinear regression analysis with MATLAB software, as follows:

A = 430 MPa, B = 904 MPa, C = 0.016, n = 0.66, m = 2.4. Hence, J-C constitutive model of QAL9-4 is given as:

$$\sigma = (430 + 904\varepsilon^{0.66})[1 + 0.016\ln(\frac{\dot{\varepsilon}}{\dot{\varepsilon}_0})]\left[1-(T^*)^{2.4}\right]. \quad (13)$$

A comparison between the J-C constitutive model curves fitting based on Eq. (13) and the true stress-strain curves obtained by the dynamic test data using SHPB test at the strain rate of 2500 s^{-1} and different temperatures is shown in Fig. 3. The fitting curves agree well with the test curves at 20 ºC, 300 ºC, and 500 ºC. However, there is a great error at 700 ºC. This is because the thermal softening effect of QAL9-4 is very strong at high temperatures. The decreasing range of the flow stress is large, and the stress almost does not increase with the increase of the strain, i.e. there is almost no strain-hardening effect at 700 ºC. Therefore, the fitting curves of the J-C constitutive model and the test curves have larger errors.

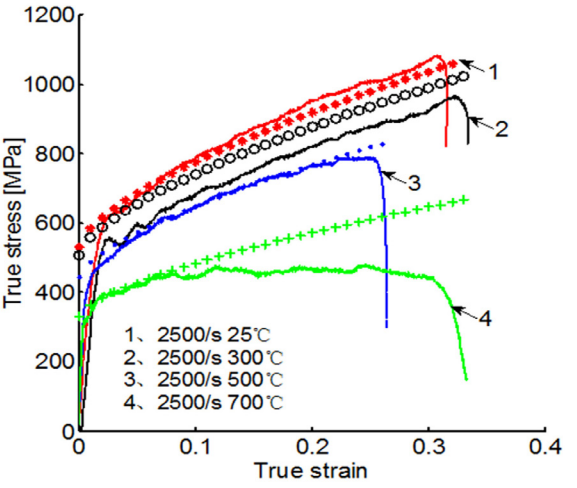

Fig. 3. *The comparison of J-C model fitting curves and test curves*

2.3 The Influence of J-C Constitutive Parameters on the Mechanical Properties

In the J-C constitutive model, A is the yield strength of the material. The larger the value of A, the stronger the bonds, the greater the hardness, and the more energy required in the high-velocity deformation of materials, the earlier the thermal softening phenomenon occurs. Therefore, the greater the strength, the likely it is that ASB will be generated [14].

B is the hardening modulus of the material. The flow stress and the energy during the process of material deformation increase with the increase of the B value. Therefore, the larger the B value, the more likely the thermal softening phenomenon is. n represents the strain-hardening effect. The larger the n value, the stronger the hardening effect, and the less prone to generating a thermal softening effect. m represents the thermal softening effect. The larger the m value, the more obvious the thermal softening phenomenon is and the more prone to producing ASB it is. C is the strain rate sensitivity coefficient. The larger the value of C, the more sensitive the flow stress-to-strain rate is.

2.4 The Microstructure Characteristics of QAL9-4

The QAL9-4 original microstructure with coarse equal axis grains and interphase is shown in Fig. 4a.

The black stripe where the white arrows are pointing in Fig. 4b is the deformed ASB formed by the effect of high-speed compression at 500 ºC and 10000 s^{-1}. Its shape is similar to that produced by

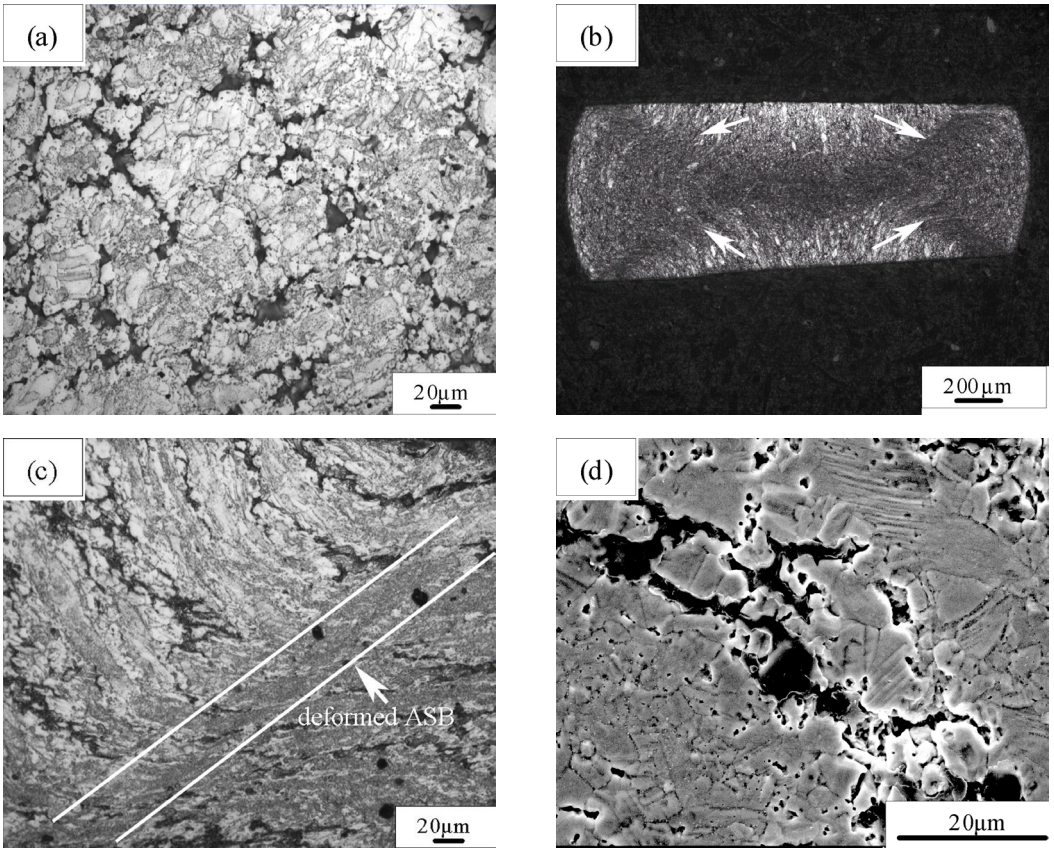

Fig. 4. *The original microstructure and internal damage of QAl9-4; a) original microstructure, b) deformed ASB, c) the partially enlarged drawing of deformed ASB, d) micro-cracks and micro-voids*

the effect of forging; its tread is along the direction of maximum shear stress, and its angle is about 45 degrees off the direction of principal stress **[15]**.

The area where the white arrow is pointing in Fig. 4c is the partially enlarged drawing of the ASB. As can be seen, the inhomogeneous plastic deformation was induced. The deformation on both sides of ASB is very serious. The grains were elongated because of the large deformation under impact loading and the elongated grains shattered gradually into tiny re-crystallization cores to finally form the dense and fine recrystallization grains inside the ASB.

The process of the high-speed deformation of the material is often accompanied by different internal micro-damage evolution that eventually leads to the failure of the material. Fig. 4d shows the micro-voids and micro-cracks in ASB, illustrating that the damage within the material is very serious, inevitably causing material deterioration and a reduction of dynamic mechanical properties. This is due to high speed, high strain rate, and large plastic deformation during the process of dynamic deformation.

3 CONCLUSIONS

- QAl9-4 exhibits a strain-hardening effect and thermal softening effect under a testing temperature range from 20 ºC to 700 ºC; the strain-hardening effect is more obvious at normal temperatures.
- The flow stress is not sensitive to the strain rate; the strain rate has almost no effect on the flow stress at room temperature, and has a small effect on the flow stress at the temperature range of 300 ºC to 700 ºC.
- The J-C constitutive model of QAl9-4 established by nonlinear regression analysis using MATLAB software is in good agreement with the true stress-strain curves.

4 ACKNOWLEDGEMENTS

This work is financially supported by the National Natural Science Foundation of China (Grant No. 51275317/E050901) and Open Fund of Key

Laboratory of Liaoning Province for Advanced Manufacturing Technology and Equipment, Shenyang Ligong University.

5 REFERENCES

[1] Chen, F., Li, H., Guo, J., Yang, Y. (2009). Predictive model of superplastic properties of aluminum bronze and of the superplastic extrusion test. *Materials Science and Engineering: A*, vol. 499, no. 1-2, p. 315-319, **DOI:10.1016/j.msea.2008.04.077**.

[2] Gao, L., Cheng, X. (2008). Microstructure and mechanical properties of Cu-10% Al-4% Fe alloy produced by equal channel angular extrusion. *Materials and Design*, vol. 29, no. 4, p. 904-908, **DOI:10.1016/j.matdes.2007.03.006**.

[3] Zhang, S., Yin, Y., Li, P. (2014). Effect of solution and aging and cryogenic treatment on microstructure and properties of QAl9-4 aluminum bronze. *Transactions of Materials and Heat Treatment*, vol. 35, no.10, p. 39-43, **DOI:10.13289/j.issn.1009-6264.2014.10.008**. (in Chinese)

[4] Lin, G., Wang, L., Xu, X., Zeng, J. (2013). Effect of solution and aging treatment on microstructure and properties of QAl9-4-3 aluminum bronze. *The Chinese Journal of Nonferrous Metals*, vol. 23, no. 3, p. 679-686. (in Chinese)

[5] Kudashov, D.V., Zauter, R. Müller, H.R. (2008). Spray-formed high-aluminum bronzes. *Materials Science and Engineering: A*, vol. 477, no. 1-2, p. 43-49, **DOI:10.1016/j.msea.2007.06.085**.

[6] Wu, L., Liu, L., Liu, J., Zhang, R. (2012). Effects of high pressure heat treatment on microstructure and micro-mechanical properties of Cu77.96 Al22.04 alloy. *Materials Transactions*, vol. 53, no. 3, p. 504-507, **DOI:10.2320/matertrans.M2011296**.

[7] Kaplan, M., Yildiz, A.K. (2003) . The effects of production methods on the microstructures and mechanical properties of an aluminum bronze. *Materials Letters*, vol. 57, no. 28, p. 4402-4411, **DOI:10.1016/S0167-577X(03)00332-X**.

[8] Adesola, A.O., Odeshi, A.G., Lanke, U.D. (2013). The effects of aging treatment and strain rates on damage evolution in AA6061 aluminum alloy in compression. *Materials & Design*, vol. 45, p. 212-221, **DOI:10.1016/j.matdes.2012.08.021**.

[9] Johnson, G.R, Cook, W.H. (1983). A constitutive model and data for metals subjected to large strains, high rates and high temperatures. *Proceedings of the 7th International Symposium on Ballistics*, p. 541-547, from: *http://www.lajss.org/HistoricalArticles/A%20constitutive%20model%20and%20data%20for%20metals.pdf*, accessed on 2015-05-22.

[10] Zerilli, F.J, Armstrong, R.W. (1990). Description of tantalum deformation behavior by dislocation mechanics based constitutive relations. *Journal of Applied Physics*, vol. 68, no. 4, p. 1580-1591, **DOI:10.1063/1.346636**.

[11] Follansbee, P.S, Huang, J.C, Gray, G.T. (1990). Low-temperature and high- strain-rate deformation of nickel and nickel-carbon alloys and analysis of the constitutive behavior according to an internal state variable model. *Acta Metallurgica et Materialia*, vol. 38, no. 7, p. 1241-1254, **DOI:10.1016/0956-7151(90)90195-M**.

[12] Meyers, M.A. (1994). *Dynamic Behavior of Materials*. John Wiley & Sons, New York, p. 344-369, **DOI:10.1002/9780470172278**.

[13] Li, J.Q, Huang, D., Duan, Z., Li, S. (2005). Analysis on adabiatic shear band characteristic and cause of formation in process of penetration in armor. *Acta Armamen Tarii*, vol. 26, no. 1, p. 60-63. **DOI:10.3321/j.issn:1000-1093.2005.01.013**. (in Chinese)

[14] Li, G., Wang, M., Duan, C. (2011). Experimental study of adiabatic shear critical conditions in orthogonal cutting of hardened 45 steel. *Journal of Dalian University of Technology*, vol. 51, no. 4, p. 518-524, DOI:10.7511/dllgxb201104009. (in Chinese)

[15] Li, J.Q., Huang, D., Duan, Z., Cong, M. (2003). Microstructure near the penetrated hole in an experimental penetration target and characteristics of the adiabatic shear band. *Journal of University of Science and Technology Beijing*, vol. 25, no. 6, p. 545-548, **DOI:10.3321/j.issn:1001-053X.2003.06.014**. (in Chinese)

Vsebina

Strojniški vestnik - Journal of Mechanical Engineering
letnik 61, (2015), številka 11
Ljubljana, november 2015
ISSN 0039-2480

Izhaja mesečno

Razširjeni povzetki

Strojniški vestnik - Journal of Mechanical Engineering 61(2015)11, SI 115

Prejeto v recenzijo: 2015-07-02
Prejeto popravljeno: 2015-10-07
Odobreno za objavo: 2015-10-08

Numerično modeliranje prašenja z industrijske deponije kompleksne geometrije

Lovrenc Novak[1] – Benjamin Bizjan[1,2,*] – Jure Pražnikar[3] – Boris Horvat[2,3] – Alen Orbanić[2,3] – Brane Širok[1]

[1] Univerza v Ljubljani, Fakulteta za strojništvo, Slovenija
[2] Abelium d.o.o., Slovenija
[3] Univerza na Primorskem, Inštitut Andrej Marušič, Slovenija

Glavna okoljska in varnostna problematika, ki se pojavi pri transportu in shranjevanju razsutega tovora, je povezana s pojavom prašenja. Pri shranjevanju tovora na velikih odprtih deponijah, kot jih običajno srečamo v tovornih pristaniščih, je prašenje še posebej problematično zaradi izpostavljenosti deponije vetru. Prihaja do vetrne erozije in odnašanja finih delcev, kar pomeni onesnaženje okolice ter resno tveganje za zdravje ljudi zaradi delcev v zraku.

V prispevku so obravnavane vetrovne razmere in pojav prašenja na Evropskem Energetskem Terminalu (EET) v Luki Koper, ki je namenjen shranjevanju in pretovoru premoga in železove rude. EET je tekom celega leta občasno izpostavljen močnim vetrovom severovzhodne in vzhodne smeri (burja) ter zahodne smeri (tramontana), ki zlahka povzročijo dviganje in odnašanje prašnih delcev z deponije. Namen študije je bil ugotoviti lokalne porazdelitve vetra nad deponijo ter emisije prahu za različne smeri in jakosti vetra ter različne ukrepe protivetrne zaščite. Izdelan je bil model deponije s tipično porazdelitvijo kupov materiala ter vključenimi okoliškimi stavbami, ograjami in žerjavi. Simulacije toka zraka so bile izvedene z uporabo sodobnih orodij za računalniško dinamiko tekočin (CFD). Dodatno so bile ocenjene tudi emisije prahu po metodi EPA (United States Environmental Protection Agency). Vstopni robni pogoji za veter so bili določeni s statistično analizo lokalno izmerjenih hitrosti vetra za obdobje enega leta.

Rezultati simulacij kažejo, da je smer vetra ključni dejavnik, ki vpliva na učinkovitost tako neprepustnih kot poroznih protivetrnih ovir. Razsežnost ter oblika deponije, ki je razpotegnjena skoraj v smeri glavnih vetrov, pomenita glavno omejitev za zagotavljanje učinkovite protivetrne zaščite z obstoječo ograjo višine 11 m. Tudi zamenjava obstoječe neprepustne ograje s porozno strukturo pokaže omejen protivetrni učinek take ograje in sicer iz istih razlogov, kot pri neprepustni ograji. Vendar pa porozna ograja omogoča boljšo zaščito najbolj izpostavljenih kupov, zato se skupna emisija prahu bistveno zmanjša. Učinkovit ukrep za zmanjšanje hitrosti vetra nad kupi je postavitev poroznih pregrad med kupi (prečno na smer glavnih vetrov), vendar bi take pregrade na dejanski deponiji lahko predstavljale veliko oviro za razkladalno-nakladalne procese. Preverjen je bil tudi vpliv prerazporeditve kupov, vendar je učinek majhen, tak ukrep pa je tudi zelo ne-praktičen za uporabo na tranzitni deponiji.

Učinkovita postavitev protivetrnih ograj ali pregrad je na velikih deponijah, ki so izpostavljene močnim vetrovom, izredno zahtevna. Večina raziskav na področju vetrne emisije prahu je izdelanih na primerih enega kupa ali več enakomerno razporejenih kupov, kar je težko primerljivo z dejanskimi deponijami. Rezultati študije kažejo, da prisotnost bližnjih ograj, zgradb, inženirskih objektov ter neurejena razporeditev kupov pomembno vplivajo na vetrovne razmere, zato je pri obravnavi razmer na realnih deponijah navedene dejavnike vedno potrebno upoštevati.

Polivanje kupov nasute snovi z vodo in s snovjo, ki na površini tvori skorjo, ostaja v predstavljenem primeru deponije nepogrešljiv ukrep za preprečevanje prašenja. Študija nakazuje možnosti za učinkovito postavitev poroznih pregrad in ograj, ki bi bistveno zmanjšale erozijski potencial, še posebej ob nadaljnji optimizaciji postavitve in lastnosti pregrad.

Eksperimentalna validacija numeričnih simulacij z meritvami v vetrovniku ali na terenu ni bila izvedena zaradi omejenega časa in sredstev, ki so bili na voljo. Za potrditev verodostojnosti simulacij bi bila izvedba eksperimentalne validacije v prihodnosti velikega pomena.

Ključne besede: računalniška dinamika tekočin, emisije prahu, prašenje, odprta deponija, emisijski faktor, hitrost vetra

*Naslov avtorja za dopisovanje: Univerza v Ljubljani, Fakulteta za strojništvo, Aškerčeva 6, 1000 Ljubljana, Slovenija, benjamin.bizjan@fs.uni-lj.si

Strojniški vestnik - Journal of Mechanical Engineering 61(2015)11, SI 116

Prejeto v recenzijo: 2015-06-18
Prejeto popravljeno: 2015-08-13
Odobreno za objavo: 2015-09-02

Vpliv pnevmatično upravljanega mehanizma za variabilno krmiljenje ventilov na zmogljivost Ottovega motorja

Fatih Uysal* – Selami Sagiroglu
Univerza Karabuk, Tehniška fakulteta, Turčija

V predstavljeni študiji je bil klasični odmikalni mehanizem enovaljnega štiritaktnega motorja z vžigalno svečko in 6 konjskimi močmi zamenjan z elektropnevmatičnim mehanizmom nihajnih vzvodov, ki je bil zasnovan in izdelan za odpiranje sesalnega ventila z majhnim (3,7 mm), srednjim (5,7 mm) in velikim (7,7 mm) dvigom v območju vrtilnih hitrosti motorja od 1600 vrt./min do 2200 vrt./min. Zračni kompresor zagotavlja tlak 6 bar za bate, ki upravljajo z odmikali. Funkcije krmiljenja batov za postopno moduliranje dviga ventilov je opravljal krmilnik; volumetrični izkoristek, navor, moč in specifična poraba goriva med delovanjem pa so bili merjeni pri polni obremenitvi in primerjani z ustreznimi vrednostmi pri klasičnem odmikalnem mehanizmu. Rezultati študije so pokazali izboljšanje zmogljivosti motorja ob zmanjšanju dviga ventilov pri manjših vrtilnih hitrostih in ob povečanju dviga ventilov pri večjih hitrostih. Ugotovljeno je bilo tudi, da je mogoče vrtljaje prostega teka zmanjšati z zmanjšanjem dviga ventilov pri nižjih vrtljajih motorja.

Cilj študije je preučitev zasnove, izdelave in vplivov pnevmatično upravljanega ventilskega mehanizma na zmogljivost motorja, ki naj bi bila podobna rešitvi VTEC, kjer sta na odmikalni gredi poleg klasičnega odmikala tudi nizko in visoko odmikalo z nespremenjenim profilom, ki se aktivirata pri majhnih oz. pri velikih vrtljajih.

Obstoječi sistem nihajnih vzvodov je bil opuščen, odmikali izpušnega in sesalnega ventila pa sta bili predelani v skladu z referenčnim motorjem. Na obeh straneh sesalnega nihajnega vzvoda sta bila dodana prosta nihajna vzvoda. Konstruirana in izdelana sta bila tudi dva pnevmatsko krmiljena bata, katerih naloga je sklenitev in razklenitev prostih nihajnih vzvodov z vzvodom sesalnega ventila.

Največja volumetrična učinkovitost 60,68 % je bila ugotovljena pri nizkem odmikalu pri 2000 vrt./min motorja, idealna vrednost λ je bila 0,995 pri klasičnem odmikalu pri 2800 vrt./min motorja, največje povečanje navora je znašalo 30,58 % pri visokem odmikalu pri 4000 vrt./min, največje zmanjšanje specifične porabe goriva pa je bilo 30,54 % pri 4000 vrt./min motorja. Rezultati navajajo k sklepu, da spremenljiv dvig ventilov pri različnih vrtilnih hitrostih pozitivno vpliva na zmogljivost motorja.

Pri preizkusih je bila merjena tudi hitrost prostega teka motorja. Pri motorju s klasično odmično gredjo je motor v prostem teku ugasnil pod 1200 vrt./min, medtem ko je testni motor deloval z nizkim odmikalom še pri 900 vrt./min prostega teka.

Izboljšanje zmogljivosti motorja z nizkim odmikalom prispeva k manjši porabi goriva, še posebej pri vozilih za urbani transport.

Zmanjšanje dviga ventila olajša zagon motorja ter poskrbi za manjšo rabo električne energije pri zagonu. Samodejni Start/stop modul v avtomobilih lahko zagotovi manjšo rabo električne energije pri zaustavitvi in ponovnem zagonu motorja v križiščih. Na ta način se izboljša poraba goriva na cestah z veliko semaforji, nastavljenimi na dolge čase.

V preizkusih so bili uporabljeni motorji z uplinjačem, kjer je količina goriva, ki se meša z zrakom, odvisna od zgradbe šobe uplinjača. Pri različnih hitrostih so bile zato ugotovljene različne vrednosti λ. Podobni preizkusi na motorjih z neposrednim vbrizgavanjem in na motorjih z vbrizgavanjem v sesalni kanal bi dali drugačne rezultate.

Ključne besede: variabilno krmiljenje ventilov (VVT), VTEC, Ottov motor, zmogljivost motorja, vžigalna svečka, elektropnevmatski mehanizem nihajnih vzvodov

*Naslov avtorja za dopisovanje: Univerza Karabuk, Tehniška fakulteta, Oddelek za strojništvo, Karabuk, Turčija, fatihuysal@karabuk.edu.tr

Strojniški vestnik - Journal of Mechanical Engineering 61(2015)11, SI 117

Prejeto v recenzijo: 2015-02-05
Prejeto popravljeno: 2015-06-08
Odobreno za objavo: 2015-09-17

Numerično modeliranje pogojev toplotnega ugodja v notranjem prostoru z viri sončnega obsevanja

Igor Bonefacic* – Igor Wolf – Bernard Frankovic
Univerza na Reki, Fakulteta za strojništvo, Hrvaška

Cilj te študije je določitev vpliva virov sončnega obsevanja na učinkovitost hlajenja stenske klima naprave in pogoje toplotnega ugodja v zaprtem prostoru poleti. Modelirana je prazna pisarna na Reki, Hrvaška, ki ima dvojno zasteklena okna in gleda proti jugu. Tridimenzionalni primer prenosa toplote in pretoka zraka je bil razrešen s programsko opremo za računalniško dinamiko fluidov FLUENT, in sicer v standardnih pogojih z neposrednim virom sončnega obsevanja in brez. Simulirani in raziskani so bili štirje različni koti pritoka zraka iz klima naprave ter sončnega obsevanja na zunanje površine in skozi okno. V numeričnem modelu je bilo prevzetih nekaj poenostavitev za zmanjšanje števila kontrolnih volumnov, ki so potrebni za diskretizacijo domene in pohitritev izračuna. Notranje ovire, kot sta pisarniška miza in omara, so bile zanemarjene. V sobi ni dodatnih virov toplote, kot so ljudje, računalniki, zasloni itd. Za napovedovanje vpliva sončnega obsevanja skozi okno je bil uporabljen algoritem za sledenje sončnim žarkom v paketu FLUENT. Algoritem je bil tudi eksperimentalno preverjen. Vpliv sevanja na parametre toplotnega ugodja v prostoru je bil analiziran s primerjavo izmerjene in izračunane temperature tal v območju, ki je izpostavljeno direktnemu sončnemu obsevanja. Meritve površinske temperature v območju tal so bile opravljene s termovizijsko kamero FLIR ThermaCAM S65. Za vse obravnavane primere so predstavljeni in primerjani rezultati za hitrost zraka v prostoru, porazdelitev temperature, srednjo sevalno temperaturo (MRT) in napovedano srednjo oceno ugodja (PMV).

Teoretična analiza je pokazala, da so povprečne vrednosti temperature zraka in hitrosti zračnega toka pri določenih robnih pogojih v sprejemljivem območju, čeprav lahko nastopajo lokalna odstopanja od standardnih vrednosti za optimalno ugodje. V obdobju hlajenja so bile opažene znatne razlike v pogojih toplotnega ugodja ob upoštevanju sončnega obsevanja skozi okno. V primerih, ko je bilo v simulacijah upoštevano sončno obsevanje, so bile povprečne temperature v prostoru za približno 4 °C višje kot v primerih brez vira sončnega obsevanja. Opažene so bile tudi določene razlike odvisno od kota pritoka zraka iz klima naprave, pri čemer je v spodnjih slojih zaradi vzgonskih učinkov prišlo do temperaturnega padca. V tem primeru se mora za izničenje vzgonskih učinkov povečati hitrost zračnega toka iz klima naprave, ki pa lahko spremeni lokalno porazdelitev zraka in skvari optimalne vrednosti ugodja.

Meritve in simulacije CFD so razkrile občutno povečanje temperature na delu tal, ki je direktno izpostavljen soncu. Čeprav je ta del razmeroma majhen, pa močno vpliva na ugodje, saj zvišuje povprečno temperaturo zraka in povzroča močne vzgonske pojave.

Kljub temu, da v simulacijah prostora niso bili upoštevani ljudje, pohištvo in dodatni viri toplote, je mogoče zaključiti, da je sončno obsevanje zelo pomemben dejavnik pri ocenjevanju toplotnega ugodja v prostoru. Za pravilno napoved toplotnega ravnovesja in pogojev ugodja v prostoru ga je zato treba vključiti v numerične simulacije. Predstavljeno numerično analizo je mogoče razmeroma preprosto prenesti tudi na podobne tehnične probleme na področju ogrevanja, prezračevanja in klimatizacije. Vanjo je mogoče vključiti tudi vlažnost zraka, notranje vire toplote kot so ljudje, računalniki, zasloni itd., kakor tudi časovno odvisne robne pogoje za simulacijo različnih izhodnih kotov zračnega toka, ki se nastavijo z vrtenjem izhodnih žaluzij klima naprave.

Ključne besede: numerično modeliranje, toplotno ugodje, hlajenje prostora, zračni tok, sončno obsevanje srednja sevalna temperatura

*Naslov avtorja za dopisovanje: Univerza na Reki, Fakulteta za strojništvo, Vukovarska 58, 51000 Reka, Hrvaška, igorb@riteh.hr

Strojniški vestnik - Journal of Mechanical Engineering 61(2015)11, SI 118

Prejeto v recenzijo: 2015-03-18
Prejeto popravljeno: 2015-07-31
Odobreno za objavo: 2015-10-01

Eksperimentalna raziskava vpliva več parametrov na preoblikovalnost pločevine DC01

Hakan Gürün* – İbrahim Karaağaç
Univerza Gazi, Tehniška fakulteta, Oddelek za proizvodno strojništvo, Turčija

Cilj te eksperimentalne študije je bil iskanje parametrov preoblikovanja, ki omogočajo doseganje največjega eksperimentalno določenega vlečnega razmerja. Podaja tudi primerjavo lastnosti preoblikovalnosti pločevine DC01 pri konvencionalnih in hidromehanskih postopkih globokega vleka z ozirom na silo pri vleku. Z identifikacijo idealnih parametrov preoblikovanja je mogoče odpraviti poskuse in napake ter priprave na proizvodnjo izdelka, kakor tudi zmanjšati stroške izdelka in orodja za podobne geometrije in parametre preoblikovanja.

Pločevina DC01 se uporablja pri globokem vleku mnogih izdelkov v različnih industrijah. Pločevina je bila izbrana za eksperiment zato, ker je v široki uporabi, s preizkusi pločevine pa je tudi mogoče identificirati idealne parametre preoblikovanja. Proizvodna industrija potrebuje nove tehnike, s katerimi bo mogoče odpraviti poskuse in napake ter priprave na proizvodnjo izdelka, kakor tudi zmanjšati stroške izdelka in orodja za podobne geometrije in parametre preoblikovanja.

Eksperimentalna študija je bila opravljena na eksperimentalnem sistemu, ki je bil zasnovan, zgrajen in umerjen. Eksperiment je bil zasnovan za izvajanje konvencionalnih in hidromehanskih procesov preoblikovanja ter za zajemanje procesnih podatkov v realnem času z elektromehanskim upravljanjem.

V eksperimentalni študiji so bili najprej identificirani parametri, ki opredeljujejo proces preoblikovanja in jih je treba preučiti. Opravljene so bile eksperimentalne študije s konvencionalnimi in hidromehanskimi procesi globokega vleka z identificiranimi eksperimentalnimi parametri. Vpliv in primerne vrednosti vsakega parametra so bili empirično identificirani in analizirani. Z identifikacijo eksperimentalnih parametrov so bile pridobljene tudi mehanske in kemijske lastnosti eksperimentalnega materiala.

V nadaljevanju so predstavljeni rezultati eksperimentalne študije.

- Tlak v komori matrice, polmer matrice in debelina pločevinastega materiala so parametri, ki so medsebojno povezani in jih ni mogoče obravnavati ločeno.
- Največje vlečno razmerje 2,33 pri hidromehanskem postopku globokega vleka pločevinastega materiala DC01 je bilo doseženo pri tlaku 0 MPa do 30 MPa.
- Največje vlečno razmerje pri konvencionalnem postopku globokega vleka je bilo 2,16.
- Pri hidromehanskem postopku globokega vleka se preoblikovalna sila povečuje s tlakom v komori.
- S povečevanjem polmera matrice se zmanjšuje preoblikovalna sila.
- Okolje, v katerem poteka preoblikovanje, je pri hidromehanskem postopku globokega vleka zelo učinkovito mazano. Pločevina se lahko zato vleče do konca brez gubanja.
- Tlak v komori in debelina pločevine sta tesno povezana parametra, tlak v komori med hidromehanskim globokim vlekom pa mora biti specificiran glede na debelino pločevine.
- Debelina se je v hidromehanskem procesu globokega vleka zmanjšala do 12 %. Ta vrednost je manjša od vrednosti zmanjšanja debeline pri konvencionalnem globokem vleku.

Študija prvič eksperimentalno preučuje vpliv tlaka v komori, polmera matrice in debeline pločevine na preoblikovalnost pločevinastega materiala DC01 pri hidromehanskem in konvencionalnem globokem vleku. Študija tudi pomaga pri določanju parametrov preoblikovanja tega materiala. Vlečno razmerje pri hidromehanskem globokem vleku se je zaradi povečanja tlaka v komori povečalo z 2,16 na 2,33. Rezultati eksperimenta so razkrili ustrezne parametre hidromehanskega in konvencionalnega preoblikovanja z globokim vlekom za vzorce materiala DC01 s cilindrično geometrijo.

Ključne besede: globoki vlek, hidromehanski globoki vlek, konvencionalni globoki vlek, DC01, preoblikovanje pločevine, hidroforming

*Naslov avtorja za dopisovanje: Univerza Gazi, Tehniška fakulteta, Oddelek za proizvodno strojništvo, Turčija, hgurun@gazi.edu.tr

Strojniški vestnik - Journal of Mechanical Engineering 61(2015)11, SI 119

Prejeto v recenzijo: 2015-06-17
Prejeto popravljeno: 2015-09-28
Odobreno za objavo: 2015-10-06

Študija vpliva neurejenih lupin na mehanske lastnosti nanožic iz SiC

Bin Zheng* – Huiling Du
Znanstveno-tehniška univerza Xi'an, Šola za materiale in inženiring, Xi'an 710054, Kitajska

Simulacije molekularne dinamike (MD) so bile uporabljene za izvedbo enoosne deformacije v simuliranih kvazistatičnih pogojih in ugotavljanje mehanskih lastnosti neurejenih nanožic SiC vrste jedro-lupina. Postavljen je bil model nanožic z jedrom premera 1 nm, 1,3 nm in 1,7 nm ter neurejeno lupino debeline 0,3 nm, 0,6 nm in 0,9 nm. Optimizacija atomskih položajev v začetnem modelu je bila opravljena po metodi minimizacije energije s pomočjo algoritma konjugiranega gradienta (CG). Notranje napetosti v začetni nanostrukturi so bile sproščene z relaksacijo pri konstantnem atmosferskem tlaku in temperaturi 300 K. Struktura je bila postopoma obremenjena v aksialni smeri s periodičnimi robnimi pogoji. Enoten odmik pri vsakem koraku je bil 0,1 nm, relaksacijski čas pri konstantni temperaturi pa je znašal 500 pikosekund. Tako je bila dosežena ekvivalentna hitrost deformiranja 0,2 m/s (0,002 % ps^{-1}).

Objavljene napetosti so bile izračunane kot vsota napetostnega tenzorja vseh atomov v smeri deformiranja, deljena s prostornino sistema. Pri stopnji deformacije od –3 % do 3 % so bile uporabljene linearna regresija in krivulje odvisnosti deformacije od napetosti za ocenjevanje modula elastičnosti (Y). Ugotovljeno je bilo, da je modul elastičnosti golih nanožic večji od modula pri žicah, prevlečenih z neurejenimi sloji. Porazdelitev atomskih napetosti v nanožicah je bila uporabljena za analizo trdnosti žic, prevlečenih z neurejeno lupino. Izkazalo se je, da je večina atomov v goli nanožici v stanju pod napetostjo, medtem ko pri nanožicah vrste jedro–lupina atomi neurejene lupine na vmesniku nasitijo proste vezi v površini jedra SiC in se napetost na vmesniku zaradi neujemanj rešetke skoraj povsem sprosti. Nanožice SiC vrste jedro–lupina slabo prevzemajo zunanje obremenitve, kar je tudi glavni razlog za majhno trdnost žic, prevlečenih z neurejeno lupino.

Zanimivo je tudi opažanje, da so nanožice SiC–*d*-C in SiC–*d*-Si bolj toge zaradi velikega kristalnega jedra pri fiksni debelini neurejene lupine. Modul elastičnosti jedra je za dva- do trikrat večji od modula elastičnosti lupine, kar kaže na pomembnejšo vlogo jedra pri trdnosti žic vrste jedro-lupina. To potrjuje tudi pojav nateznega napetostnega stanja v jedru ter ničelnih napetosti v jedru pod vplivom zunanje natezne sile.

S spremljanjem razvoja strukture pod obremenitvijo na atomski ravni so bile pridobljene informacije o plastičnih deformacijah nanožic SiC. V golih žicah SiC se niso pod kritično stopnjo deformacije (31 %) ob dodatni kompresiji pojavile nobene napake v strukturi. Ko je kritična stopnja deformacije presežena, nenadna prekinitev vezi Si–C zunaj območja vzvoja in nato čisti zlom nakazuje krhko vedenje. Pri nanožicah vrste jedro–lupina nasprotno med deformiranjem ni bil opažen čist zlom v izoliranem jedru in lupini, kot kažejo plastične deformacije nanožic SiC zaradi neurejene plasti. Primerjava konfiguracije gole žice in izoliranega jedra pokaže, da je struktura slednjega bolj neurejena. Avtorji verjamejo, da je amorfizacija jedra, ki jo povzroči neurejena lupina, glavni krivec za duktilne lastnosti nanožic vrste jedro–lupina.

Mehanske lastnosti nanožic vrste polprevodniško jedro–lupina so odvisne od vrste in debeline neurejene lupine, kar je treba upoštevati pri snovanju nanonaprav za določeni namen uporabe. Vmesnik jedro–lupina vpliva na trdnost s prerazdelitvijo atomskih napetosti v nanožicah. Rezultati raziskave osvetljujejo funkcijo tanke neurejene plasti v nanostrukturi, ki je sicer ni težko razkriti z eksperimentom, vendar je pogosto prezrta.

Ključne besede: nanožica vrste jedro–lupina, mehanske lastnosti, modul elastičnosti, vpliv velikosti, duktilnost, simulacija molekularne dinamike

*Naslov avtorja za dopisovanje: Znanstveno-tehniška univerza Xi'an, Šola za materiale in inženiring, Xi'an 710054, Kitajska, zhengbin@xust.edu.cn

Strojniški vestnik - Journal of Mechanical Engineering 61(2015)11, SI 120

Prejeto v recenzijo: 2015-06-30
Prejeto popravljeno: 2015-09-15
Odobreno za objavo: 2015-09-17

Numerična raziskava vpliva Reynoldsovega števila na toplotne in hidrodinamične parametre mešanega konvektivnega prenosa toplote s turbulentnim tokom v poševni cevi

Farhad Vahidinia* – Mohadeseh Miri
Univerza v Zabolu, Oddelek za strojništvo, Iran

Članek poroča o numerični raziskavi vpliva Reynoldsovega števila na toplotne in hidrodinamične parametre mešanega konvektivnega prenosa toplote pri turbulentnem toku nanofluida voda/Al_2O_3 v poševnem krožnem kanalu. Zgornja stena kanala je bila izpostavljena neenakomernemu toplotnemu toku, njegov spodnji del pa je bil izoliran. Za reševanje vodilnih enačb so bili uporabljeni model dvofazne zmesi, metoda končnih volumnov in shema gorvodnih razlik drugega reda.

Pri študiju mešanega konvektivnega prenosa toplote s turbulentnim tokom je pomembna preučitev sprememb Reynoldsovega števila in njihovega vpliva na toplotne in hidrodinamične parametre. Privzeto je bilo Reynoldsovo število od 4000 do 6000, 4-odstotni volumski delež nanodelcev in Grashofovo število $Gr = 1\times10^8$. Nagib cevi glede na vodoravnico je bil 45°. Za prikaz veljavnosti ter natančnosti modela in numeričnega postopka so bile opravljene primerjave z razpoložljivimi rezultati eksperimentov in numeričnih simulacij.

Rezultati so pokazali, da postane brezdimenzijska aksialna hitrost pri določenem Grashofovem številu in konstantnem volumskem deležu enakomernejša, ko se poveča Reynoldsovo število. S povečanjem Reynoldsovega števila se poveča aksialni moment in pojavi se turbulenca v smeri toka. Maksimalna brezdimenzijska aksialna hitrost in razvoj se zmanjšata s povečanjem Reynoldsovega števila, predvsem zato, ker postane profil hitrosti s povečanjem Reynoldsovega števila enakomernejši. S povečanjem Reynoldsovega števila se povečata hitrost in turbulence v fluidu, posledično pa tudi turbulentna kinetična energija. S povečanjem Reynoldsovega števila se povečata koeficient konvektivnega prenosa toplote in strižne napetosti, koeficient površinskega trenja pa se zmanjša.

Prenos toplote v nanofluidu je odvisen od različnih parametrov kot so toplotna prevodnost, koeficient konvektivnega prenosa toplote, viskoznost, specifična toplota, kot cevi glede na vodoravnico in volumski delež nanodelcev. V okviru preučevanja hidrodinamičnega in toplotnega vedenja nanofluidov v poševni cevi sta bili pridobljeni dve enačbi za izračun povprečnega Nusseltovega števila in koeficienta površinskega trenja na stenah.

Namen tega dela je preučitev prenosa toplote v poševnih ceveh z nanofluidi ter vpliva Reynoldsovega števila na toplotne in hidrodinamične lastnosti turbulentnega toka. Ta študija se lahko razširi z eksperimentom za sončne kolektorje v zgoraj omenjenih robnih pogojih za optimizacijo rabe energije. Raziskovalci lahko problem preučujejo tudi pri drugačnih robnih pogojih oz. pri drugačnem naklonu cevi glede na vodoravnico. Eksperimentalno in numerično je mogoče preučiti tudi vpliv drugih parametrov, kot so Grashofovo število, volumski delež ter premer nanodelcev. Uporabiti je mogoče tudi druge nanofluide in poiskati najboljše za prenos toplote v poševnih ceveh in sončnih kolektorjih.

Ključne besede: mešana konvekcija, poševni kanal, turbulentni tok, Reynoldsovo število, koeficient površinskega trenja, koeficient konvektivnega prenosa toplote

*Naslov avtorja za dopisovanje: Univerza v Zabolu, Oddelek za strojništvo, Zabol, Iran, f.vahidinia@gmail.com

Strojniški vestnik - Journal of Mechanical Engineering 61(2015)11, SI 121

Prejeto v recenzijo: 2015-05-22
Prejeto popravljeno: 2015-09-09
Odobreno za objavo: 2015-09-17

Eksperimentalna študija in analiza dinamičnih mehanskih lastnosti aluminijevega brona

Jinquan Li* – Hailin Guo – Peipei Zhou
Univerza Shenyang Ligong, Šola za strojništvo, Kitajska

Aluminijev bron (QAL9-4) se uporablja na številnih področjih zaradi svoje visoke trdnosti, trdote, protiobrabne obstojnosti in dobre toplotne prevodnosti. Material je tudi primerna zamenjava za nerjavno jeklo, nikljeve zlitine itd. Obširne raziskave aluminijevega brona so bile do sedaj osredotočene predvsem na pripravo zlitine, preizkušanje zmogljivosti ter na vplive legirnih dodatkov in toplotne obdelave na mikrostrukturo in lastnosti. Konstitutivne relacije brona QAL9-4 pa so manj raziskane. V članku so zato preučene dinamične mehanske lastnosti in določena je Johnson-Cookova (J-C) konstitutivna enačba za QAL9-4 kot osnova za praktično uporabo tega materiala.

Preučene so bile dinamične mehanske lastnosti in poškodbene lastnosti materiala QAL9-4. Prave krivulje odvisnosti deformacij od napetosti za aluminijev bron (QAL9-4) pri različnih temperaturah (v območju od 20 °C do 700 °C) in pri različnih hitrostih obremenjevanja (v območju od 2500 s^{-1} do 10000 s^{-1}) so bile pridobljene v dinamičnem kompresijskem preizkusu z deljenim Hopkinsonovim tlačnim drogom (SHPB). Rezultati kažejo jasen pojav deformacijskega utrjevanja in toplotnega mehčanja pri QAL9-4, napetost tečenja ni odvisna od hitrosti obremenjevanja, hitrost obremenjevanja praktično nima vpliva na napetost tečenja pri sobni temperaturi, v temperaturnem območju od 300 °C do 700 °C pa ima majhen vpliv.

Zaradi učinka visokohitrostne kompresije se pri 500 °C in 10000 s^{-1} oblikuje deformiran adiabatni strižni pas (ASB). Njegova oblika je podobna formacijam, ki nastanejo pri kovanju, usmerjen je v smeri maksimalne strižne napetosti in pod kotom približno 45° glede na smer glavne napetosti. Deformacije na obeh straneh ASB so resne. Zrna so se zaradi velikih deformacij pod udarno obremenitvijo podaljšala, podaljšana zrna so se postopoma razbila v drobna rekristalizacijska jedra, le-ta pa so končno oblikovala gosta in fina rekristalizirana zrna v ASB.

Proces visokohitrostnih deformacij QAL9-4 pogosto spremlja razvoj notranjih mikropoškodb, ki v končni fazi privedejo do odpovedi. Mikroluknje in mikrorazpoke v ASB kažejo, da so poškodbe QAL9-4 zelo resne ter neizogibno privedejo do pešanja materiala in zmanjšanja dinamičnih mehanskih lastnosti. To je posledica visokohitrostnih in velikih obremenitev ter velikih plastičnih dinamičnih deformacij.

Zapisana je konstitutivna enačba J-C. Termoplastični konstitutivni model J-C se danes pogosto uporablja za opis dinamičnega mehanskega vedenja (enačba (8)).

Na podlagi eksperimentalne ugotovitve, da pri materialu QAL9-4 s povečevanjem obremenitev in hitrosti obremenjevanja prihaja do učinka utrjevanja, s porastom temperature pa do pojava mehčanja, so bili izračunani parametri konstitutivnega modela J-C z matematičnim iskanjem prilega, konstitutivna enačba pa je bila določena s prilegom eksperimentalnih podatkov, pridobljenih z napravo SHPB (enačba (13)).

Krivulje prilega konstitutivnega modela J-C se dobro ujemajo s pravimi krivuljami odvisnosti deformacij od napetosti, ki so bile določene v preizkusih. Po konstitutivnem modelu J-C z večanjem meje plastičnosti materiala prihaja do zgodnejšega pojava toplotnega mehčanja. Večji kot je modul utrjevanja materiala, bolj je ta nagnjen k toplotnemu mehčanju; večji kot je vpliv deformacijskega utrjevanja, bolj intenzivno je utrjevanje; večji kot je vpliv toplotnega mehčanja, bolj očiten je pojav toplotnega mehčanja. C je količnik občutljivosti na hitrost obremenjevanja: večji kot je, bolj občutljiva je napetost tečenja na hitrost obremenjevanja.

Ključne besede: dinamične mehanske lastnosti, aluminijev bron, konstitutivna relacija, adiabatni strižni pas, deformacije, hitrost obremenjevanja

*Naslov avtorja za dopisovanje: Univerza Shenyang Ligong, Šola za strojništvo, No.6 Nanping Centre Road, Hunnan New District, Kitajska, li_jinquan@163.com

Doktorske disertacije

DOKTORSKE DISERTACIJE

Na Fakulteti za strojništvo Univerze v Ljubljani je obranil svojo doktorsko disertacijo:

● dne *16. oktobra 2015* **Damir HUSEJNAGIĆ** z naslovom: »Model okolja v proizvodnji po naročilu« (mentor: prof. dr. Alojzij Sluga);

Proizvodna podjetja, v katerih se izvaja posamična proizvodnja zahtevnih izdelkov po naročilu, so pod hudim pritiskom globalne konkurence in razgibanih tržnih razmer, kar se odraža z razraščajočo paleto izdelkov, individualizacijo izdelkov in skrajševanjem časovnih okvirjev. Pri tem se soočamo s problemi naraščajoče kompleksnosti na vseh nivojih, od izdelkov in storitev do procesov. Očitno je, da v proizvodnih podjetjih s strukturno togostjo, deterministčnim pristopom k odločanju v stohastičnem okolju, hierarhično delitvijo pristojnosti in pomanjkljivo komunikacijo ter nezadostno izkoriščenostjo strokovnega znanja ni mogoče doseči teh porajajočih zahtev na ustrezni ravni.

Disertacija gradi na hipotezi, da je boljše obvladovanje kompleksnosti v proizvodnji izdelkov po naročilu mogoče doseči z uvedbo upravljanja v realnem času in z orodji, kot so ubikvitarna tehnologija in senzorska omrežja, pa tudi s preglednostjo, sledljivostjo in s sistemi za podporo odločanju v realnem času.

Za reševanje teh izzivov je razvit nov koncept ubikvitarnega avtonomnega delovnega sistema, ki predstavlja napredno strukturo za nadaljnji razvoj proizvodnih sistemov in okolij, v katerih se izvaja posamična proizvodnja zahtevnih izdelkov po naročilu, upoštevajoč sodobne informacijske tehnologije in tehnologije vgradnih sistemov za gradnjo takšnih struktur;

*

Na Fakulteti za strojništvo Univerze v Mariboru sta obranila svojo doktorsko disertacijo:

● dne *20. oktobra 2015* **Matej PAULIČ** z naslovom: »Model inteligentnega sistema za prilagajanje postavitve obdelovanca v delovni prostor obdelovalnega stroja« (mentor: prof. dr. Jože Balič);

Moderni obdelovalni sistemi zahtevajo nenehno posodabljanje in vključevanje najnovejših tehnologij v tehnološke postopke. Raziskave in razvoj obdelovanih postopkov se v zadnjem obdobju nagiba k rešitvam, ki na eni strani povečujejo hitrosti, večajo fleksibilnost in točnost, na drugi strani pa skrajšujejo razvojni cikel izdelka.

Uvajanje računalniškega vida na obdelovalne stroje nam omogoča, da lahko brez večjih težav zaznamo postavitev (pozicijo) in orientacijo obdelovanca, ki ga bomo obdelovali.

V raziskavi predlagamo uporabo metod umetne inteligence za zasnovo naprednega sistema, ki bo sposoben samodejno prilagoditi postavitev obdelovanca v obdelovalni prostor stroja., ter prilagoditi CNC-program za novo pozicijo vpetega obdelovanca. Predlagana je uporaba algoritmov optimizacije z rojem delcev, kot tudi uporaba mehke logike.

V zaključku raziskave so podani rezultati, ki utemeljujejo in dokazujejo uporabnost sistema. Podani so tudi predlogi za nadaljnji razvoj in raziskave;

● dne *21. oktobra 2015* **Tomaž IRGOLIČ** z naslovom: »Optimiranje odrezavanja gradientnega materiala pri frezanju« (mentor: prof. dr. Franc Čuš);

Uvajanje tehnologije laserskega navarjanja kovinskih materialov s postopkom LENS v zadnjem času pridobiva na veljavi in uporabnosti za namene popravila strojnih delov in gravur preoblikovalnih orodij. Kljub zelo dobrim dosežkom navarjanja plasti kovinskih materialov, je še vedno potrebna naknadna obdelava navarov s postopki odrezavanja. Dosedanji način poobdelave navarjene površine je bil s postopkom brušenja.

Način brušenja navarjenih plasti je dal do sedaj ustrezne rezultate. Slabost brušenja v primerjavi s frezanjem pa je manjši odvzem materiala v enaki časovni enoti. Prav zaradi tega je raziskava v okviru doktorske naloge potekala v smeri nadomestitve procesa brušenja s procesom frezanja.

Cilj raziskave je bil ugotoviti vpliv parametrov stroja za lasersko navarjanje na dobljene hrapavosti in valovitosti navarjenih površin gradientnega materialov. Problem navarjenih materialov je površina, ki ne ustreza standardu hrapavosti N6, kar je bil naš zastavljen cilj. Zato je potrebno navarjene površine nadaljnjo obdelati, za kar smo si izbrali proces frezanja z oblikovnim krogelnim frezalom. Z raziskavami smo dokazali, da je možno nadomestiti proces brušenja s procesom frezanja.

Površina vseh izdelanih vzorcev je bila predhodno skenirana s tri-razsežnim optičnim skenerjem. S skeniranjem se je zagotovil oblak točk, na podlagi katerega sta se v nadaljevanju naloge izračunala srednji aritmetični odstopek navarjenaga profila Ra,

največja višina izbočin Rp in debelina navarjenih plasti.

Za ugotavljanje debeline navarjenih plasti se je izdelal uporabniški vmesnik za merjenje debeline in analizo navarjenih plasti. S pomočjo izračunov se je v nadaljevanju izračunala minimalna potrebna globina frezanja z oblikovnim krogelnim frezalom, ki je potrebna, da dobimo poobdelano površino navarjenih plasti. Vsi vzorci ki so bili obdelani s frezanjem so imeli končno kvaliteto površine stopnje N6 oziroma boljšo.

Seveda je izbira rezalnih parametrov za poobdelavo navarjenih plasti gradientnih materialov s procesom frezanja ključnega pomena. Zato je pomembno, da poznamo trdoto materiala, njegovo kemijsko sestavo in pripadajoče mehanske lastnosti. Le te so v veliki meri odvisne od predhodno izbranih parametrov stroja za navarjanje.

Tekom raziskave pridobljeni rezultati so bili shranjeni v namensko izdelano podatkovno bazo. Ta je uporabniku prijazna in mogoča hiter pregled osnovnih podatkov o materialu, pregled izmerjenih rezalnih sil pri izbranih rezalnih pogojih in grafično primerjavo izmerjenih rezalnih sil pri različnih rezalnih parametrih.

Celotna raziskava doktorske naloge zajema predstavitev problema, osnove delovanja stroja za lasersko navarjanje in seveda vrsto preizkusov, kjer se je skenirala površina navarjenih slojev, izračunala pripadajoča hrapavost in valovitost površine in seveda vršila nadaljnja obdela navarjenih plasti gradientnih materialov s procesom frezanja.

Information for Authors

All manuscripts must be in English. Pages should be numbered sequentially. The manuscript should be composed in accordance with the Article Template given above. The maximum length of contributions is 10 pages. Longer contributions will only be accepted if authors provide juastification in a cover letter. For full instructions see the Information for Authors section on the journal's website: http://en.sv-jme.eu .

SUBMISSION:

Submission to SV-JME is made with the implicit understanding that neither the manuscript nor the essence of its content has been published previously either in whole or in part and that it is not being considered for publication elsewhere. All the listed authors should have agreed on the content and the corresponding (submitting) author is responsible for having ensured that this agreement has been reached. The acceptance of an article is based entirely on its scientific merit, as judged by peer review. Scientific articles comprising simulations only will not be accepted for publication; simulations must be accompanied by experimental results carried out to confirm or deny the accuracy of the simulation. Every manuscript submitted to the SV-JME undergoes a peer-review process.

The authors are kindly invited to submit the paper through our web site: http://ojs.sv-jme.eu. The Author is able to track the submission through the editorial process - as well as participate in the copyediting and proofreading of submissions accepted for publication - by logging in, and using the username and password provided.

SUBMISSION CONTENT:

The typical submission material consists of:

- A **manuscript** (A PDF file, with title, all authors with affiliations, abstract, keywords, highlights, inserted figures and tables and references),
- Supplementary files:
  - a **manuscript** in a WORD file format
  - a **cover letter** (please see instructions for composing the cover letter)
  - a ZIP file containing **figures** in high resolution in one of the graphical formats (please see instructions for preparing the figure files)
  - possible **appendicies** (optional), cover materials, video materials, etc.

Incomplete or improperly prepared submissions will be rejected with explanatory comments provided. In this case we will kindly ask the authors to carefully read the Information for Authors and to resubmit their manuscripts taking into consideration our comments.

COVER LETTER INSTRUCTIONS:

Please add a **cover letter** stating the following information about the submitted paper:

1. Paper **title**, list of **authors** and their **affiliations**.
2. **Type of paper**: original scientific paper (1.01), review scientific paper (1.02) or short scientific paper (1.03).
3. A **declaration** that neither the manuscript nor the essence of its content has been published in whole or in part previously and that it is not being considered for publication elsewhere.
4. State the **value of the paper** or its practical, theoretical and scientific implications. What is new in the paper with respect to the state-of-the-art in the published papers? Do not repeat the content of your abstract for this purpose.
5. We kindly ask you to suggest at least two **reviewers** for your paper and give us their names, their full affiliation and contact information, and their scientific research interest. The suggested reviewers should have at least two relevant references (with an impact factor) to the scientific field concerned; they should not be from the same country as the authors and should have no close connection with the authors.

FORMAT OF THE MANUSCRIPT:

The manuscript should be composed in accordance with the Article Template. The manuscript should be written in the following format:

- A **Title** that adequately describes the content of the manuscript.
- A list of **Authors** and their **affiliations**.
- An **Abstract** that should not exceed 250 words. The Abstract should state the principal objectives and the scope of the investigation, as well as the methodology employed. It should summarize the results and state the principal conclusions.
- 4 to 6 significant **key words** should follow the abstract to aid indexing.
- 4 to 6 **highlights;** a short collection of bullet points that convey the core findings and provide readers with a quick textual overview of the article. These four to six bullet points should describe the essence of the research (e.g. results or conclusions) and highlight what is distinctive about it.
- An **Introduction** that should provide a review of recent literature and sufficient background information to allow the results of the article to be understood and evaluated.
- A **Methods** section detailing the theoretical or experimental methods used.
- An **Experimental section** that should provide details of the experimental set-up and the methods used to obtain the results.
- A **Results** section that should clearly and concisely present the data, using figures and tables where appropriate.
- A **Discussion** section that should describe the relationships and generalizations shown by the results and discuss the significance of the results, making comparisons with previously published work. (It may be appropriate to combine the Results and Discussion sections into a single section to improve clarity.)
- A **Conclusions** section that should present one or more conclusions drawn from the results and subsequent discussion and should not duplicate the Abstract.
- **Acknowledgement** (optional) of collaboration or preparation assistance may be included. Please note the source of funding for the research.
- **Nomenclature** (optional). Papers with many symbols should have a nomenclature that defines all symbols with units, inserted above the references. If one is used, it must contain all the symbols used in the manuscript and the definitions should not be repeated in the text. In all cases, identify the symbols used if they are not widely recognized in the profession. Define acronyms in the text, not in the nomenclature.
- **References** must be cited consecutively in the text using square brackets [1] and collected together in a reference list at the end of the manuscript.
- **Appendix(-icies)** if any.

SPECIAL NOTES

Units: The SI system of units for nomenclature, symbols and abbreviations should be followed closely. Symbols for physical quantities in the text should be written in italics (e.g. *v*, *T*, *n*, etc.). Symbols for units that consist of letters should be in plain text (e.g. ms^{-1}, K, min, mm, etc.). Please also see: http://physics.nist.gov/cuu/pdf/sp811.pdf .

Abbreviations should be spelt out in full on first appearance followed by the abbreviation in parentheses, e.g. variable time geometry (VTG). The meaning of symbols and units belonging to symbols should be explained in each case or cited in a **nomenclature** section at the end of the manuscript before the References.

Figures (figures, graphs, illustrations digital images, photographs) must be cited in consecutive numerical order in the text and referred to in both the text and the captions as Fig. 1, Fig. 2, etc. Figures should be prepared without borders and on white grounding and should be sent separately in their original formats. If a figure is composed of several parts, please mark each part with a), b), c), etc. and provide an explanation for each part in Figure caption. The caption should be self-explanatory. Letters and numbers should be readable (Arial or Times New Roman, min 6 pt with equal sizes and fonts in all figures). Graphics (submitted as supplementary files) may be exported in resolution good enough for printing (min. 300 dpi) in any common format, e.g. TIFF, BMP or JPG, PDF and should be named Fig1.jpg, Fig2.tif, etc. However, graphs and line drawings should be prepared as vector images, e.g. CDR, AI. Multi-curve graphs should have individual curves marked with a symbol or otherwise provide distinguishing differences using, for example, different thicknesses or dashing.

Tables should carry separate titles and must be numbered in consecutive numerical order in the text and referred to in both the text and the captions as Table 1, Table 2, etc. In addition to the physical quantities, such as *t* (in italics), the units [s] (normal text) should be added in square brackets. Tables should not duplicate data found elsewhere in the manuscript. Tables should be prepared using a table editor and not inserted as a graphic.

REFERENCES:

A reference list must be included using the following information as a guide. Only cited text references are to be included. Each reference is to be referred to in the text by a number enclosed in a square bracket (i.e. [3] or [2] to [4] for more references; do not combine more than 3 references, explain each). No reference to the author is necessary.

References must be numbered and ordered according to where they are first mentioned in the paper, not alphabetically. All references must be complete and accurate. Please add DOI code when available. Examples follow.

Journal Papers:

Surname 1, Initials, Surname 2, Initials (year). Title. Journal, volume, number, pages, DOI code.

[1] Hackenschmidt, R., Alber-Laukant, B., Rieg, F. (2010). Simulating nonlinear materials under centrifugal forces by using intelligent cross-linked simulations. *Strojniški vestnik - Journal of Mechanical Engineering,* vol. 57, no. 7-8, p. 531-538, DOI:10.5545/sv-jme.2011.013.

Journal titles should not be abbreviated. Note that journal title is set in italics.

Books:

Surname 1, Initials, Surname 2, Initials (year). Title. Publisher, place of publication.

[2] Groover, M.P. (2007). *Fundamentals of Modern Manufacturing*. John Wiley & Sons, Hoboken.

Note that the title of the book is italicized.

Chapters in Books:

Surname 1, Initials, Surname 2, Initials (year). Chapter title. Editor(s) of book, book title. Publisher, place of publication, pages.

[3] Carbone, G., Ceccarelli, M. (2005). Legged robotic systems. Kordić, V., Lazinica, A., Merdan, M. (Eds.), Cutting Edge Robotics. Pro literatur Verlag, Mammendorf, p. 553-576.

Proceedings Papers:

Surname 1, Initials, Surname 2, Initials (year). Paper title. Proceedings title, pages.

[4] Štefanić, N., Martinčević-Mikić, S., Tošanović, N. (2009). Applied lean system in process industry. *MOTSP Conference Proceedings*, p. 422-427.

Standards:

Standard-Code (year). Title. Organisation. Place.

[5] ISO/DIS 16000-6.2:2002. *Indoor Air – Part 6: Determination of Volatile Organic Compounds in Indoor and Chamber Air by Active Sampling on TENAX TA Sorbent, Thermal Desorption and Gas Chromatography using MSD/FID.* International Organization for Standardization. Geneva.

WWW pages:

Surname, Initials or Company name. Title, from http://address, date of access.

[6] Rockwell Automation. Arena, from *http://www.arenasimulation.com,* accessed on 2009-09-07.

EXTENDED ABSTRACT:

When the paper is accepted for publishing, the authors will be requested to send an **extended abstract** (approx. one A4 page or 3500 to 4000 characters). The instruction for composing the extended abstract are published on-line: http://www.sv-jme.eu/information-for-authors/ .

COPYRIGHT:

Authors submitting a manuscript do so on the understanding that the work has not been published before, is not being considered for publication elsewhere and has been read and approved by all authors. The submission of the manuscript by the authors means that the authors automatically agree to transfer copyright to SV-JME when the manuscript is accepted for publication. All accepted manuscripts must be accompanied by a Copyright Transfer Agreement, which should be sent to the editor. The work should be original work by the authors and not be published elsewhere in any language without the written consent of the publisher. The proof will be sent to the author showing the final layout of the article. Proof correction must be minimal and executed quickly. Thus it is essential that manuscripts are accurate when submitted. Authors can track the status of their accepted articles on http://en.sv-jme.eu/.

PUBLICATION FEE:

Authors will be asked to pay a publication fee for each article prior to the article appearing in the journal. However, this fee only needs to be paid after the article has been accepted for publishing. The fee is 240.00 EUR (for articles with maximum of 6 pages), 300.00 EUR (for articles with maximum of 10 pages), plus 30.00 EUR for each additional page. The additional cost for a color page is 90.00 EUR. These fees do not include tax.

Strojniški vestnik -Journal of Mechanical Engineering
Aškerčeva 6, 1000 Ljubljana, Slovenia,
e-mail: info@sv-jme.eu

9 770039 248001
ISSN 0039-2480

http://www.sv-jme.eu

Contents

Papers